University of Alberta

Rigid Body Modeling of the Feline Hindlimb

by

Ryan Wayne Stewart

A thesis submitted to the Faculty of Graduate Studies and Research in partial fulfillment of the requirements for the degree of **Master of Science**.

Department of Mechanical Engineering

Edmonton, Alberta
Spring 2006

Library and Archives Canada

Published Heritage Branch

395 Wellington Street
Ottawa ON K1A 0N4
Canada

Bibliothèque et Archives Canada

Direction du Patrimoine de l'édition

395, rue Wellington
Ottawa ON K1A 0N4
Canada

Your file Votre référence
ISBN: 0-494-13891-2
Our file Notre référence
ISBN: 0-494-13891-2

NOTICE:
The author has granted a non-exclusive license allowing Library and Archives Canada to reproduce, publish, archive, preserve, conserve, communicate to the public by telecommunication or on the Internet, loan, distribute and sell theses worldwide, for commercial or non-commercial purposes, in microform, paper, electronic and/or any other formats.

The author retains copyright ownership and moral rights in this thesis. Neither the thesis nor substantial extracts from it may be printed or otherwise reproduced without the author's permission.

AVIS:
L'auteur a accordé une licence non exclusive permettant à la Bibliothèque et Archives Canada de reproduire, publier, archiver, sauvegarder, conserver, transmettre au public par télécommunication ou par l'Internet, prêter, distribuer et vendre des thèses partout dans le monde, à des fins commerciales ou autres, sur support microforme, papier, électronique et/ou autres formats.

L'auteur conserve la propriété du droit d'auteur et des droits moraux qui protège cette thèse. Ni la thèse ni des extraits substantiels de celle-ci ne doivent être imprimés ou autrement reproduits sans son autorisation.

In compliance with the Canadian Privacy Act some supporting forms may have been removed from this thesis.

While these forms may be included in the document page count, their removal does not represent any loss of content from the thesis.

Conformément à la loi canadienne sur la protection de la vie privée, quelques formulaires secondaires ont été enlevés de cette thèse.

Bien que ces formulaires aient inclus dans la pagination, il n'y aura aucun contenu manquant.

Canada

To my family.

Abstract

Rigid body models of the feline hindlimb are often used to estimate the joint torques which occur within the limb, aiding investigations into the locomotor control systems of cats. This study investigates the factors which can affect the estimated joint torques. The effect of including or excluding a rigid paw is investigated. Additionally the sensitivity of the estimated joint torques to variations in the mass, center of mass location (CML), centroidal moment of inertia (CMI) of each hindlimb segment, and non-planar motion of the hindlimb is also investigated.

This study determined that the estimated joint torques were significantly affected by the rigid body paw and the variations in the CML's and masses of each limb segment ($> 48\%$, $> 9\%$, $> 7\%$, respectively in the observed peak knee torque during stance). The variations in the CMI's, and the non-planar movement that was investigated, had negligible effects on the estimated joint torques.

Acknowledgements

I would like to thank my supervisor, Dr. Don Raboud, for the guidance over the course of my degree. It has been quite a journey and I have learned a number of important lessons. One of the lessons that will always stay with me came in the form of a question (that I was asked numerous times!)

"*Can you prove that what you have done works?*"

I have also learned that if you hear the words, "*That should be easy.*" from your supervisor, it will probably be quite the opposite!

I would also like to thank all the great people I have had an opportunity to get to know during my time in the lab. They provided help, feedback, and some much needed distraction.

Ryan Swain, Kristin Miller, David Burton, Simon Jones, Quenton Kusiek

Table of Contents

1 Introduction and Literature Review **1**
- 1.1 Kinematics . . . 3
- 1.2 Electromyography . . . 3
- 1.3 Inverse Dynamics . . . 4
- 1.4 Forward Dynamics . . . 7
- 1.5 Thesis Outline . . . 7

2 Data Collection **9**
- 2.1 Data Collection Method . . . 9
  - 2.1.1 Limitations of the Motion Capture System . . . 12
- 2.2 Kinematic and Ground Reaction Force Data . . . 13
  - 2.2.1 Two-Dimensional Kinematic Data . . . 14
  - 2.2.2 Three-Dimensional Kinematic Data . . . 22
  - 2.2.3 Two-Dimensional Ground Reaction Forces . . . 30
  - 2.2.4 Three-Dimensional Ground Reaction Forces . . . 34
  - 2.2.5 Limitations of the Force Plate Measurements . . . 35

3 Two-Dimensional Inverse Dynamics Model **37**
- 3.1 Anatomical Modeling . . . 38
- 3.2 Hindlimb Model . . . 42
- 3.3 Kane's Equations . . . 48
- 3.4 Two-Dimensional Joint Torques . . . 49
  - 3.4.1 Static and Dynamic Contributions to the Estimated Joint Torques . . . 52
  - 3.4.2 Fixed Hip Assumption . . . 54
- 3.5 Joint Torque Sensitivity to Variations in Segment Parameters 56
  - 3.5.1 Effect of Centroidal Moment of Inertia Variations . . . 58
  - 3.5.2 Effect of Segmental Mass Variations . . . 59
  - 3.5.3 Effect of Variations in Center of Mass Locations . . . 63
  - 3.5.4 Sensitivity Summary . . . 67

3.6 Rigid Body Paw Model 70
3.6.1 Equations of Motion with Rigid Body Paw 74
3.6.2 Estimated Joint Torques 75
3.6.3 Rigid Body Paw Summary 78

4 Three-Dimensional Inverse Dynamics Model **80**
4.1 Three-Dimensional Hindlimb Model 81
4.2 Three-Dimensional Kane's Equations 82
4.3 Three-Dimensional Joint Torques 84
4.4 Two-Dimensional and Three-Dimensional Joint Torque Comparison 88

5 Two-Dimensional Forward Dynamics **91**
5.1 Two-Dimensional Forward Dynamics Model 91
5.2 Failure of the Forward Dynamics Simulations 93
5.2.1 Forward Dynamics Simulations for a Simple Pendulum 94
5.3 Torsional Springs and Dampers 98
5.3.1 Implementation of Torsional Springs and Dampers . . . 102
5.3.2 Joint Torques with Torsional Spring-Damper Pairs . . 105
5.4 Concluding Remarks 107

6 Conclusions and Future Work **108**
6.1 Conclusions 108
6.2 Future Work 109

References **111**

A Motion Capture System Calibration **115**

B Autolev Code **119**
B.1 Two-Dimensional Hindlimb Model Code 119
B.2 Three-Dimensional Hindlimb Model Code 122

List of Tables

3.1 Centroidal moments of inertia and center of mass locations. . . 47
3.2 Table of two-dimensional hindlimb model segment parameters. 47
3.3 Maximum deviations observed in the estimated joint torques during the swing phases due to ±50% variations of the hindlimb segmental parameters. 57
3.4 Maximum deviations observed in the estimated joint torques during the stance phase due to ±50% variations of the hindlimb segmental parameters. 57
3.5 Segment parameters for the rigid body paw. 71

4.1 Table of three-dimensional hindlimb model segmental variables. 81

List of Figures

1.1 Typical feline hindlimb skeletal anatomy. 6

2.1 Schematic of the motion capture system. 11
2.2 Gait cycles for a typical hindlimb. 14
2.3 Positional data for a cat hindlimb. (Data set 1) 15
2.4 Definition of the joint angles. 17
2.5 Estimated joint angles: Θ_1, Θ_2, Θ_3. (Data set 1) 18
2.6 Estimated angular velocities: $\dot{\Theta}_1$, $\dot{\Theta}_2$, $\dot{\Theta}_3$. (Data set 1) 19
2.7 Estimated angular accelerations: $\ddot{\Theta}_1$, $\ddot{\Theta}_2$, $\ddot{\Theta}_3$. (Data set 1) . . 20
2.8 Triangulated hip and knee joint angles. 21
2.9 Angular velocities calculated using the triangulated position of the knee marker. 21
2.10 Angular accelerations calculated using the triangulated position of the knee marker. 22
2.11 Positional data for a cat hindlimb. (Data set 2) 23
2.12 Estimated joint angles: Θ_1, Θ_2, Θ_3 (Data set 2) 24
2.13 Estimated angular velocities: $\dot{\Theta}_1$, $\dot{\Theta}_2$, $\dot{\Theta}_3$. (Data set 2) 24
2.14 Estimated angular accelerations: $\ddot{\Theta}_1$, $\ddot{\Theta}_2$, $\ddot{\Theta}_3$. (Data set 2) . . 25
2.15 Abduction and adduction of the hip joint during the swing and stance phases. 26
2.16 Sample hip adduction and abduction angle data. 27
2.17 Approximated hip adduction and abduction angle, Θ_a. 29
2.18 Approximated hip out-of-plane angular velocity, $\dot{\Theta}_a$. 29
2.19 Approximated hip out-of-plane angular acceleration, $\ddot{\Theta}_a$. . . . 30
2.20 Raw force plate signals. 31
2.21 Filtered and unfiltered force plate signals. 32
2.22 Two-dimensional hindlimb ground reaction forces. 33
2.23 Three-dimensional hindlimb ground reaction forces. 34

3.1 Typical feline hindlimb skeletal anatomy. 39

3.2 Depiction of the paw prior to contact with the ground, immediately after contact with the ground, and near the end of the stance phase. 40
3.3 Trajectory of the MTP joint during the stance phase (0.23 s to 0.92 s). 41
3.4 Two-Dimensional hindlimb model for a typical feline hindlimb. 43
3.5 Free body diagram for the two-dimensional model. 44
3.6 Definition of joint torques. 45
3.7 Joint torques estimated from the two-dimensional inverse dynamics hindlimb model. 50
3.8 Selected hindlimb positions corresponding to Figure 3.7. . . . 50
3.9 Static contributions to the estimated joint torques. (Data Set 1) 53
3.10 Dynamic contributions to the estimated joint torques. (Data Set 1) 53
3.11 Hip joint torques estimated with the hip fixed and with the hip free to follow the actual hip motion. 55
3.12 Knee joint torques estimated with the hip fixed and with the hip free to follow the actual hip motion. 55
3.13 Ankle joint torques estimated with the hip fixed and with the hip free to follow the actual hip motion. 56
3.14 Hip joint torques estimated with ±50% variations in I_b. 59
3.15 Hip joint torques estimated with ±50% variations in M_a. . . . 60
3.16 Hip joint torques estimated with ±50% variations in M_b. . . . 60
3.17 Hip joint torques estimated with ±50% variations in M_c. . . . 61
3.18 Knee joint torques estimated with ±50% variations in M_b. . . 61
3.19 Knee joint torques estimated with ±50% variations in M_c. . . 62
3.20 Ankle joint torques estimated with ±50% variations in M_c. . . 62
3.21 Hip joint torques estimated with ±50% variations in L_1. . . . 64
3.22 Hip joint torques estimated with ±50% variations in L_2. . . . 64
3.23 Hip joint torques estimated with ±50% variations in L_3. . . . 65
3.24 Knee joint torques estimated with ±50% variations in L_2. . . . 65
3.25 Knee joint torques estimated with ±50% variations in L_3. . . . 66
3.26 Ankle joint torques estimated with ±50% variations in L_3. . . 66
3.27 Hip joint torques estimated using the slender rod assumption and the values predicted by Hoy and Zernicke (1985). 68
3.28 Knee joint torques estimated using the slender rod assumption and the values predicted by Hoy and Zernicke (1985). 68
3.29 Ankle joint torques estimated using the slender rod assumption and the values predicted by Hoy and Zernicke (1985). 69

3.30 Differences between the joint torques estimated using the slender rod assumption and the values predicted by Hoy and Zernicke (1985). 70
3.31 Rigid body paw model. 71
3.32 Joint angles for the rigid body paw. 72
3.33 Angular velocities for the rigid body paw. 73
3.34 Angular velocities for the rigid body paw. 73
3.35 Estimated MTP joint torques calculated calculated for different locations of center of pressure application. 76
3.36 Estimated hip joint torques calculated for different locations of center of pressure application. 77
3.37 Estimated knee joint torques calculated for different locations of center of pressure application. 77
3.38 Estimated ankle joint torques calculated for different locations of center of pressure application. 78

4.1 The four joint torques for the three-dimensional model. 82
4.2 Joint torques estimated by the three-dimensional inverse dynamics hindlimb model. 85
4.3 Selected hindlimb positions corresponding to Figure 4.2. . . . 85
4.4 Joint torques estimated by the two-dimensional inverse dynamics hindlimb model. 86
4.5 Static contributions to the estimated joint torques. (Data Set 2) 87
4.6 Dynamic contributions to the estimated joint torques. (Data Set 2) 87
4.7 Hip joint torques estimated by both the two-dimensional and three-dimensional hindlimb models. 89
4.8 Knee joint torques estimated by both the two-dimensional and three-dimensional hindlimb models. 89
4.9 Ankle joint torques estimated by both the two-dimensional and three-dimensional hindlimb models. 90
4.10 Differences between the two-dimensional and three-dimensional hindlimb torques. 90

5.1 Original kinematic data vs. the predicted kinematic data from the forward dynamics simulation 94
5.2 Single link pendulum. 95
5.3 Original kinematic data and the kinematic data predicted by the forward dynamics simulation for the single link pendulum. 96

5.4 Forces applied to the free end of the pendulum for the static case investigation. 97
5.5 Torsional spring-damper pair representation. 98
5.6 Single link pendulum with the addition of the torsional spring-damper pair. 99
5.7 Anatomic and total joint torques for the pendulum model. . . 100
5.8 Passive torques supplied during the inverse dynamics and during the forward dynamics simulation. 101
5.9 Magnification of Figure 5.8 to highlight the corrective torque supplied by the spring-damper pair during the forward dynamics simulation. 101
5.10 Two-dimensional hindlimb model with the addition of the linear torsional spring-damper pairs, ... 102
5.11 Passive Joint Torques created by the spring-damper pairs. . . 105
5.12 Total Joint Torques ($K = 0.04 \frac{\text{Nm}}{\text{rad}}, C = 0.042 \frac{\text{Nm·s}}{\text{rad}}$). 106
5.13 Anatomic joint torques. 106

A.1 Calibration board used for the calibration of the motion capture system. 116
A.2 Plot of the calculated X-Coordinate position of the reflective marker at Point 1 from the motion capture system. 117
A.3 Error in the measurement of the limb caused by two-dimensional data collection. 118

Nomenclature

Θ_1	Hip joint angle
Θ_2	Knee joint angle
Θ_3	Ankle joint angle
Θ_4	MTP joint angle
Θ_a	Hip abduction / adduction angle
$\dot{\Theta}_1$	Hip angular velocity
$\dot{\Theta}_2$	Knee angular velocity
$\dot{\Theta}_3$	Ankle angular velocity
$\dot{\Theta}_4$	MTP angular velocity
$\dot{\Theta}_4$	Hip abduction / adduction angular velocity
$\ddot{\Theta}_1$	Hip angular acceleration
$\ddot{\Theta}_2$	Knee angular acceleration
$\ddot{\Theta}_3$	Ankle angular acceleration
$\ddot{\Theta}_4$	MTP angular acceleration
$\ddot{\Theta}_4$	Hip abduction / adduction angular acceleration
Φ_1	relative angle between the thigh and shank
Φ_2	relative angle between the shank and tarsals
$\dot{\Phi}_1$	relative angular velocity between the thigh and shank
$\dot{\Phi}_2$	relative angular velocity between the shank and tarsals
GRF_x	Ground reaction force acting on the hindlimb in the X-direction
GRF_y	Ground reaction force acting on the hindlimb in the Y-direction
GRF_z	Ground reaction force acting on the hindlimb in the Z-direction
I_a	Centroidal moment of inertia of the thigh
I_b	Centroidal moment of inertia of the shank
I_c	Centroidal moment of inertia of the tarsal
I_d	Centroidal moment of inertia of the paw

M_a	Mass of the thigh segment
M_b	Mass of the shank segment
M_c	Mass of the tarsal segment
M_d	Mass of the paw segment
L_a	Length of the thigh segment
L_b	Length of the shank segment
L_c	Length of the tarsal segment
L_d	Length of the paw segment
L_1	Center of mass location for the thigh segment
L_2	Center of mass location for the shank segment
L_3	Center of mass location for the tarsal segment
L_4	Center of mass location for the paw segment
L_5	Location to which the GRF's are applied to the paw
g	Gravitational acceleration
K	Stiffness coefficient for the torsional springs
C	Damping coefficient for the torsional dampers
T_{hip}	Joint torque at the hip for the two-dimensional hindlimb model
T_{knee}	Joint torque at the knee for the two-dimensional hindlimb model
T_{ankle}	Joint torque at the ankle for the two-dimensional hindlimb model
T_{hip_X}	Joint torque about at the hip about the X-axis of the global reference frame for the three-dimensional hindlimb model
T_{hip_Y}	Joint torque about at the hip about the Y-axis of the global reference frame for the three-dimensional hindlimb model
CMI	Centroidal Moment of Inertia
CML	Center of mass location

Chapter 1

Introduction and Literature Review

Locomotion can be defined as the act of moving from place to place and encompasses tasks such as crawling, jumping, swimming, running, and walking. All animals, including humans, use some form of locomotion on a regular basis. In nature, locomotion is vital to meet the basic needs of food collection or self preservation. There are two principal systems that are responsible for locomotion: the musculoskeletal system, and the central nervous system or CNS, both of which must work in unison to coordinate and perform each locomotor task.

The musculoskeletal system provides the frame (skeleton) and the actuators (muscles) with which to create the motion. The muscles are connected to the bones of the skeleton by tendons and produce motion by moving the skeleton about its joints. The forces required to move the skeleton are created by contraction of the muscles, thus the forces that are created in the muscle are always tensile. Since muscles can only provide a tensile force, to reverse the motion of a limb caused by the contraction of one muscle group, another group of muscles is required to exert an opposite pull. As an example, one can consider simple flexion and extension of the human arm about the elbow joint. Flexion of the arm is accomplished by the contraction of the bicep muscles. During flexion of the arm the tricep muscles located on the back of the arm stretch until they are needed to reverse the motion of the arm. The tricep muscles then contract while the bicep muscles relax, extending the arm. Rarely does an individual muscle act by itself to create motion, instead groups of muscles work together synergistically to create motion. A number of muscles may be activated throughout the entire limb for a certain motion; however,

the times at which the muscles are activated, and the levels of activation for each individual muscle vary.

The CNS acts as a control system for the musculoskeletal system during locomotion. For each different type of locomotion, sensory information such as speed, direction, limb location, weight distribution, and intramuscular forces must all be simultaneously processed, monitored, and adjusted. The sheer amount of information that is processed and modified in order to allow for the completion of the many different types of locomotion is a testament to the complexity of the locomotor control system. To date, the precise architecture of the locomotor control system is unknown for both animals and humans. Much of the current knowledge about the control of locomotion in humans is actually derived from experiments on quadrupeds, most notably the typical house cat. While some extrapolations are required, many basic similarities between the locomotor systems of cats and humans have been demonstrated [Duysens et al. (2002)]. Human and cat locomotion is hierarchically controlled at several levels of the central nervous system, namely the spinal cord, the brainstem, and the cerebral cortex, which can interact and influence one another [Duysens et al. (2002)]. Difficulty arises in isolating each individual level of locomotor control because of the interrelation between the different levels of control for locomotion.

There are a number of areas which would benefit from a thorough understanding of the locomotor control system, such as prosthetics, robotics, and various fields within medicine. Prosthetic devices could be improved with respect to their functionality. Understanding the types of afferent and efferent signals, to and from the nervous system respectively, required for a specific locomotor task would then allow prosthetic devices to be designed such that they could process and simulate the required signals for the control system. Recent research has focused on ways of making connections with afferent nerve axons which can then be used as natural transducers for touch, force, and position [Gasson et al. (2005)]. Combining knowledge of the locomotor control system and a means of communication between the CNS and prosthetic device would allow for far more advanced prosthetics. To date many walking robots are relatively slow moving and have been confined to statically stable locomotion [Schmiedeler and Waldron (1999)]. The development of walking robots that can move with the same agility and speed as an animal, throughout numerous environments, is highly sought after because they would not have the same restrictions on their mobility as a wheeled robot would have. The medical field would also stand to benefit since a thorough understanding of the loco-

motor control system may allow for new methods of treatment for diseases, such as cerebral palsy, which disrupts the body's ability to control movement and posture.

As mentioned earlier much of the current knowledge about the control of locomotion in humans is actually derived from experiments with cats. The cat is an ideal subject for investigation into locomotion control since there is a considerable amount of knowledge available about the associated biology [Ekeberg and Pearson (2005)]. Investigations into the control systems for locomotion are often performed by means of gait analysis, which is defined as being the quantitative description of all mechanical aspects of gait [Cappozzo (1984)]. Typically there are four types of gait analysis tools which are used: kinematic analyses, electromyography, inverse dynamics, and forward dynamics.

1.1 Kinematics

The term kinematics is used to describe the motion of bodies or objects with respect to their positions, velocities, and accelerations without regard for the forces which cause the motion. Currently, kinematic data for gait studies is most often collected through the use of video based systems where markers are placed on the bodies of interest. The desired locomotion is then recorded. The markers are then found in each image captured by the video camera and their locations calculated. Based on the locations of the markers the positions, velocities, and accelerations of the bodies of interest are calculated.

Kinematic analyses have been used to investigate a broad range of locomotion topics such as: the angular movements of the hindlimb segments and the resulting lengths of select hindlimb muscles for a range of locomotion speeds [Goslow et al. (1973)], the coordination of the motion of the hindlimbs and forelimbs [Miller et al. (1975)], the theory that end point control and trajectory planning may be applicable to limb movement in locomotion [Shen and Poppele (1995)], the motor patters and hindlimb motions for up-slope and level walking [Carlson-Kuhta et al. (1998)], and the motor patterns and hindlimb motions for forward and backward walking [Buford et al. (1990)].

1.2 Electromyography

The electromyogram (EMG) uses an electrode placed within a muscle to measure the electrical activity. Thus, EMG's represent the muscle activation sig-

nal. An elusive goal of most investigators utilizing EMG in their studies has been, and still is, to relate the magnitude of the EMG signal to the muscle tension. However controversy exists about the correlation of EMG with muscle tension under dynamic loading conditions [Sutherland (2001)]. EMG results are usually presented as either an absolute voltage or as a percentage of a normalized standard. A drawback associated with EMG's is due to the nature of skeletal muscle make up. A muscle consists of many individual bundles of muscle fibres where each individual fibre gives off an electrical signal. Due to the sheer number of muscle fibres, and interference from other muscles, EMG signals are noisy. See Buford and Smith (1990); Carlson-Kuhta et al. (1998); Perell et al. (1993); Miller et al. (1975) for examples of EMG signals collected from cats.

EMG's are used to identify the muscles that are being activated during motion. A kinematic analysis is often performed in conjunction with and EMG analysis. This way the activation of the muscles can be correlated to the position of the limb, providing additional insight into the analysis. EMG's are also used to quantify muscle activation levels, and to find the times at which the muscle is active [Buford and Smith (1990); Carlson-Kuhta et al. (1998); Perell et al. (1993)].

1.3 Inverse Dynamics

While kinematic and EMG analyses are both useful gait analysis tools, they do not provide any indication of the magnitude of the reactions which occur within the limbs of the animal during locomotion. Direct measurement of the forces that occur within the limbs is usually not performed due to the invasive nature of the measurement techniques. Instead inverse dynamics are applied. The internal forces and moments are estimated based upon the physical properties of the limb, the motion of the limb, and the external forces applied to the limb. The moments acting about each individual joint in the limb caused by muscle forces acting within the limb, and the external forces acting on the limb, are termed joint torques. The external forces acting on a limb when in contact with a surface are known as ground reaction forces, or GRF's.

Physical properties for the limbs of cats have been published by both Manter (1938) and Hoy and Zernicke (1985), however the physical properties presented by Manter (1938) were fairly limited in scope as they only represent a single cat. Hoy and Zernicke (1985) went much further by measuring the

segmental parameters of nine separate cats. Hoy and Zernicke (1985) then developed empirical equations with which the segmental masses and centroidal moments of inertia about the center of mass for each limb segment can be predicted based on the lengths of each segment and the total mass of the cat. The results presented by Hoy and Zernicke (1985) are for a two-dimensional case, where the motion of the limb is assumed to occur in the sagittal plane. While the empirical equations developed by Hoy and Zernicke (1985) are often used to allow the prediction of feline hindlimb dynamics [Fowler et al. (1993); Perell et al. (1993); Trank and Smith (1996); McFayden et al. (1999)], to the author's knowledge no study has investigated how sensitive the estimated joint torques are to variations in the segmental parameters of the limbs. The results of the sensitivity analysis may allow the accuracy of the estimated joint torques to be improved in future works by finding more accurate methods of measuring or obtaining the segmental parameters, if so required.

To aid in the discussion which follows the skeletal anatomy of a typical feline hindlimb is shown in Figure 1.1. The hindlimb contains the following joints: a hip joint, a knee joint, an ankle joint, a metatarsophalangeal (or MTP) joint, and the interphalangeal joints of the paw. Figure 1.1 highlights the aforementioned joints in their respective order, from top to bottom. Excluding the paw, the feline hindlimb consists of three main segments: the thigh segment between the hip and knee joints, the shank segment between the knee and ankle joints, and the tarsal segment between the ankle and MTP joints.

Inverse dynamics have been used in a number of studies of feline locomotion. The earliest study that could found, that the author is aware of, was Manter (1938). Manter (1938) created a planar, three-link, rigid body model of a hindlimb (thigh, shank, and tarsals) to provide an estimate of the joint torques acting within the limb during contact with the ground. Hoy and Zernicke (1985) studied hindlimb dynamics when the hindlimb was swinging freely without ground contact for three separate gaits: pace-like walk, trot-like walk, and gallop. Here a planar, two-segment, rigid body system was used to represent the shank, as well as the tarsals and paw as a single segment. Fowler et al. (1993) used inverse dynamics to examine the relationship between internal force production in selected skeletal muscles, measured with transducers placed upon selected tendons, and the estimated joint torques when the hindlimb was in contact with the ground. The planar inverse dynamics model used by Fowler et al. (1993) was a three-segment, rigid body system representing the shank, tarsals, and paw respectively. The hindlimb kinetics during both forward and backward walking were assessed by Perell

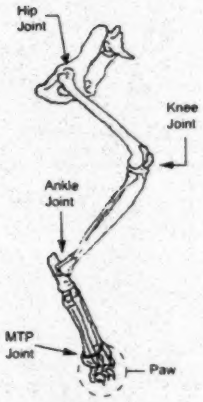

Figure 1.1: Typical feline hindlimb skeletal anatomy. The paw, which consists of the individual phalanges bones and the interphalangeal joints, is shown inside the broken circle.

et al. (1993). Here the planar, three-segment, rigid body model created by Hoy and Zernicke (1985) (thigh, shank, tarsals and paw) was used when the limb was not in contact with the ground. During contact with the ground a planar, four-segment, rigid body model (thigh, shank, tarsals, paw) was created based upon the three-segment model created by Fowler et al. (1993).

One dissimilarity between the inverse dynamics models used by Manter (1938), Fowler et al. (1993), and Perell et al. (1993) is in the way that the paw is modeled. It does not appear that Manter (1938) included the paw in his model since there is no kinematic data shown for the paw. Kinematic data was only shown for the thigh, shank, and tarsal segments. The lack of a paw in Manter's model poses a problem for the estimation of the joint torques in the hindlimb since the GRF's are distributed over the underside of the paw. The distribution of the GRF's can be represented by a single force in each coordinate direction, at a single location on the paw for each instant that the GRF's are measured. This point is known as the center of pressure. Over the duration of time that the paw is in contact with the ground, the center of pressure moves along the paw in the same direction as the locomotion [Fowler et al. (1993)]. Manter (1938) also inferred that the center of pressure does not remain at a fixed location, however the means with which to calculate the center of pressure were not available. Without the center of pressure Manter

(1938) estimated a location at which to apply the GRF's during the latter portion of the stance phase. Manter (1938) stated, 'An estimated position, inferred from the nature of the step, was used for the period toward the end of the step when the pressure under the foot shifts towards the region of the toes.' Manter (1938) reported that this correction had no significant impact on the observed final results. Fowler et al. (1993) and Perell et al. (1993) modeled the paw as a single rigid body during contact with the ground. Both Fowler et al. (1993) and Perell et al. (1993) measured the center of pressure which allows them to use their paw model.

In each of the inverse dynamics studies [Manter (1938); Hoy and Zernicke (1985); Fowler et al. (1993); Perell et al. (1993); Trank and Smith (1996)] an assumption was made that the joint torques which were investigated could be accurately estimated from a planar model, even though in reality the hindlimb is not restricted to planar motion.

1.4 Forward Dynamics

Forward dynamics uses known forces and moments, both external and internal, acting on a system of bodies to calculate the resulting motion of the system. Often a forward dynamics model is created to test a theory about the control of locomotion [Herr and McMahon (2000); Van Den Bogert et al. (1989)]. The movements predicted by the forward dynamics model can be compared to reality, enabling identification of incorrect models in many cases. Thus forward dynamic simulation models can lead to a better understanding of the functioning of the locomotor system and the factors that affect it's normal behavior [Van Den Bogert et al. (1989)].

1.5 Thesis Outline

The purpose of this study is to investigate a number of different aspects associated with the mechanical modeling of the feline hindlimb for both inverse and forward dynamics.

Chapter 2 describes the methods used to collect and process the kinematic data and the ground reaction force data required for this study.

Chapter 3 outlines the creation of the two-dimensional hindlimb model. The two-dimensional hindlimb model was then used in an inverse dynamics analysis to estimate the joint torques occurring within the hindlimb for walking on a level surface. The sensitivity of the estimated joint torques to variations in the centroidal moment of inertia, the masses, and the center of mass locations of each individual hindlimb segment is investigated. The joint torques estimated by the two-dimensional hindlimb model, with and without a paw, is also included.

Chapter 4 details an investigation into whether or not a planar hindlimb model can be used estimate the joint torques occurring in a feline hindlimb, since the hindlimb is actually subject to non-planar motion during typical level walking. This was determined by comparing the joint torques estimated from the two-dimensional hindlimb model to joint torques estimated from a three-dimensional hindlimb model.

In Chapter 5 the two-dimensional hindlimb model is used to perform an initial investigation into forward dynamics simulations. The estimated joint torques and the GRF's were used as the inputs with which to run the forward dynamics simulations. The predicted kinematics could then be compared to the original kinematics as a means of verifying the modeling methodology.

Conclusions and recommendations for future work in this area are presented in Chapter 6.

Chapter 2

Data Collection

In order to create a dynamic model of the hindlimb, the kinematics of the hindlimb, as well as the types of forces which act upon it, must first be studied. Here kinematics of the hindlimb refers to the positions, velocities, and accelerations, of each segment of the hindlimb. The external forces which act upon the limb must also be measured so that they may be used in conjunction with the kinematic data to estimate the forces and moments which occur within the hindlimb. For walking along a level surface, the only forces external to the hindlimb that must be measured are the ground reaction forces, or GRF's. Any drag on the hindlimb caused by air resistance may be neglected as it is extremely small in comparison to the GRF's.

This chapter outlines the methods used to obtain both the two-dimensional and three-dimensional kinematic and GRF data required for this study. The procedures used to calculate and modify the data, such as: calculation of the joint angles, differentiation of joint angle data in order to obtain angular velocities and angular accelerations, as well as interpolation and filtering of the data, are also discussed.

2.1 Data Collection Method

Currently one of the most common methods of collecting data for gait analysis is to employ the use of a video based motion capture system. A brief description of a motion capture system used to collect kinematic data for this study is included to provide the reader with some background for the data collection process. There are three main components of a video based motion capture system used for the collection of gait analysis data:

1. Video Camera.

Reflective markers are placed upon the limbs (or bodies) of interest and a video camera is used to film the subject as it moves. The video data is then digitized and transferred to a computer where the kinematic measurements are made based upon the location of the reflective markers in each frame of the digitized video data. The number of video cameras required for kinematic data collection depends on both the complexity of the movement being studied and whether or not two-dimensional or three-dimensional kinematic data is required. For gait analysis requiring two-dimensional kinematic data, a single video camera may be used. Should the motion being studied require three-dimensional kinematic measurements, a minimum of two video cameras would be required.

2. Force Plate.

Force plates are placed in the surface of the walkway upon which the subject walks to measure the GRF's between the subject's foot and the surface. The GRF's are measured in three separate directions where each direction corresponds to a single axis of an orthogonal reference frame.

3. Computer.

Computer workstations are used to record and process both the data from the video camera and the data from the force plate. A software program is used to locate the reflective markers for each frame of the video data and calculate the position of the reflective markers with respect to a user defined reference frame.

The kinematic and force data used for this study was obtained from the lab of Dr. Keir Pearson, Director for the Center of Neuroscience for the University of Alberta. The motion capture system used in Dr. Pearson's lab was purchased from Peak Performance Technologies, Inc. and utilizes Peak Motus software for the collection of the kinematic and force data. A schematic of Dr. Pearson's motion capture system is shown in Figure 2.1. The walkway is situated on top of a wheeled frame which places the walkway at approximately hip height, and is enclosed by plexi-glass walls which keep the cat from straying off of the walkway. The video camera is placed perpendicular to the walkway so that the portion of the gait cycle in which the hindlimb makes contact with

the force plate, occurs within the field of view. A gait cycle begins when one foot contacts the ground and continues until the same foot again contacts the ground. Dr. Pearson's motion capture system utilized a single video camera, therefore only two-dimensional kinematic data was available. An orthogonal right-handed global reference frame, also shown in Figure 2.1, was chosen such that the positive X-axis is aligned with the forward motion of the cat along the walkway, and the positive Z-axis is aligned vertically upwards, parallel to the direction of gravity.

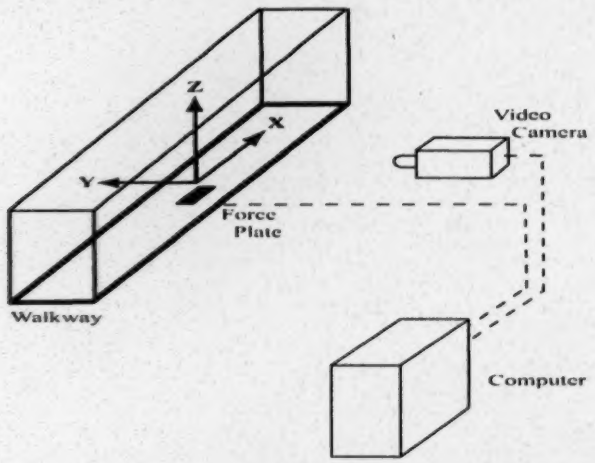

Figure 2.1: Schematic of the motion capture system. The force plate is shown as the black square embedded in the walkway.

A brief description of the data collection process for a typical gait trial is as follows. First small circular reflective markers are placed upon the shaved hindlimb of a cat, above the bony anatomical landmarks of the limb such as the hip, knee, and ankle. The motion capture system is then calibrated by placing a calibration grid along the walkway, within the field of view of the video camera. The calibration grid consists of a number of black dots that are placed upon a white background which the Peak Motus software uses as a reference on which to base it's position calculations for the kinematic measurements. The force plate is also calibrated by applying a known force in each direction while recording the output from the force plate. After the motion capture system has been calibrated, the cat is placed on the walkway and coaxed to walk from one end of the walkway to the other. As the cat nears the force plate a synchronization pulse is initiated by the operator who is collecting the data. The synchronization pulse is recorded onto both the force

plate data and the video data, and ensures the alignment of the time scales of both data files.

Once the data has been collected the Peak Motus software is used to track the reflective markers. The tracking process refers to identifying the location of the individual reflective markers in each frame of the digitized video. Once the markers have been tracked, the Peak Motus software can calculate the coordinates of each of the reflective markers for the entire trial. This set of coordinate data will be referred to as the positional data.

2.1.1 Limitations of the Motion Capture System

While the video based motion capture system is a powerful tool for conducting gait analysis investigations, there are a few drawbacks associated with it. These drawbacks are related to the use of the reflective markers as the basis for the kinematic measurements.

Since the reflective markers are placed directly upon the skin of the hindlimb, there may be some movement of the reflective markers as the skin itself is free to move relative to the skeletal system. Miller et al. (1975) investigated the amount of skin slippage which occurs about the anatomical landmarks of a feline hindlimb during locomotion on a treadmill. Small lead disk's, 4 mm's in diameter, were placed on the skin above bony anatomical landmarks of the hindlimb. X-rays of the cat's hindlimb were then taken as it walked on a treadmill. Miller et al. (1975) found that the skin remained closely related to the bony landmarks of the hindlimb in all places, except the knee. The maximum skin slippage observed at the knee over the duration of several step cycles was found to be $\approx$ 4.0 cm, the majority of which occurred along the axis of the shank segment of the hindlimb. Upon inspection of the kinematic data collected from Dr. Pearson's motion capture system, slippage of the knee marker was also observed as maximum variations of 0.9 cm, and 2.6 cm were observed in the lengths of the thigh and shank segments of the hindlimb. To correct for this variation in the hindlimb segment lengths, the mean length of each hindlimb segment was calculated from the positional data. The calculated mean hindlimb segment lengths were then used as the actual hindlimb segment lengths for the calculation of the joint angles as well as for the two-dimensional model.

The second drawback related to the use of the reflective markers is the limitation on the motion that can be measured due to the physical size of

the different anatomical structures. While the use of the reflective markers work reasonably well for the larger limb segments, such as the thigh, shank, and tarsals, the motion of much smaller limb segments, such as the individual phalanges (the bones of the paw and digits) cannot be measured. The markers used to collect the kinematic data for this study were quite large in comparison to the phalanges, thus the reflective markers would not provide adequate resolution to accurately measure the motion of the phalanges. Thus, there is also no detailed kinematic information available for the individual phalanges of the paw. A single reflective marker was affixed to the middle of the paw for the kinematic measurements, however the paw marker only provides a general representation of the location of the paw during the gait cycle.

A simple test was conducted in which the positions of four stationary reflective markers were manually measured and compared to the locations of the reflective markers as measured by the motion capture system to investigate the error, if any, in the measurements made by the motion capture system. A maximum error of 0.21 cm was found in the measurement of the reflective marker positions made by the motion capture system. This measurement error is fairly small when compared to the error introduced by the movement of the reflective markers due to the skin slippage, which can be as high as 4 cm's. The details of the test can be found in Appendix A.

2.2 Kinematic and Ground Reaction Force Data

Before proceeding there are a few commonly used terms associated with gait analysis which should be defined. The gait cycle, previously defined as the movement which occurs between two successive contacts with the ground, can be divided into two distinct phases. The stance phase begins when a leg initially comes into contact with the ground, and continues until the leg loses contact with the ground. Once the leg loses contact with the ground, the leg enters into the swing phase which continues until the onset of the next stance phase. The swing and stance phases are shown in Figure 2.2.

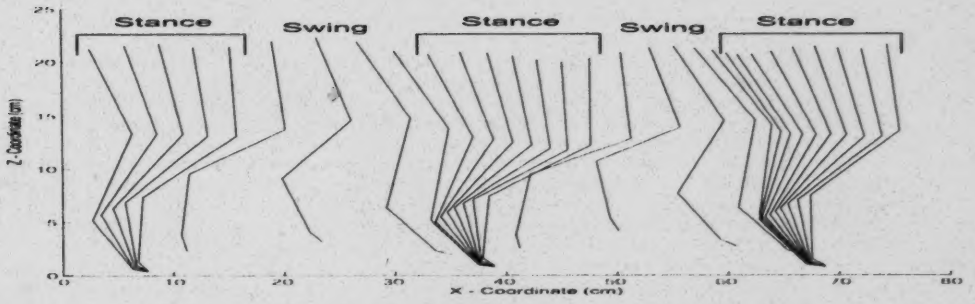

Figure 2.2: Gait cycles for a typical hindlimb. The stance phase and swing phase portions of the gait cycle are indicated.

2.2.1 Two-Dimensional Kinematic Data

The positional data is a subset of the kinematic data as it represents the locations of each of the reflective markers calculated by the motion capture system. Occasionally the positional data will be referred to directly to distinguish it from the angular kinematic data which consists of the angular positions, angular velocities, and angular accelerations of the hindlimb segments. The positional data for the hindlimb of a typical cat is shown in Figure 2.3. The reflective markers (A to E) are plotted with respect to their X and Z coordinates, and are connected by line segments to aid in the visualization of the limb's motion. The Peak Motus software uses a Butterworth filter for the filtering of the positional data. The order and cut-off frequency for the Butterworth filter are chosen automatically by the Peak Motus software and are not included in the data.

Only a portion of the positional data, as indicated in Figure 2.3, was used for the study. Since a single force plate was used, only the GRF's for a single stance phase of the hindlimb could be recorded. Without the GRF's the internal moments and forces which occur in the hindlimb at each joint during the stance phase can not be estimated. Therefore only the positional data for the swing phase prior to the stance phase, and the swing phase immediately following the stance phase for which the GRF's were recorded, was used. Therefore the kinematic data set consisted of a pre-stance swing phase, the stance phase, and a post-stance swing phase.

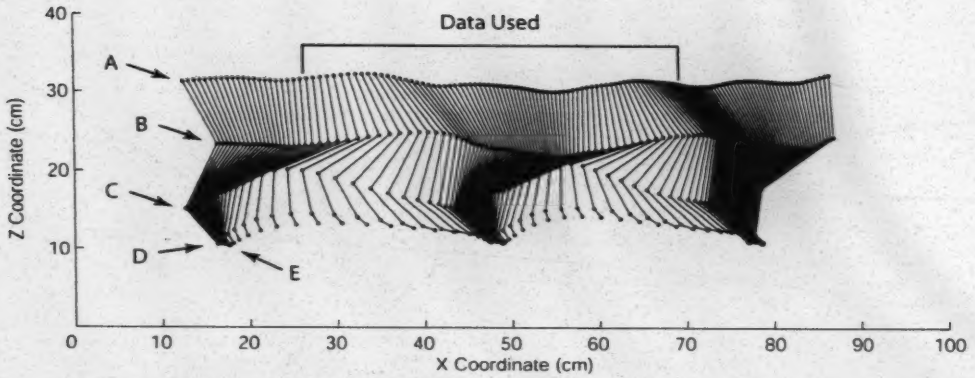

Figure 2.3: Positional data for a cat hindlimb captured at 60 Hz. Each hindlimb position shown represents and interval of $\frac{1}{60}$ s. Each dot represents a reflective marker, where: A = Hip, B = Knee, C = Ankle, D = MTP, and E = Paw.

Goslow et al. (1973) measured the duration of the step cycle for the unrestrained walking, trotting, and galloping of 11 adult cats. They found that for a cat walking at 2 mph (which was the slowest walking speed studied) the duration of a complete step cycle for the hindlimb was 700 ms, where the swing phase lasted 225 ms, while the stance phase lasted 475 ms. Comparatively for the fastest galloping speed studied of 16 mph, the duration of a complete step cycle was reduced to 290 ms where the swing phase decreased slightly to 200 ms and the stance phase was reduced quite drastically to 90 ms. Goslow et al. (1973) showed that over a relatively large range of locomotion speeds ($2 - 16$ mph) the duration of the swing phase for a cat's hindlimb remains relatively constant, while the duration of the stance phase decreases rather dramatically.

For the trial shown in Figure 2.3 the duration of each step cycle was $\approx$ 915 ms, where the swing phase lasted $\approx$ 230 ms, which is very close to the duration of the swing phase of the cat walking at 2 mph observed by Goslow et al. (1973). The stance phase for the trial shown in Figure 2.3 lasted $\approx$ 685 ms. The hindlimb moves the fastest during the swing phase which can be inferred from Figure 2.3. The kinematic data was recorded at a constant 60 Hz and during the swing phases the positions of the hindlimb become more spread out from one another, indicating that the limb is moving faster. The 230 ms duration of the swing phase corresponds to the hindlimb moving at $\approx$ 4.3 Hz. Since the video camera of the motion capture system recorded the positional data at 60 Hz, the sampling rate is then 14 times faster than the

motion being filmed. According to the Sampling Theorem [Shannon (1949)], the sampling frequency must be at least twice as fast the data being sampled. Therefore the 60 Hz sampling rate should be more than adequate to provide an accurate representation of the positional data.

While the positional data was collected at 60 Hz, resulting in a time step of $\frac{1}{60}$ s between each data point, the GRF data was collected at 600 Hz, resulting in a time step of $\frac{1}{600}$ s between each data point in the GRF data sets. In order to simplify working with both the positional and GRF data sets a time step of 0.001 s was chosen and both the positional and GRF data sets were interpolated using cubic spline interpolation. This ensured that the positional data and the GRF data sets were the same size, and shared the same time interval. While a time step of $\frac{1}{600}$ may seem to be a more obvious choice, thus negating the need to interpolate the GRF data sets, the time step of 0.001 s was chosen since it is easier to work with. Also, since the forward dynamics simulations utilize an adaptive step size integrator, the smaller time step should reduce the number of interpolations required during the integration process thereby reducing the time needed to run a forward dynamic simulation.

The angles which described the location of each hindlimb segment were calculated using Equation 2.1, and the X and Z coordinates of the hip, knee, ankle, metatarsalphalangeal (or MTP), and paw reflective markers.

$$\Theta_i = \arctan\left(\frac{x_{i+1} - x_i}{z_{i+1} - z_i}\right) \tag{2.1}$$

where: i = $1, 2, 3, 4$
x, z = coordinates of the reflective markers

Since each of the angles are measured at one of the hindlimb's joints, they are referred to as the joint angles. Figure 2.4 illustrates how the joint angles used to describe the location of each hindlimb segment are defined. The hip, knee, ankle, and MTP joint angles are represented in Figure 2.4 by Θ_1, Θ_2, Θ_3 and Θ_4 respectively. Each joint angle is measured relative to the negative Z-axis of the global coordinate system, where the positive direction of each angle is defined as being clockwise.

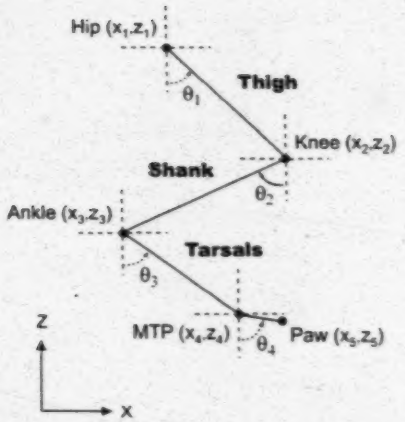

Figure 2.4: Definition of the joint angles. Positive and negative joint angle directions are shown with the solid (clockwise) and dashed (counterclockwise) arrows respectively. All joint angles are measured relative to the negative Z-axis.

The angular velocities and angular accelerations of each hindlimb segment were calculated using the central difference formulas shown in Equations 2.2 and 2.3.

$$\dot{\Theta}_{(i)} = \frac{\Theta_{(i+1)} - \Theta_{(i-1)}}{2\Delta_t} \tag{2.2}$$

$$\ddot{\Theta}_{(i)} = \frac{\dot{\Theta}_{(i+1)} - \dot{\Theta}_{(i-1)}}{2\Delta_t} \tag{2.3}$$

where:
Θ = Angle
$\dot{\Theta}$ = Angular Velocity
$\ddot{\Theta}$ = Angular Acceleration
i = $(2, 3, 4, \ldots, n-1)$
n = number of data points in data set
Δ_t = time step

While other alternative differentiation techniques could have been used, the central difference method was chosen for it's simplicity and because it allows the angular velocities and accelerations to be calculated at the same discrete time steps as the original joint angle data. A problem that can occur when using the central difference method is that for a discrete data set of size $i = 1 \ldots n$, the first value ($i = 1$) and the last value ($i = n$) in the data set can not be differentiated. This is a result of the central difference equations requiring information about the values which either precede or follow the value at the location where the differentiation is to take place. However since the entire positional data set was not required, due to the GRF's being collected for a single stance phase as mentioned earlier, this problem was avoided.

The joint angles for the hip, knee, and ankle joints, estimated from the positional data set, are shown in Figure 2.5. The MTP joint angle is not included since, as mentioned in Section 2.1.1, the paw marker only provides a very general representation of the location of the paw and is not required, as will be discussed in Chapter 3, Section 3.2.

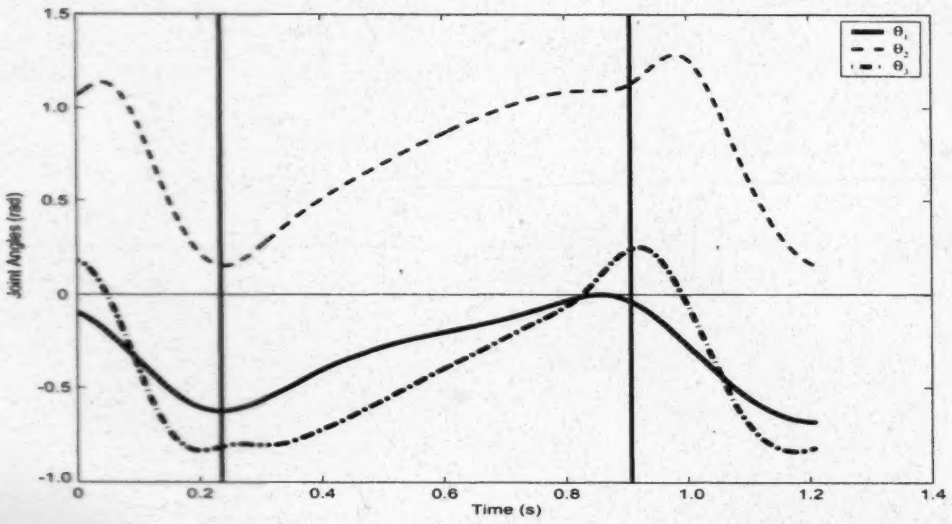

Figure 2.5: Estimated joint angles. Θ_1, Θ_2, and Θ_3 represent the hip, knee, and ankle joint angles, respectively. The two vertical lines represent the transitions from swing phase to stance phase (0.23 s), and stance phase to swing phase (0.92 s).

The estimated angular velocities are shown in Figure 2.6, while the estimated angular accelerations are shown in Figure 2.7. The angular velocities ($\dot{\Theta}_1$, $\dot{\Theta}_2$, $\dot{\Theta}_3$), and angular accelerations ($\ddot{\Theta}_1$, $\ddot{\Theta}_2$, $\ddot{\Theta}_3$) of each limb segment adhere to the same sign convention as the joint angles. As mentioned earlier Goslow et al. (1973) found that as the forward speed of the cat increased, the time that it took to complete one step cycle decreased, where the majority of the decrease in step cycle duration came from the decrease in the duration of the stance phase. Alternatively for slower locomotion the duration of the stance phase is increased while the duration of the swing phase changes very little. The cat from which the positional data was collected was travelling at a relatively slow, self-selected walking speed (approximately 0.70 mph). Therefore it is not surprising that the hindlimb moves much more slowly during the stance phase as shown in Figures 2.6, and 2.7.

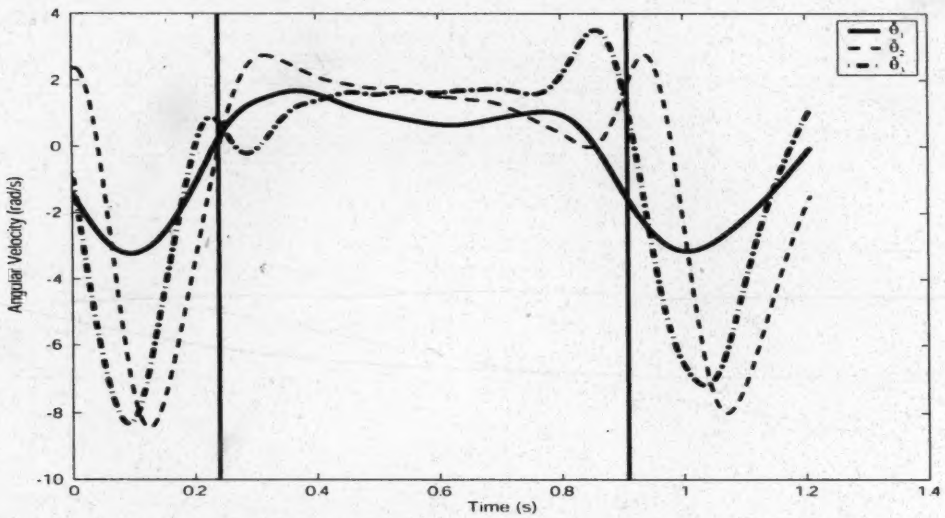

Figure 2.6: Estimated angular velocities. $\dot{\Theta}_1$, $\dot{\Theta}_2$, and $\dot{\Theta}_3$ represent the respective hip, knee, and ankle angular velocities. The two vertical lines represent the transitions from swing phase to stance phase (0.23 s), and stance phase to swing phase (0.92 s).

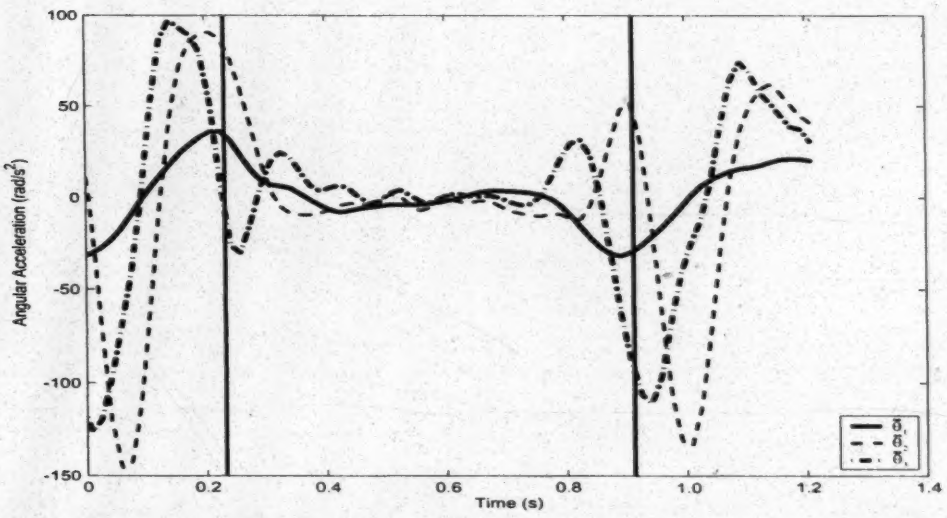

Figure 2.7: Estimated angular accelerations. $\ddot{\Theta}_1$, $\ddot{\Theta}_2$, and $\ddot{\Theta}_3$ represent the respective hip, knee, and ankle angular accelerations. The two vertical lines represent the transitions from swing phase to stance phase (0.23 s), and stance phase to swing phase (0.92 s).

As mentioned earlier in Section 2.1.1 there was some movement of the knee reflective marker observed in positional data. To minimize the effect of the marker movement the location of the knee marker is often estimated by triangulating it's location based upon the location of the hip and ankle markers and the known lengths of the thigh and shank segments (Buford et al. (1990); Carlson-Kuhta et al. (1998); Fowler et al. (1993); Goslow et al. (1973); Shen and Poppele (1995)). As a investigation to see how triangulating the location of the knee marker would affect the joint angle data, the location of the knee marker was calculated using the hip and ankle marker locations and the mean lengths of the thigh and shank segments, as calculated from the positional data. The resulting angular kinematic data is shown in Figures 2.8 to 2.10. As shown in Figure 2.8 the differences between the hip and knee joint angles occur during the swing phases and the transition from stance phase to swing phase. The differences in the hip joint angles are larger than the differences in the knee joint angles, however the profiles of the joint angle curves estimated using the triangulated knee marker position remain quite similar to the original kinematic data. Similarly, the angular velocities and angular accelerations shown in Figure 2.9 and Figure 2.10 respectively, also are fairly similar to the angular velocities and angular accelerations shown in Figures 2.6 and 2.7.

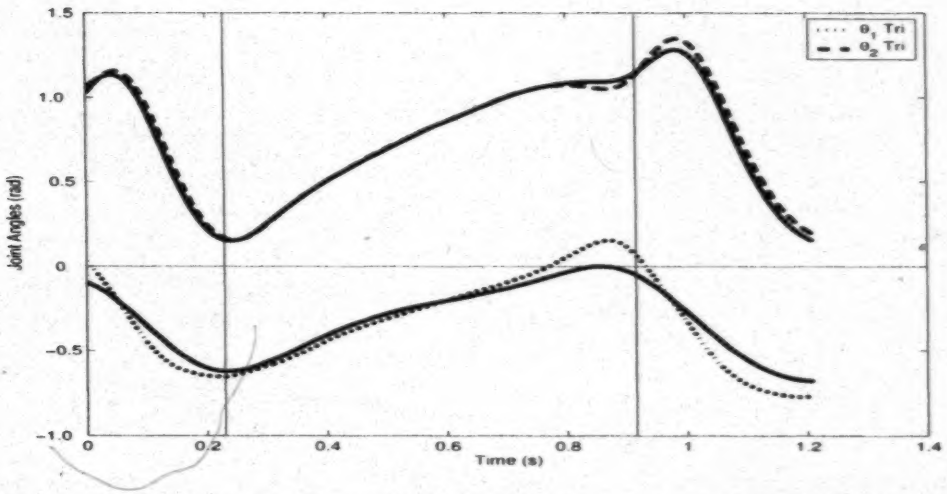

Figure 2.8: The hip and knee joint angles calculated using the triangulated position of the knee marker, Θ_1 Tri and Θ_2 Tri respectively, are shown plotted over the hip and knee joint angles (solid lines) shown in Figure 2.5.

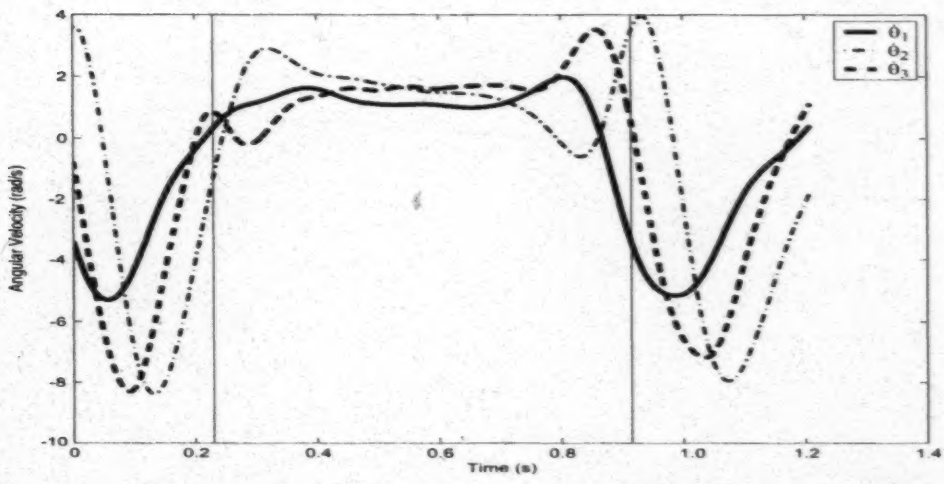

Figure 2.9: Angular velocities calculated using the triangulated position of the knee marker.

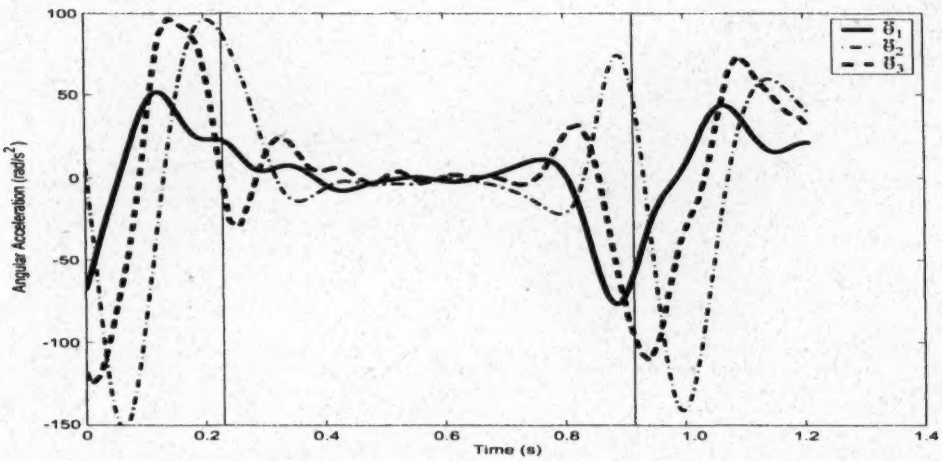

Figure 2.10: Angular accelerations calculated using the triangulated position of the knee marker.

An assumption of the triangulation method is that the lengths of the thigh and shank segments are known, as they are measured directly from the cat. In this investigation the actual thigh and shank segment lengths were unknown as they were not available. Instead the mean lengths of the thigh and shank segments calculated from the positional data were used. Thus, while the joint angles calculated with the triangulated knee joint marker position may be more consistent because the lengths of the thigh and shank segments do not change, there is no way to be sure that joint angles calculated from the triangulated knee marker locations are any more accurate than joint angles calculated directly from the positional data. Therefore the joint angles calculated with the triangulated knee marker locations were not used in this study.

2.2.2 Three-Dimensional Kinematic Data

In order to investigate if there were any significant differences between the joint torques estimated by a two-dimensional hindlimb model and the joint torques estimated by a three-dimensional hindlimb model, a three-dimensional kinematic data set was also required. However, as mentioned earlier, Dr. Pearson's motion capture system was only set up to obtain two-dimensional positional data. Fortunately an associate of Dr. Pearson, Dr. John Misiaszek, who is an Associate Professor in the Department of Occupational Therapy at the University of Alberta, studied three-dimensional movement of feline hindlimbs. Dr.

Misiaszek studies investigated the amount of adduction and abduction of the hip during the gait cycle. When viewing the cat from behind, adduction refers to motion at the hip which moves the limb closer to the body, while abduction refers to motion at the hip that moves the limb out laterally, farther away from the body. Unfortunately Dr. Misiaszek was only interested in the hip adduction and abduction motion and did not collect any positional data for the knee or ankle, nor did he collect any GRF's. Since a complete three-dimensional kinematic data set could not be obtained, and approximated three-dimensional kinematic data set was created by combining a two-dimensional kinematic data set with an approximated hip adduction and abduction data set. The approximation of the hip adduction and abduction data will be discussed later in this section.

An additional positional data set was obtained from Dr. Pearson for which a three-dimensional GRF data set was also collected. The new two-dimensional positional data set is shown in Figure 2.11, where the positions of the reflective markers have been connected with lines to aid in the visualization of the limbs motion. Once again only the kinematic data of the swing phases prior to, and immediately following the stance phase for which the GRF's were recorded, were used. The joint angles, angular velocities, and angular accelerations were all calculated using the same procedures as outlined for the first kinematic data set in Section 2.2.1, and are shown in Figures 2.12 to 2.14.

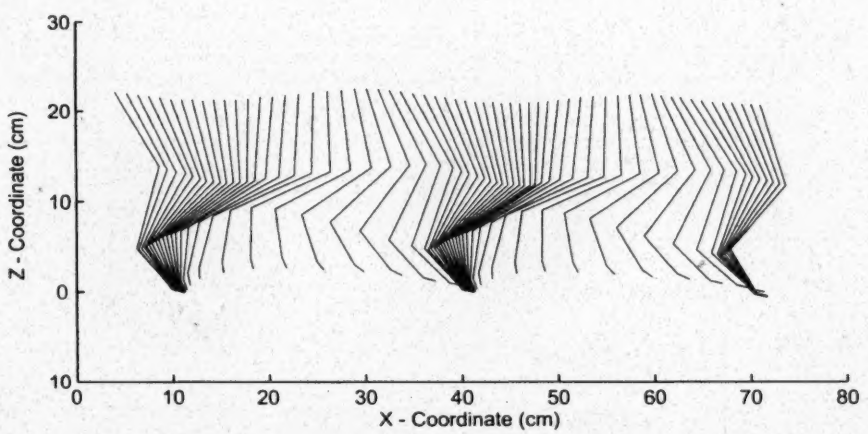

Figure 2.11: Plot of the positional data. Each hindlimb position shown represents an interval of $\frac{1}{60}$ s.

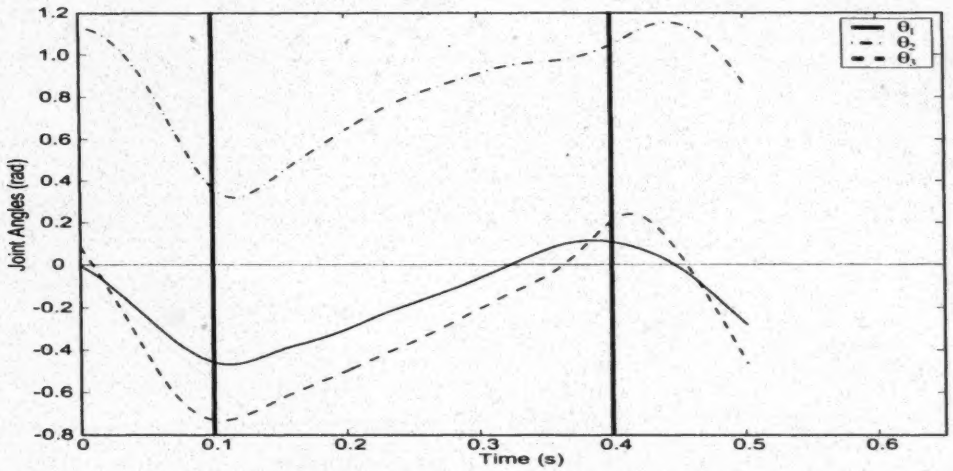

Figure 2.12: Estimated joint angles. Θ_1, Θ_2, and Θ_3 represent the hip, knee, and ankle joint angles, respectively. The two vertical lines represent the transitions from swing phase to stance phase (0.10 s), and stance phase to swing phase (0.40 s).

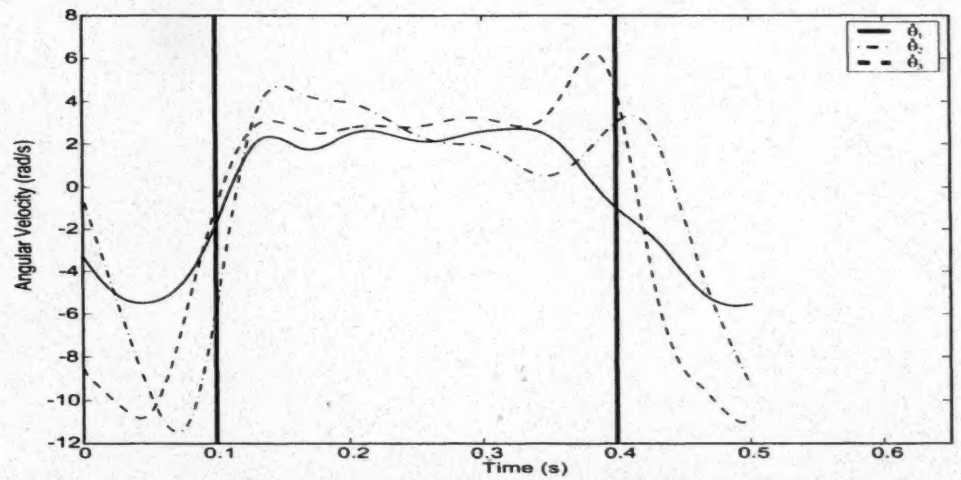

Figure 2.13: Estimated angular velocities. $\dot{\Theta}_1$, $\dot{\Theta}_2$, and $\dot{\Theta}_3$ represent the respective hip, knee, and ankle angular velocities. The two vertical lines represent the transitions from swing phase to stance phase (0.10 s), and stance phase to swing phase (0.40 s).

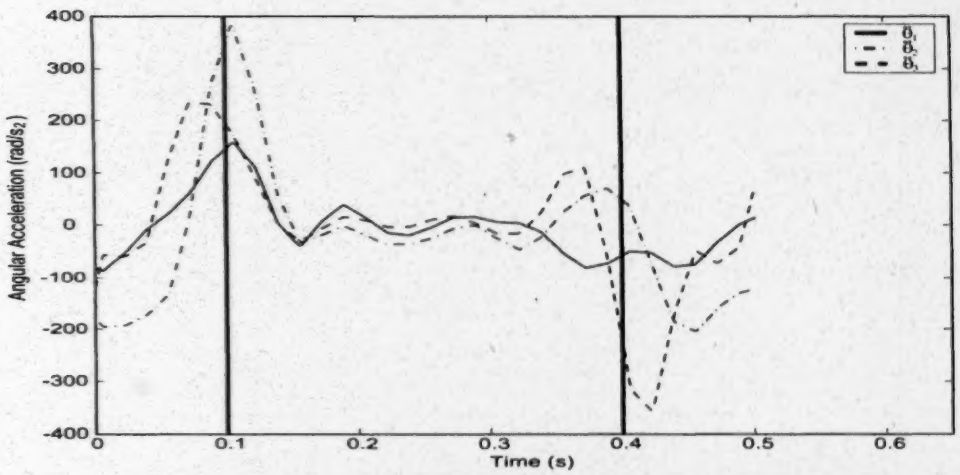

Figure 2.14: Estimated angular accelerations. $\ddot{\Theta}_1$, $\ddot{\Theta}_2$, and $\ddot{\Theta}_3$ represent the respective hip, knee, and ankle angular accelerations. The two vertical lines represent the transitions from swing phase to stance phase (0.10 s), and stance phase to swing phase (0.40 s).

The joint angles of the first kinematic data set (shown in Figure 2.5) and the second kinematic data set (shown in Figure 2.12) are quite similar to one another as they share the same characteristic shapes. There is some variability between the two joint angle data sets with respect to the magnitudes of each of the joint angles. Since a different animal was used to obtain each kinematic data set variability between the two data sets should be expected because the hindlimb segment lengths and gait patterns of the two animals may differ from one another. The main difference between the second kinematic data set and the kinematic data set used in Section 2.2.1 is the speed of locomotion. In the second kinematic data set (shown in Figure 2.11) the swing phases are 0.15 s in duration, while the stance phase lasts 0.3 s, both of which are approximately one half the duration of the swing and stance phases of the kinematic data in Figure 2.5. Thus the cat from which the new data was collected was moving approximately twice as fast as the cat from which the first data was collected. This is readily apparent in the larger magnitudes of the angular accelerations of the second kinematic data set shown in Figure 2.14. The most noticeable difference is the large spike in the magnitude of the knee angular acceleration at 0.1 s which is approximately four times larger than the comparable magnitude of the knee angular acceleration observed from the first kinematic data set, shown in Figure 2.7.

Hip Adduction and Abduction

Dr. Misiaszek was gracious enough to provide five separate hip adduction and abduction data sets. Dr. Misiaszek also uses a Peak Motus motion capture system for his data collection, similar to Dr. Pearson's, with the exception that Dr. Misiaszek's system is set up to measure three-dimensional kinematic data. Reflective markers were placed on the head, the shoulders and paws of the forelimbs, as well as the hips and MTP joints of the cat's hindlimbs.

Over the duration of a complete gait cycle the hip joint transitions through both adduction and abduction. Θ_a represents the adduction and abduction angle as shown in Figure 2.15. Abduction of the hindlimb occurs during the swing phase as the hindlimb swings out from the body. During the stance phase the hip joint undergoes adduction wherein the hip moves out laterally over the paw, which is also shown in Figure 2.15.

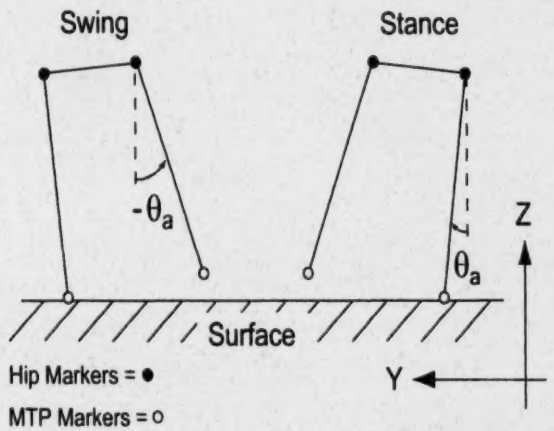

Figure 2.15: Abduction and adduction of the hip joint during the swing and stance phases. Abduction is represented by a negative Θ_a while adduction is represented by a positive Θ_a. Θ_a is measured relative to the negative Z axis.

After analyzing the five data sets provided by Dr. Misiaszek, the mean peak abduction at the hip joint during the swing phase was found to be 6° ($\Theta_a = -6°$), while mean peak adduction of the hip joint was found to be 4°

($\Theta_a = 4°$) during the stance phase. In each of the data sets the transitions between the stance and swing phases occurred when Θ_a was approximately 0°. Thus the hindlimb is very near perpendicular to the surface when lifting off or touching down on the surface. One of the trials obtained from Dr. Misiaszek for the adduction and abduction motion of the hindlimb is shown in Figure 2.16. A sine curve was fitted to the sample abduction and adduction data to highlight the repeating pattern of the sample data, which was a trend observed in all of the abduction and adduction angular data obtained from Dr. Misiaszek. The data set shown in Figure 2.16 differs slightly from the other adduction and abduction data sets since the magnitudes of the abduction and adduction are almost the same. In each of the other trials the peak magnitude of the abduction angles are slightly larger, by up to 4 degrees, than the peak magnitude of the adduction angles.

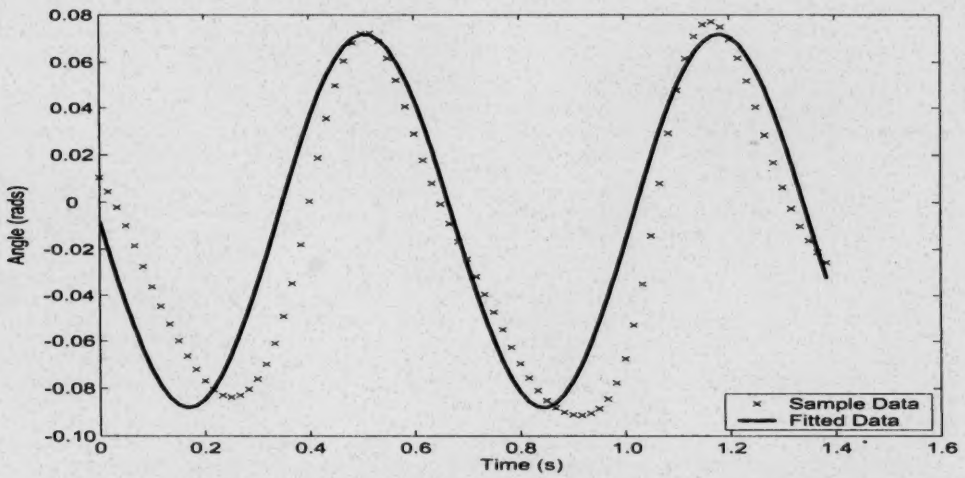

Figure 2.16: Sample hip adduction and abduction angle data. A sine curve was fitted to the sample data to highlight the repeating pattern observed in the sample data.

Since the hip adduction and abduction data sets were obtained from cats walking at self selected speeds the length of each data set, as well as the magnitudes of the hip adduction and abduction angles between each of the data sets, varied from one another. In order to obtain a hip abduction and adduction data set that matched the time interval of the second kinematic data set obtained from Dr. Pearson an approximate adduction and abduction data set, which will referred to as the Θ_a data set, was created based on the mean peak

adduction and abduction angles. The durations of the swing and stance phases were calculated from the second set of GRF data obtained from Dr. Pearson. Ideally a single sine curve would be used for the approximation. However, as mentioned earlier the amplitudes of the hip adduction and abduction phases differed from one another, thus a single sine curve would not provide an accurate representation. Therefore a combination of sine and cosine curves were used to create an approximation of the adduction and abduction motion.

The different amplitudes of the sine and cosine curves used for the approximated data set, created discontinuities at the transitions between the abduction and adduction phases when combined together to create a single data set. If the approximated data for Θ_a was differentiated with the discontinuities at the transitions between the adduction and abduction phases, very large and unrealistic changes in the magnitudes of the angular velocities and angular accelerations would be observed. To solve the problem of the discontinuities at the transition points between the swing and stance phases, a sixth order polynomial which was the lowest order polynomial that provided a reasonable fit to the data as observed by the author, was fitted to the approximated data set. The result of using the sixth order polynomial is a smooth, continuous data set for the approximated Θ_a motion. the use of the polynomial also ensured that $\dot{\Theta}_a$ and $\ddot{\Theta}_a$, which are the angular velocities and angular accelerations respectively for the hip adduction and abduction motion, were smooth and continuous.

Admittedly the approximated data set for the abduction and adduction motion of the hip is somewhat idealized. As shown in Figure 2.16, the magnitudes of the hip adduction and abduction motion vary slightly from peak to peak. Also when increasing in magnitude the slope of the sample data appears to be slightly steeper than the slope of the sample data when the magnitude is decreasing.However this approach provides an acceptable approximation for this study. Figures 2.17, 2.18, and 2.19, show the angular data set, angular velocity data set, and the angular acceleration data set, respectively for the approximated adduction and abduction motion of the hindlimb.

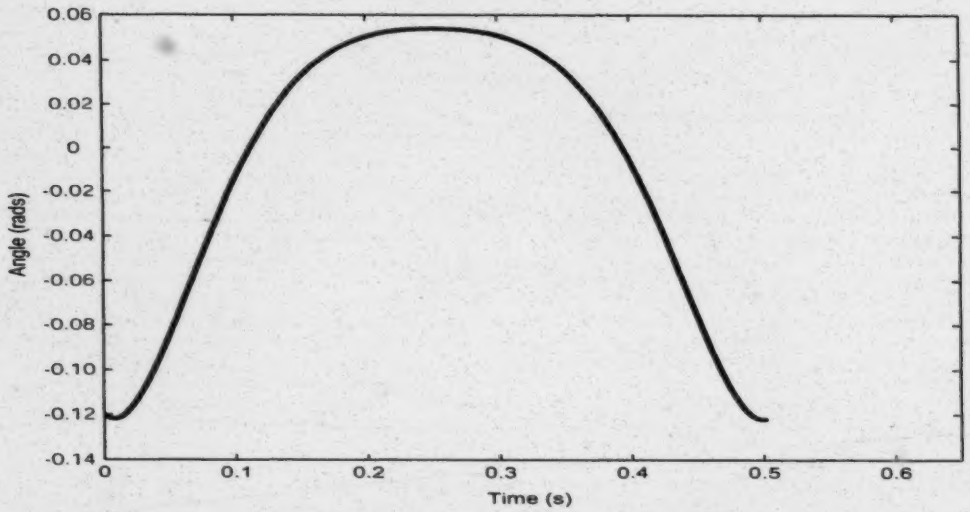

Figure 2.17: Approximated hip adduction and abduction angle, Θ_a. Adduction of the hip is positive, while abduction of the hip is negative.

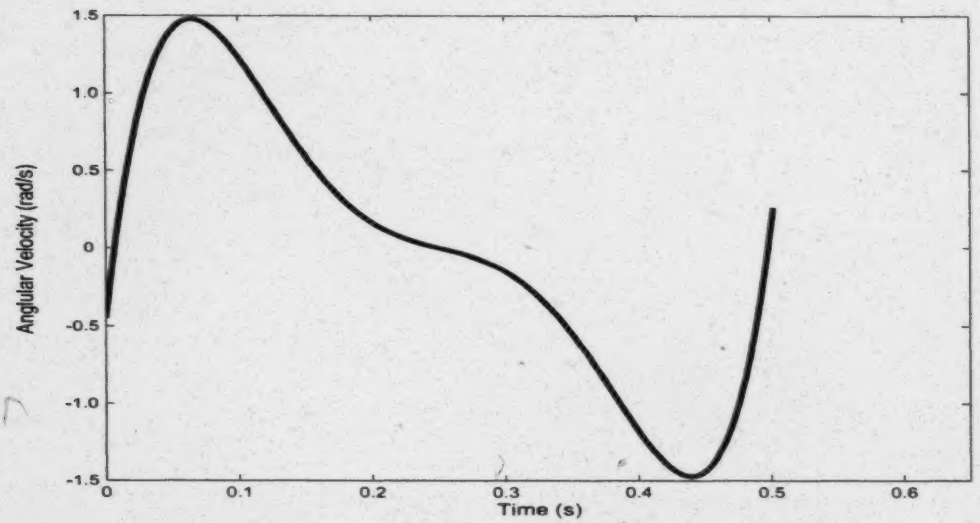

Figure 2.18: Approximated hip out-of-plane angular velocity, $\dot{\Theta}_a$.

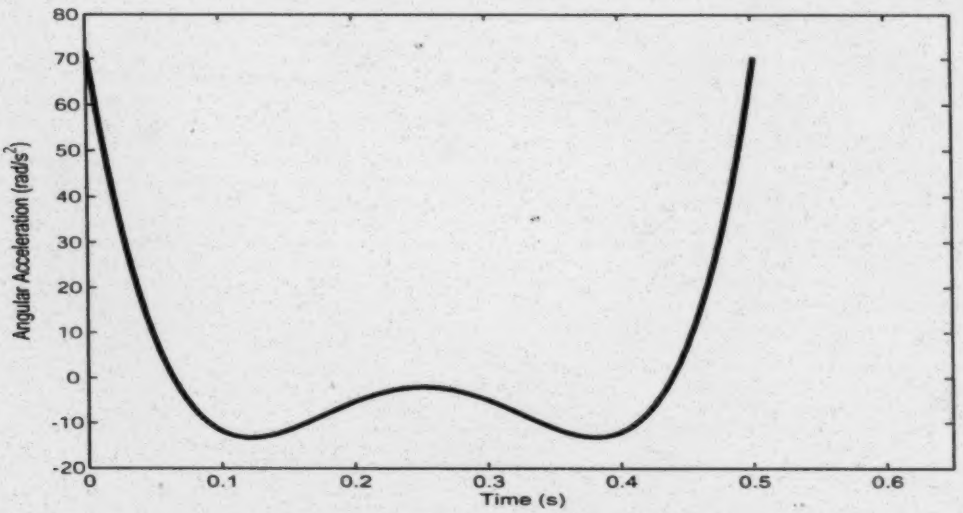

Figure 2.19: Approximated hip out-of-plane angular acceleration, $\ddot{\Theta}_a$.

2.2.3 Two-Dimensional Ground Reaction Forces

Inspection of the raw force plate signals, shown in Figure 2.20, revealed a noticeable amount of noise in the signals. The source of the noise in the signals may have been caused by the force plate measuring vibrations in the building or the walkway itself. Additionally, there may have been some environmental electrical or magnetic interference with the analog force plate signals which is a common source of noise in analog signals. The noise in the raw force plate signals was removed by filtering the raw force plate signals with a digital, low pass, third-order Butterworth filter using a cutoff frequency of 15 Hz. A number of different cutoff frequencies and filter orders were tried until the results of the filtering process appeared sufficiently smooth upon visual inspection. To ensure that the chosen cutoff frequency did not remove any higher frequency components of the force plate signals resulting in a loss of information from the force plate signal, a fast fourier transform of the force plate signal was performed. Upon inspection of the fast fourier transform it was determined that the majority of the power of the force plate signals occurred below 8 Hz, thus the chosen cutoff frequency should not significantly affect the results.

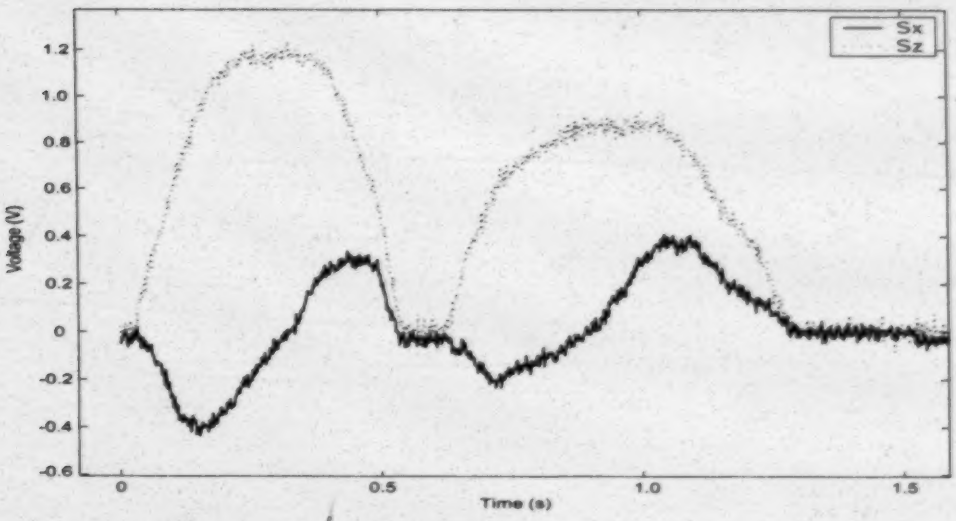

Figure 2.20: Raw force plate signals. A single step for both the left front limb and the left hindlimb is shown. Sx is the force plate signal in the X-direction, while Sz is the force plate signal in the Z-direction.

A common problem encountered when filtering data is the occurrence of a phase shift, which is a translation of the filtered data along the time axis. To ensure that the force plate signals were not affected by a phase shift they were first filtered in the forward direction and then immediately filtered again in the reverse direction, with the same filter. Usually when data is filtered the filtering process begins with the initial value the data set and proceeds through until the end of the data set. Filtering in the reverse direction infers that the filtering process starts with the last value in the data set, and works backwards towards the first value. The result of the dual-direction filtering is zero-phase shift in the filtered data, as well as a doubling of the filter order [Winter (1979)]. Due to the dual direction filtering the filter order was doubled from a third-order butterworth filter, to a sixth-order Butterworth filter. The filtered force plate signals are shown plotted over top of the unfiltered signals in Figure 2.21.

After the filtering process was completed the force plate signals were converted from voltages to forces using calibration factors obtained from the force plate calibration of 0.6 N/V and 1.3 N/V, for the X and Z directions respectively. The ground reaction force in the Z-direction (GRFz) was defined to be positive when aligned with the positive Z-axis of the global reference frame.

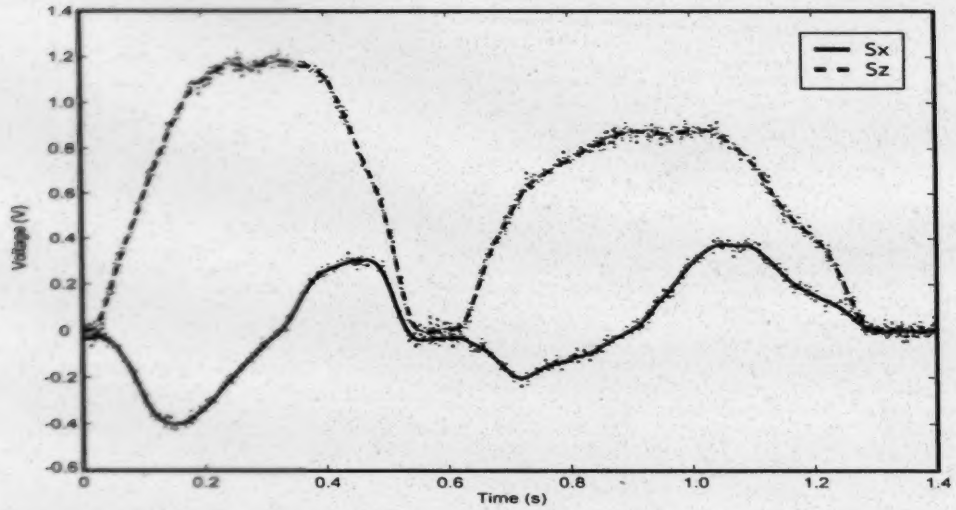

Figure 2.21: Filtered and unfiltered force plate signals. Sx is the force plate signal in the X-direction, while Sz is the force plate signal in the Z-direction.

Similarly the ground reaction force in the X-direction (GRFx) was defined to be positive when aligned with the positive X-axis of the global reference frame. The GRF's that were recorded contained data for both a forelimb and a hindlimb, as can be seen by the multiple peaks in force plate signal in the Z-direction (Sz) in Figure 2.21. Since only the hindlimb GRF data was of interest, the forelimb GRF data was removed.

The precise times at which touch-down and lift-off occurred, which are defined as the points at which hindlimb comes into contact, and loses contact with the surface, were determined through inspection of the GRFz data. Due to the noise in the force plate signal there was some fluctuation in the GRFz data about zero when the hindlimb was not in contact with the ground, even after filtering. The fluctuation in the force plate signals when there was no contact between the force plate and the cat, may be attributed to the force plate measuring vibration in the walkway, or noise in the signal. From a physical standpoint no GRF's should be applied to the limb outside of the stance phase, since the limb is no longer in contact with the surface. Once the touch-down and lift-off times were determined all of the GRF data before the hindlimb touched down, and after the hindlimb lifted off, was set equal to zero.

Figure 2.22 shows both GRFx and GRFz after processing. The rapid rise, plateau, and rapid fall in GRFz over the duration of the stance phase occurs since the hindlimb must momentarily support a portion of the cat's body-weight. The positive value of GRFz indicates the force which the ground must apply to the cat's paw in order to counteract the weight that is being supported by the paw. For this study GRFz will always be positive since a negative GRFx would indicate that there was some sort of adhesive force between the paw and the surface, which was not the case. Compared to the magnitude of GRFz, GRFx remains much smaller over the duration of the stance phase. What really distinguishes GRFx from GRFz is the change in direction in which GRFx is applied during the stance phase. Initially GRFx is negative, indicating a force that opposes the cat's direction of motion, which can be viewed as a friction or braking force. If the friction force was not present the paw would slip forward during the initial contact with the ground. Part way through the stance phase GRFx changes signs and becomes positive for the remainder of the stance phase. The positive value of GRFx indicates a force that acts in the same direction as the motion of the cat, and can be thought of as a propulsive force.

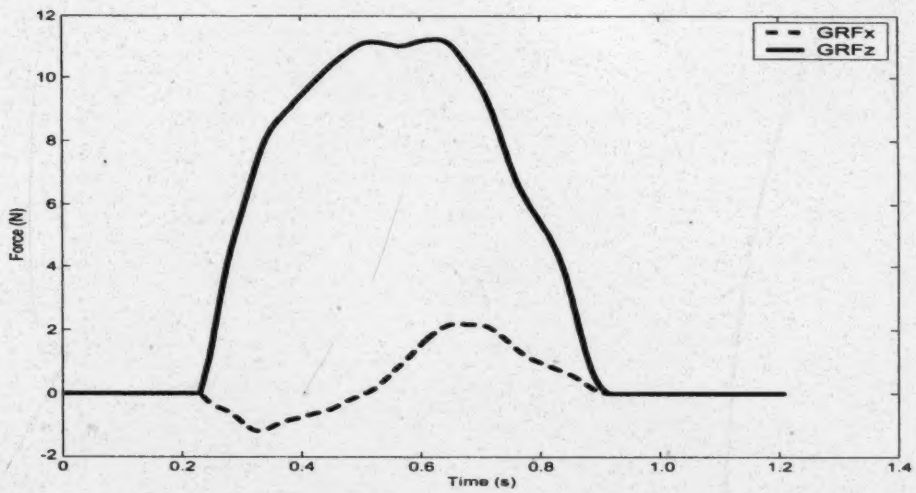

Figure 2.22: Two dimensional hindlimb ground reaction forces. GRFx is the ground reaction force in the X-direction, while GRFz is the ground reaction force in the Z-direction.

2.2.4 Three-Dimensional Ground Reaction Forces

The three-dimensional GRF data obtained from Dr. Pearson were processed using the same methods which were used for the two-dimensional GRF's in Section 2.2.3, and are shown in Figure 2.23.

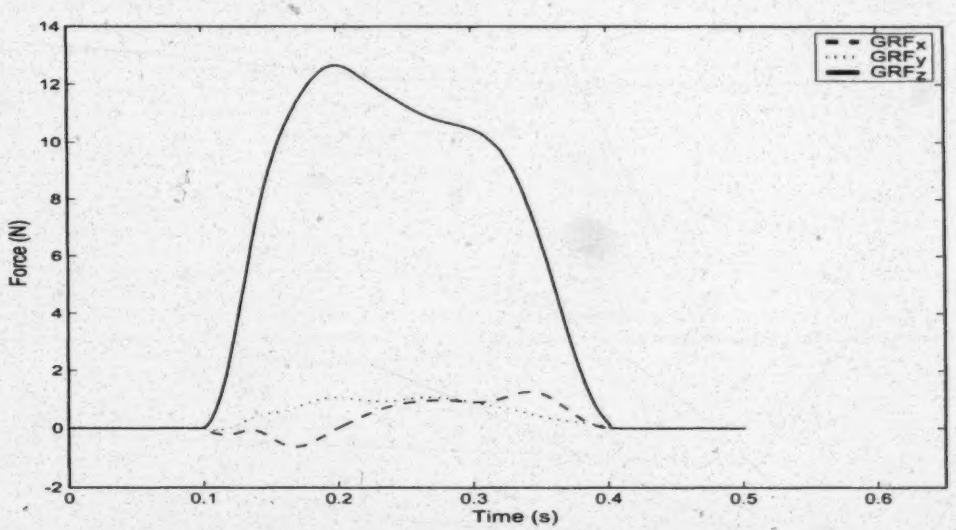

Figure 2.23: Three dimensional hindlimb ground reaction forces. GRFx, GRFy, GRFz are the ground reaction forces in the X, Y, and Z directions respectively.

During the initial portion of the stance phase the three-dimensional GRFz undergoes a rapid rise in magnitude. Unlike the two-dimensional GRFz, a more pronounced peak can be observed in the three-dimensional GRFz during the initial portion of the stance phase, however this may be due to the faster speed of locomotion of the cat for which the three-dimensional GRF data was collected. A gradual drop in the magnitude of the three-dimensional GRFz occurs over the main portion of the stance phase followed by a rapid drop in the magnitude near the end of the stance phase. Like the two-dimensional GRFx, the three-dimensional GRFx acts as a braking force over the initial portion of the stance phase before switching to a propulsive force for the remainder of the stance phase, however the braking and propulsive portions of the three-dimensional GRFx are not as pronounced as is observed in the two-dimensional GRFx. The differences between the two-dimensional and three-dimensional GRFx and GRFz data sets occur mainly in the magnitudes and shapes of

the force curves, however they both share the same underlying characteristics. The differences observed between the two-dimensional and three-dimensional GRF data sets can be attributed to variations in the gait, such as speed of locomotion, between the two animals from which the GRF data was collected.

The third GRF is GRFy, and like GRFx and GRFz it is defined as being positive when aligned with the positive Y-axis of the global reference frame. As shown in Figure 2.23 GRFy gradually increases in magnitude over the initial portion of the stance phase, it then plateaus and stays relatively constant over the mid-portion of the stance phase before gradually decreasing back to zero over the last part of the stance phase. GRFy remains positive over the duration of the stance phase. Intuitively this makes sense since during the stance phase the hip moves laterally out over the paw. The hip must then provide a torque which acts about the negative X-axis to prevent the hip from moving out too far in the lateral direction, thereby preventing the cat losing it's balance and falling over on it's side. The result of the negative hip torque is that the paw pushes out laterally in the negative Y-direction, so the ground must supply a force acting in the positive Y-direction.

2.2.5 Limitations of the Force Plate Measurements

During contact with the ground the GRF's are transferred through the portion of the paw that is in contact with the ground. The paw acts as a compliant platform that can change it's shape in order to provide a stable base of support between the limb and the surface. Contact between the paw and the ground does not occur at a single point, but rather over number of points, thus there are a number of forces acting on the underside of the paw at any given instant during stance. At each instant during the stance phase the forces which act between the paw and the surface can be summed to find a resultant GRF vector. The location on the paw at which this single GRF vector is applied is known as the center of pressure. The center of pressure is often used in gait analysis studies [Bobbert et al. (1992); Fowler et al. (1993); Huber and Dutoit (2004); Wu and Hitt (2004)], and is an important consideration for the development of ground contact models for both forward dynamics simulations and robotics [Bruneau and Ouezdou (1999)]. There are two relatively common methods which are used to measure the center of pressure which will be discussed.

The first method involves using a grid of small force plates (or pressure sensors) instead of a single force plate. As the subject walks across the grid the forces (or pressure) applied to each part of the grid can be measured individually. The force distribution along the foot can then be summed for each discrete time step for which the data was collected, and then analyzed to find the center of pressure.

The second method involves the measurement of both the moments which are applied to the force plate and the location of the paw on the force plate, in addition to measuring the forces in the vertical and horizontal directions. Using the location of the foot on the force plate and the measured forces and moments applied to the force plate, the center of pressure for each discrete time step can be determined.

Both of the aforementioned techniques used to obtain the center of pressure information could not used for this study. A single force plate was used to measure the GRF's, thereby ruling out the first method. Neither the moments acting on the force plate, nor the location of the paw on the force plate were recorded which then ruled out the second method. Therefore no center of pressure information was available for this study.

Chapter 3

Two-Dimensional Inverse Dynamics Model

When a system of rigid bodies is subject to a motion, the internal forces and moments which act upon the connections of the system during the motion are often desired. If the motion, the physical properties of the bodies, and the external forces which act upon the system are known, then the internal forces and moments can be calculated. The process of calculating the internal moments and forces is known as inverse dynamics and is often used in gait analysis studies. The direct measurement of the torques and the reaction forces which occur within the limbs is generally not a feasible option for most investigations. The cost, the time required, or the invasive nature of the techniques used to directly measure the moments and forces in a limb frequently prevent the implementation of direct measurement technique.

The application of inverse dynamics to the study of animal locomotion is performed by creating models with which to simulate the motion. The model itself may encompass the whole animal [Herr and McMahon (2000)], or may focus only on a single limb [Manter (1938); Hoy and Zernicke (1985); Fowler et al. (1993)]. Once a suitable model has been created, the locomotion of the animal is studied and the kinematics of the body (or bodies) of interest are determined. Should any external forces act upon the body during the locomotion, the magnitude, direction, and time that the forces occur must be measured as well. After the kinematic and force data are collected, the equations of motion governing the chosen model can then be used to solve for the unknown internal forces and moments. The internal moments and forces could then be related to muscle forces if so required.

This chapter outlines the methodology pertaining to the creation of the two-dimensional hindlimb model used to investigate the joint torques which occur at the hip, knee, and ankle joints for a typical feline hindlimb. The joint torques estimated by the model, and the sensitivity of the estimated joint torques to variations in the segmental parameters of the model, are discussed. The segmental parameters referred to are the centroidal moments of inertia, the masses, and the center of mass locations for each segment of the hindlimb model. The sensitivity analysis of the joint torques to variations in the segmental parameters of the model is included in order to clarify which of the segmental parameters are the most influential with respect to their effect on the estimated joint torques. Should the estimated joint torques prove to be sensitive to any of the segmental parameters, the accuracy of the estimated joint torques could be improved in future works by finding more accurate methods of measuring or obtaining the segmental parameters, if so required. An investigation into the joint torques estimated by the two-dimensional hindlimb model, with and without a rigid paw, is also included.

3.1 Anatomical Modeling

The two-dimensional hindlimb model is based upon the skeletal anatomy of a typical feline hindlimb, as shown in Figure 3.1. Excluding the paw, the feline hindlimb consists of three main segments: the thigh segment between the hip and knee joints, the shank segment between the knee and ankle joints, and the tarsal segment between the ankle and MTP joints.

When creating the two-dimensional hindlimb model, the thigh, shank, and tarsal segments of the hindlimb were modeled as rigid uniform slender rods. The actual geometry and mass distribution of a feline hindlimb is much more complex due to the non-uniform distribution of soft tissues along the limb, however the validity of the uniform slender rod assumption will be addressed in a subsequent analysis (see Section 3.5.4). Modeling the paw for the two-dimensional hindlimb model proved to be much more difficult since the structure of the paw is is quite different when compared to the structure of rest of the hindlimb.

A typical feline hindlimb paw is comprised of four digits, where each digit contains a number of individual phalanges and their associated interphalangeal joints. Due to the much smaller size of the digits and the number of phalangeal bones in each digit, the structure of the paw allows for far more flexibility

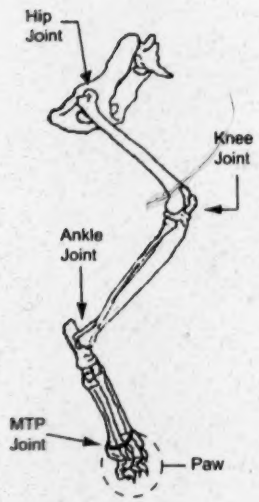

Figure 3.1: Typical feline hindlimb skeletal anatomy. The paw, which consists of the individual phalanges bones and the interphalangeal joints, is shown inside the broken circle.

when compared to the rigidity of the rest of the hindlimb segments. Kuhtz-Buschbeck et al. (1994) performed an X-ray study of the feline hindlimb for typical cats walking on a treadmill. Figure 1 from Kuhtz-Buschbeck et al. (1994) shows a sequence of X-ray frames taken during the transition between the swing and stance phase for a feline hindlimb. During the latter portion of the swing phase the digits of the paw extend and spread out in preparation for contact with the ground. Upon initiation of the stance phase the digits then contract, pulling in closer to the rest of the paw, providing a more solid base of support. Figure 4 from Kuhtz-Buschbeck et al. (1994) shows the transition between stance to swing phase. Here the MTP joint gradually lifts off of the ground and at the very end of the stance phase the hindlimb touches the ground with the tips of the digits. Along with the movement of the phalanges, there is also some small amount of deformation which occurs during ground contact due to the compliance of the soft tissues in the paw. These soft tissues include a plantar pad and four digital paw pads which are located on the underside of the paw. The events that have just been discussed for the contact between the paw and a surface are depicted in Figure 3.2.

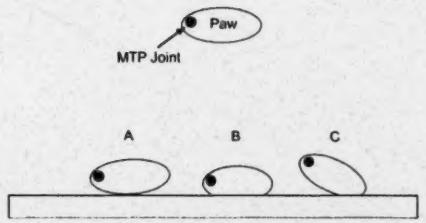

Figure 3.2: Depiction of the paw: A) Immediately prior to contact with the ground. B) Just after initial contact with the ground. C) Near the end of the stance phase. The direction of locomotion is from left to right.

The trajectory of the MTP joint, obtained from the two-dimensional kinematic data during the stance phase, is shown in Figure 3.3. When the paw initially comes into contact with the surface the MTP joint is located at a height of 1.6 cm above the ground and at an X coordinate location of 16.0 cm. Midway through the stance phase the MTP joint descends to the minimum of height 0.95 cm while travelling forward to a X coordinate location of 17.6 cm. At lift off the MTP joint is located at a height of 2.7 cm and a X coordinate location of 19.2 cm. The distance travelled by the MTP joint in both the X and Z directions during the second half of the stance phase is larger than the distance travelled during the first half of the stance phase due to the rotation of the paw about its area of contact, as shown by event C in Figure 3.2.

Due to the compliance of the soft tissues, and the lifting of the rear portion of the paw over the latter portion of the stance phase, the GRF's do not act at a single location on the paw over the duration of the stance phase. Fowler et al. (1993) measured the changes in the center of pressure for the hindlimb paws of three separate cats walking along a level surface. The results of 26 trials showed that from the point of initial contact to the end of the stance phase, the center of pressure moved a mean distance of 1.2 cm, with a standard deviation of 0.7 cm, in the same direction in which the cat was walking.

Perhaps the most straight forward approach to implementing the paw into the two-dimensional hindlimb model for an inverse dynamics investigation would be to treat the paw as a single rigid body and use the center of pressure information to apply the GRF's at the appropriate locations on the paw. This approach was taken by both Fowler et al. (1993) and Perell et al. (1993). This approach does not portray the actual dynamics of the paw in the sense that it

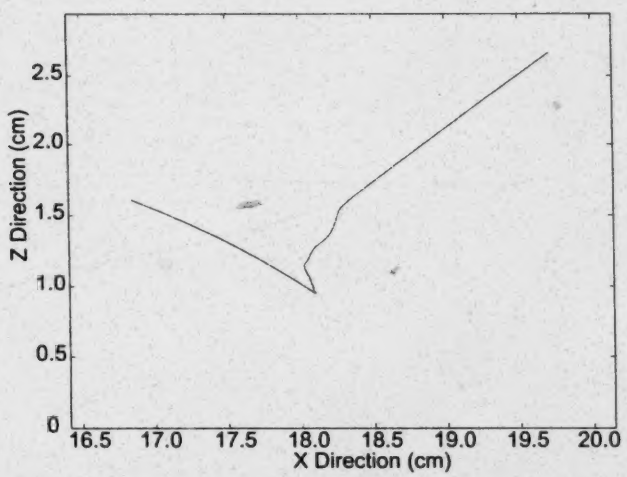

Figure 3.3: Trajectory of the MTP joint during the stance phase (0.23 s to 0.92 s).

ignores the reaction forces and moments which occur within the paw itself. To create a inverse dynamics model of the paw to investigate the reaction forces and moments that occur internal to the paw would require kinematic data for the phalanges. As mentioned in Section 2.1.1 it is difficult to acquire the required kinematic data with a video based motion capture system, due to the physical size of the phalanges. Additionally the precise location to which the GRF's would be applied to the phalanges would be quite difficult to ascertain since the GRF's are transmitted to the phalanges through the soft tissues on the underside of the paw. Thus, an approximation must be made to simplify the modeling process. Here the rigid body paw and the center of pressure information provides such an approximation.

For this study a decision was made to exclude the paw from the two-dimensional hindlimb model because any paw model that might be constructed would require the kinematic data for the motion of the phalanges, as well as the center of pressure information, both of which were not available. The MTP joint was chosen as the end of the two-dimensional hindlimb model. Unfortunately by excluding the paw from the hindlimb model the joint torques estimated by the hindlimb model may not accurately portray the joint torques which actually occur within the feline hindlimb. An investigation into the effects on the estimated joint torques due to the inclusion of a rigid body paw is included in Section 3.6.

While the chosen two-dimensional hindlimb model may not provide an accurate portrayal of the joint torques which occur in the feline hindlimb, it can provide an approximation of what the joint torques may look like, and can be used to investigate how the joint torques are affected by variations in the segmental properties of the hindlimb.

3.2 Hindlimb Model

Mabuchi and Fujie (1996) measured the dynamic friction coefficients for the stifle (knee) joints of mature Japanese white rabbits and found the dynamic friction coefficient to have a mean value of 0.008 with a standard deviation of ± 0.002. They compared their findings to those of an earlier study for an intact canine hip in which the dynamic coefficient of friction for the hip joint was found to be 0.007 with a standard deviation of ± 0.004. These findings show that while there is a small amount of friction between limb joints, the amount of friction that exists is very small. Since the contribution of friction to the joint torques should be negligible when compared to the total magnitude of the joint torques, the hip, knee, and ankle joints of the hindlimb model were modeled as frictionless revolute joints.

With the exclusion of the paw the two-dimensional hindlimb was modeled as a three-link, three-degree of freedom, rigid body system, as shown in Figure 3.4. It was assumed that the relatively constant motion of the hip in the sagittal plane (see Figure 2.3) would not be large enough to cause any significant effects in the estimated joint torques. Thus, the position of the hip was held at a stationary location for the two-dimensional hindlimb model. The orientation of each limb segment of the two-dimensional hindlimb model is specified by a single joint angle associated with each individual segment. Θ_1, Θ_2, and Θ_3 are used to specify the orientation of the thigh, shank and tarsal segments respectively, as shown in Figure 3.4. The two-dimensional hindlimb model shown in Figure 3.4 is oriented such that all of the joint angles are positive.

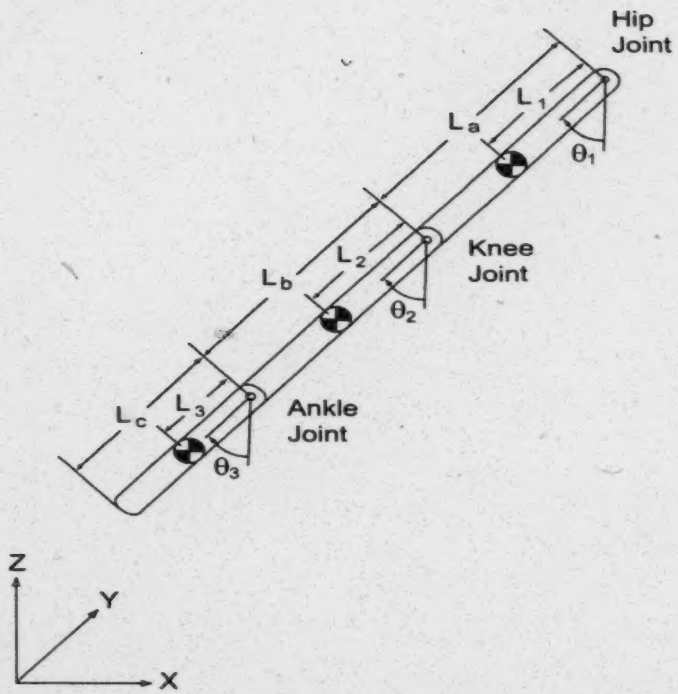

Figure 3.4: Two-Dimensional hindlimb model for a typical feline hindlimb. Note that the model is not shown to scale.

The free body diagrams for each of the limb segments of the two-dimensional model is shown in Figure 3.5. Both ground reaction forces, GRFx and GRFz, are applied to the end of the tarsals (which corresponds to the location of the MTP joint for the actual feline hindlimb). Both GRF's are defined as being positive when the directions in which they act are aligned with the positive axes of the global reference frame. The moments T_{hip}, T_{knee}, and T_{ankle}, shown in Figure 3.5 are referred to as the joint torques. The hindlimb model was defined such that each joint torque corresponds to a specific limb segment. For example a positive hip torque implies that a clockwise torque would act upon the thigh at the hip joint. Similarly a positive knee torque implies that the shank would experience a clockwise torque, while a torque of equal magnitude would act in the opposite direction upon the thigh segment as shown in Figure 3.6

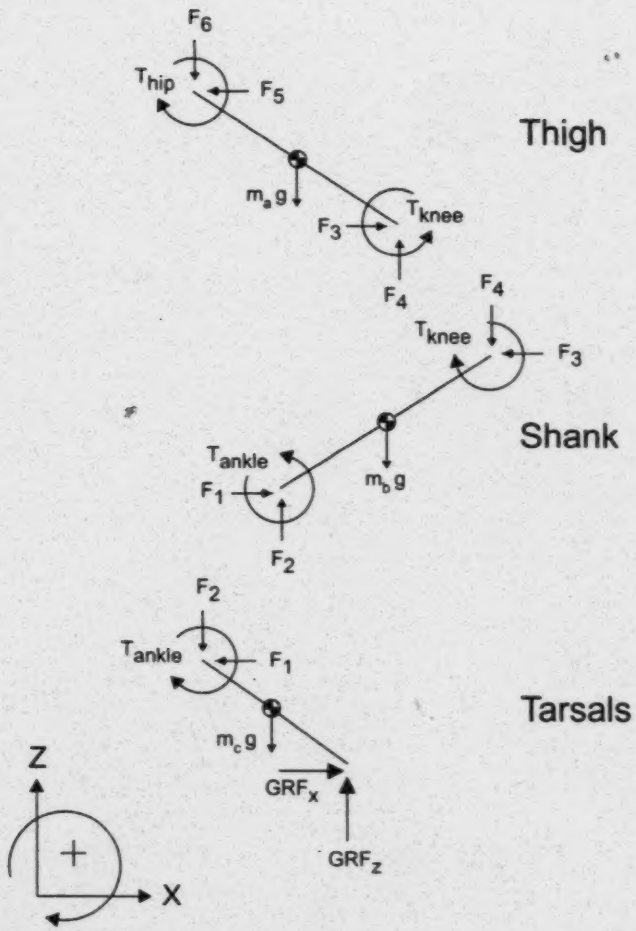

Figure 3.5: Free body diagram for the two-dimensional model. T_{hip}, T_{knee}, and T_{ankle} are the joint torques. $F_1, F_2, ..., F_6$ are the reaction forces which occur between the rigid bodies.

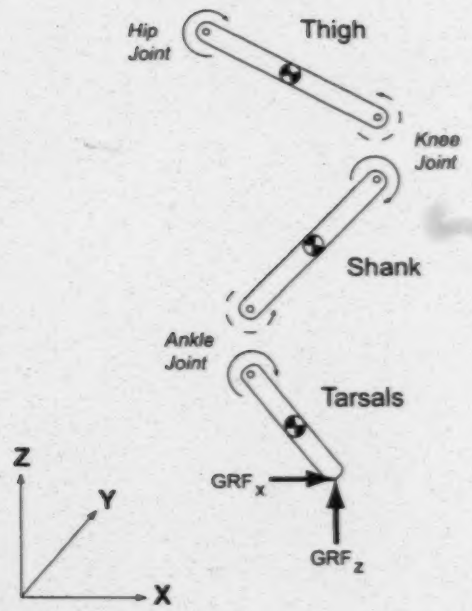

Figure 3.6: Definition of joint torques. Positive (negative) joint torques are shown with solid (dashed) circular arrows.

The length of the limb segments could not be found directly from the kinematic data due to the movement of the markers affixed to the skin of the hindlimb. In order to compensate for the variation in the lengths observed in the kinematic data, the mean length of each limb segment was calculated from the kinematic data and used as the actual limb segment length, as discussed in Chapter 2, Section 2.1.1.

Hoy and Zernicke (1985) measured the segmental limb parameters of nine individual cats and presented empirical equations with which the individual segmental masses and the moment of inertia about the center of mass, for a cat's limb segments, can be predicted. Table 1 in Hoy and Zernicke (1985) also listed the individual segment masses as a percentage of the total cat mass, the center of mass location as a percentage of the segment length, and the moment of inertia of each segment as measured from nine separate cats. As mentioned in Section 2.1.1 the length of each hindlimb segment was estimated from the positional data. The mass of the cat for which the two-dimensional kinematic

and GRF data was collected was not provided. Since a total cat mass was required in order to use the empirical equations presented by Hoy and Zernicke (1985) to predict the segmental masses for the hindlimb model, a mass of 4.0 kg for the cat was assumed.

While the masses for the hindlimb segments were predicted using the empirical equations presented by Hoy and Zernicke (1985), the center of mass locations (L_1, L_2, and L_3), and the centroidal moments of inertia, or CMI's, (I_a, I_b, and I_c) for the two-dimensional hindlimb model were calculated based on the hindlimb segments being modeled as uniform slender rods. If the values predicted by Hoy and Zernicke (1985) had been used for the center of mass locations and CMI's, the variation of the segmental parameters of each hindlimb segment for the sensitivity analysis would have been made quite difficult. The moment of inertia of each hindlimb segment is dependant on the mass, the center of mass location, and the geometry of each hindlimb segment. Since Hoy and Zernicke (1985) did not provide any geometries with which to model each segment of the hindlimb, the change in the moment of inertia for each hindlimb segment could not be calculated when the mass or location of the center of mass for each hindlimb segment was varied. By modeling the hindlimb segments as uniform slender rods this problem is avoided, allowing for the variation of each of the segmental parameters of the two-dimensional hindlimb model.

Not surprisingly the values for the segmental centers of mass and CMI's predicted by Hoy and Zernicke (1985) conflict with the uniform slender rod assumption, since the slender rods do not account for the more complex geometry of a feline hindlimb. Table 3.1 shows the values for the CMI's of each limb segment, as predicted the empirical equations of Hoy and Zernicke (1985), along with those values used for the model based upon the homogenous solid slender rod assumption. Also included in Table 3.1 are measured center of mass locations for each of the hindlimb segments [Hoy and Zernicke (1985)], and the center of mass locations used based on the slender rod assumption. The location of the mass center for each segment is defined as a percentage of the segment length, as measured from the proximal joint of the segment. The proximal joint is defined as being the joint which is nearest the point of attachment or origin. Thus for the thigh, shank, and tarsal segments the hip joint, the knee joint, and the ankle joint are the respective proximal joints. Of the three hindlimb segments the center of mass location of the shank, which is 42.3% of the length of the shank segment as measured from the knee joint, is the furthest from the center of mass locations based upon the homogenous

slender rod geometry. The suitability of the choice of slender rods for modeling the hindlimb segments will be addressed in the sensitivity analysis of the segmental limb parameters. All of the segmental parameters and their values, for the limb segments of the two-dimensional hindlimb model, are shown in Table 3.2.

Table 3.1: Centroidal moments of inertia and center of mass locations from Hoy and Zernicke (1985) and the uniform slender rod assumption.

Limb Segment	Predicted CMI ($kg{\cdot}m^2$)	Slender Rod CMI ($kg{\cdot}m^2$)	Measured Center of Mass (%)†	Slender Rod Center of Mass (%)
Thigh	2.171×10^{-4}	1.204×10^{-4}	44.3 (6.33)*	50.0
Shank	1.031×10^{-4}	0.667×10^{-4}	42.3 (2.39)	50.0
Tarsals	0.093×10^{-4}	0.076×10^{-4}	48.6 (6.04)	50.0

CMI = Centroidal Moment of Inertia.
† Percent of segment length from proximal joint.
* Mean (standard deviation)

Table 3.2: Table of two-dimensional hindlimb model segment parameters.

Segment Parameter	Description	Value	Units
I_a	CMI of the thigh	1.204×10^{-4}	$kg{\cdot}m^2$
I_b	CMI of the shank	0.667×10^{-4}	$kg{\cdot}m^2$
I_c	CMI of the tarsals	0.076×10^{-4}	$kg{\cdot}m^2$
M_a	Mass of limb the thigh	204	g
M_b	Mass of the shank	57	g
M_c	Mass of the tarsals	23	g
L_a	Length of limb the thigh	8.48	cm
L_b	Length of the shank	9.11	cm
L_c	Length of the tarsals	5.83	cm
L_1	Center of mass location	$L_a/2$	cm
L_2	Center of mass location	$L_b/2$	cm
L_3	Center of mass location	$L_c/2$	cm

3.3 Kane's Equations

Kane and Levinson (1988) outline a method of formulating dynamical equations of motion, which are often referred to as Kane's equations of motion. Kane's method has a number of advantages over other methods formulating equations of motion, such as Newton's method or Lagrange's method. In general the equations of motion obtained from Kane's method are less complex when compared to the equations of motion obtained from either Newton's or Lagrange's method. Kane's method automatically eliminates non-contributing forces and moments without requiring the use of algebraic means, as is the case when employing Newton's equations of motion, which simplifies the equations of motion. Additionally Kane's method is operationally straightforward and the dynamic equations provided are computationally efficient, thus suited to both forward and inverse dynamics simulations.

Once the segmental parameters for the two-dimensional hindlimb model were defined, Autolev was used to find Kane's dynamical equations of motion for the model. Autolev is a symbolic manipulator that automatically derives Kane's dynamical equations of motion. The Autolev code used to generate Kane's equations of motion can be found in Appendix B. Kane's equations of motion for the two dimensional inverse dynamics model are:

$$\begin{aligned} T_{hip} &= T_{knee} + L_a(GRF_x\cos\Theta_1 - GRF_z\sin\Theta_1) + g\sin\Theta_1(L_1M_a + L_aM_b + L_aM_c) \\ &\quad + L_a(L_2M_b + L_bM_c)\sin(\Theta_1-\Theta_2)\dot{\Theta}_2^2 + L_3L_aM_c\sin(\Theta_1-\Theta_3)\dot{\Theta}_3^2 \\ &\quad + (I_a + M_aL_1^2 + M_bL_a^2 + M_cL_a^2)\ddot{\Theta}_1 + L_a(L_2M_b + L_bM_c)\cos(\Theta_1-\Theta_2)\ddot{\Theta}_2 \\ &\quad + L_3L_aM_c\cos(\Theta_1-\Theta_3)\ddot{\Theta}_3 \end{aligned} \tag{3.1}$$

$$\begin{aligned} T_{knee} &= T_{ankle} + L_b(GRF_x\cos\Theta_2 - GRF_z\sin\Theta_2) + g\sin\Theta_2(L_2M_b + L_bM_c) \\ &\quad - L_a(L_2M_b + L_bM_c)\sin(\Theta_1-\Theta_2)\dot{\Theta}_1^2 + L_3L_bM_c\sin(\Theta_2-\Theta_3)\dot{\Theta}_3^2 \\ &\quad + L_a(L_2M_b + L_bM_c)\cos(\Theta_1-\Theta_2)\ddot{\Theta}_1 + (I_b + M_bL_2^2 + M_cL_b^2)\ddot{\Theta}_2 \\ &\quad + L_3L_bM_c\cos(\Theta_2-\Theta_3)\ddot{\Theta}_3 \end{aligned} \tag{3.2}$$

$$\begin{aligned} T_{ankle} &= +L_c(GRF_x\cos\Theta_3 - GRF_z\sin\Theta_3) - L_3L_aM_c\sin(\Theta_1-\Theta_3)\dot{\Theta}_1^2 \\ &\quad - L_3L_bM_c\sin(\Theta_2-\Theta_3)\dot{\Theta}_2^2 + gL_3M_c\sin\Theta_3 + (I_c + M_cL_3^2)\ddot{\Theta}_3 \\ &\quad + L_3L_bM_c\cos(\Theta_2-\Theta_3)\ddot{\Theta}_2 + L_3L_aM_c\cos(\Theta_1-\Theta_3)\ddot{\Theta}_1 \end{aligned} \tag{3.3}$$

After Kane's equations were generated using Autolev, they were implemented into a MATLAB® program created to determine the three joint torques when given the kinematic and GRF data as the inputs. Newton's equations of motion for the two-dimensional inverse dynamics model were also derived and implemented into a MATLAB® program so that they could be used to solve for the three joint torques in a similar fashion. The joint torques calculated from Newton's equations of motion were then used as a check on those found from Kane's equations.

3.4 Two-Dimensional Joint Torques

When discussing joint torques the terms flexor and extensor are often used. A flexor torque refers to any torque which flexes the limb, bringing the limb closer to the body, while an extensor torque is just the opposite of a flexor torque, as it extends the leg away from the body. For the hip and ankle joints an extensor torque represents a positive torque, while a flexor torque represents a negative torque. The knee joint on the other hand is just the opposite. A flexor knee torque represents a positive torque, while an extensor knee torque represents a negative torque.

The estimated joint torques calculated using the two-dimensional hindlimb model are shown in Figure 3.7. The two vertical lines which run through the figure indicate the transitions between the swing and stance gait phases. The first transition occurs at 0.23 s when the paw comes into contact with the ground, as the limb exits the first swing phase and enters the stance phase. The stance phase continues until 0.92 s at which point the paw loses contact with the surface, and the limb enters into a second swing phase. Figure 3.8 has been included to aid in the discussion of the joint torques by providing a visual representation of some of the positions of the hindlimb during the swing and stance phases.

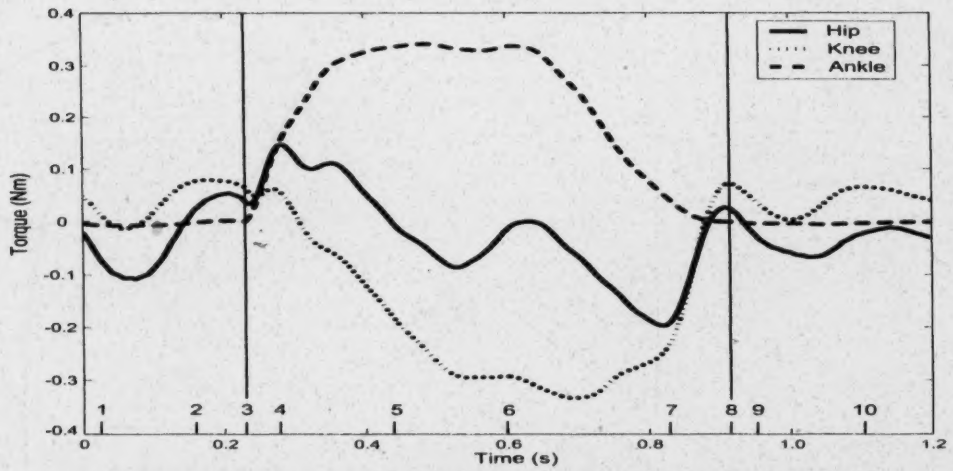

Figure 3.7: Joint torques estimated from the two-dimensional inverse dynamics hindlimb model. The two vertical lines indicate the transitions between the swing and stance gait phases, while the small vertical bars, numbered $1 - 10$, represent the times for each limb position shown in Figure 3.8

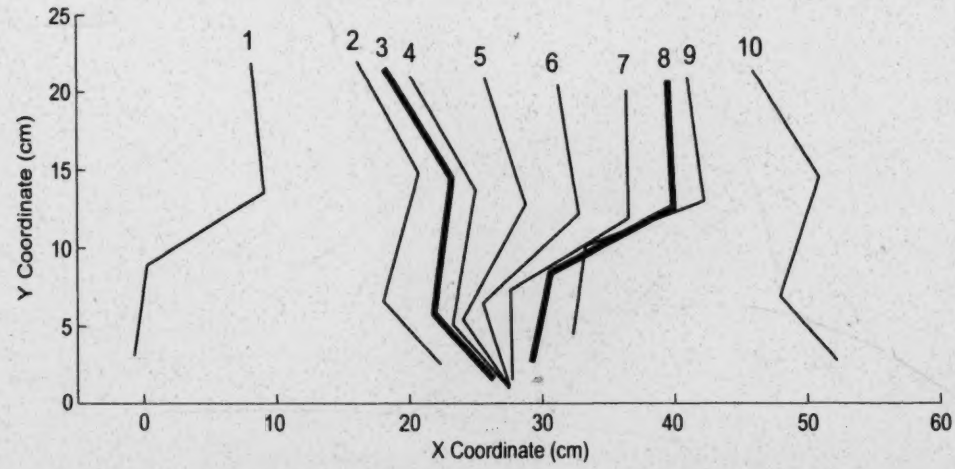

Figure 3.8: Selected hindlimb positions corresponding to Figure 3.7. Positions 3 and 8 have been darkened as they show the beginning and end of the stance phase.

During the swing phases the estimated joint torques are much smaller in comparison to the joint torques which occur during the stance phase. An explanation for the difference in the size of the estimated joint torques can be found if one considers the forces which act upon the hindlimb during the swing and stance phases. The only forces which act upon the hindlimb that contribute to the joint torques during the swing phases are the gravitational forces acting on each hindlimb segment, and the forces which arise due to the inertia of each of the hindlimb segments. The masses of each limb segment, which are large contributors to the magnitude of the inertial and gravitational forces, are relatively small and thus the joint torques which occur during the swing phases are also small. During the stance phase the hindlimb must support a portion of the bodyweight of the cat, which is much larger than the individual masses of the hindlimb segments, and aid in locomotion by providing propulsion in addition to the inertial and gravitational forces. Therefore much larger forces can be expected during the stance phase.

During the initial portion of the first swing phase (position 1) all three joint torques act as flexors, where the hip torque swings the leg forward, while the knee and ankle torques lift the shank and tarsals clear of the ground. During the latter part of the first swing phase (position 2) both the hip and ankle torques become positive as the hip torque acts as a extensor torque to slow the forward progression of the leg, and the ankle torque begins extending the tarsals in preparation for the stance phase. The knee torque remains a flexor torque throughout the latter part of the swing phase, keeping the shank from extending, and maintaining the orientation of the lower limb.

At the onset of the stance phase (positions 3−5) the knee and ankle torques undergo a marked change in magnitude as the hindlimb must now support a portion of the cat's bodyweight. Both the knee and ankle torques act as extensor torques in order to keep the leg from collapsing. The hip torque, however, does not see the same change in magnitude as the knee or ankle torques. At the onset of the stance phase the magnitude of the hip torque increases as it helps to propel the cat forward, then for the majority of the stance phase (positions 5 − 8) the hip torque decreases and becomes a flexor torque (a negative hip torque) in order to prevent the hip from dropping while the other hindlimb swings forward. During the latter stage of the stance phase (positions 7 and 8) all three joint torques undergo a rapid decrease in magnitude as the other hindlimb comes into contact with the ground. This allows the hindlimb being studied to unload and prepare for the next swing phase.

The initial portion of the second swing phase is quite similar to that of the first swing phase, but the latter portion of the second swing phase does differ from the first swing phase. During the latter portion of the second swing phase (position 10) the hip torque does not reach the same negative magnitude as in the first swing phase, nor does it change signs to become positive, switching from a flexor to an extensor torque. This could be explained by the decrease in speed of the limb over the second swing phase, which can be seen in Figure 2.6. Many factors could contribute to this reduction in speed of the limb, though the most likely would be that the cat slowed its forward progression speed.

3.4.1 Static and Dynamic Contributions to the Estimated Joint Torques

The static and dynamic contributions to the estimated joint torques can be separated from one another. If all dynamic terms in the equations of motion, such as $\dot{\Theta}_1$, $\dot{\Theta}_2$, $\dot{\Theta}_3$, $\ddot{\Theta}_1$, $\ddot{\Theta}_2$, and $\ddot{\Theta}_3$, are set equal to zero the static contributions to the estimated joint torques can be brought to light. These will be referred to as the static joint torques. The static joint torques can then be subtracted from the original joint torques to obtain the dynamic contributions to the estimated joint torques, or dynamic joint torques. The static joint torques are shown in Figure 3.9. As can be observed in Figure 3.9 the static joint torques are a contributor to the joint torques in the swing phases and a major contributor to the stance phase. This is not surprising during the stance phase when considering the relatively slow motion of the hindlimb, when compared to the swing phase, and the application of the GRF's.

Figure 3.10 shows the dynamic joint torques. While the dynamic joint torques do play a significant role during the swing phase, they are almost negligible when compared to the magnitude of the static joint torques between 0.35 s and 0.8 s. Should the speed of locomotion increase, the contribution of the dynamic joint torques should remain very small in comparison to the static joint torques throughout the majority of the stance phase. While the duration of the stance phase will decrease as the locomotion speed increases (Goslow et al. (1973)), and thus the speed at which the hindlimb moves increases, larger GRF's can be expected as well thereby increasing the magnitudes of the static joint torques.

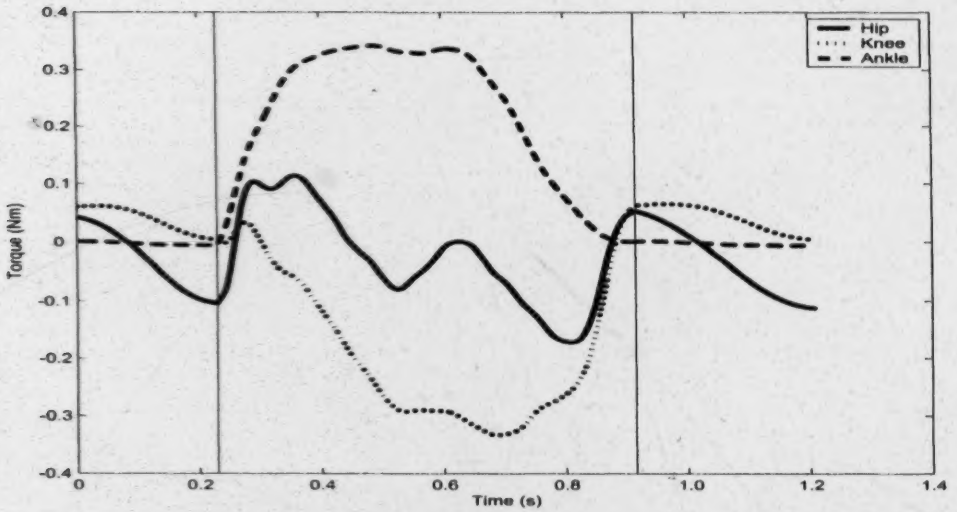

Figure 3.9: Static contributions to the estimated joint torques.

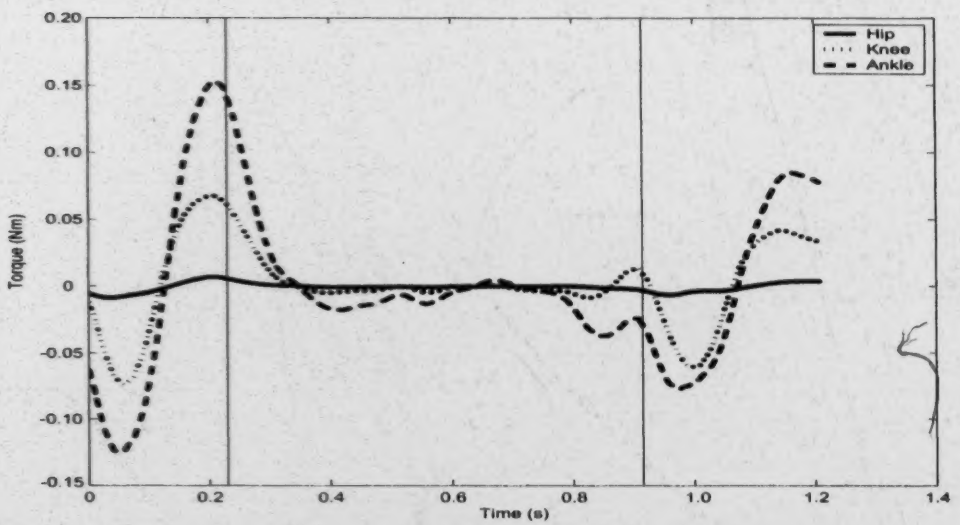

Figure 3.10: Dynamic contributions to the estimated joint torques.

Researchers sometimes ignore the contributions of the dynamic joint torques altogether during the stance phase (Fowler et al. (1993); Perell et al. (1993); Shen and Poppele (1995); Trank and Smith (1996)), however care should be taken to not rule out the effects of the dynamic joint torques during the transitions between the swing and stance phases. As shown in Figure 3.10 the peak magnitudes of the dynamic joint torques occur during the transition from the swing phase to the stance phase. Depending on the speed of locomotion being studied the contributions of the dynamic torques may become significant during these transitions between swing and stance.

3.4.2 Fixed Hip Assumption

An assumption that was made when defining the two-dimensional hindlimb model was that the hip could remain at a stationary location. In reality, however, the hip joint moves. The two-dimensional hindlimb model was modified such that the motion of the hip could be included, allowing the effect of the hip motion on the estimated joint torques to be investigated. The hip positions, velocities, and accelerations were calculated from the positional data similarly to the angular kinematic data. Figures 3.11, 3.12, and 3.13 show the joint torques calculated when the hip joint is held at a fixed location (solid lines) and when the hip joint of the model follows the actual hip motion (plotted with dots). The only differences observed in the three joint torques occurred in the hip joint torque, the majority of which occur during the swing phases. Since there was no available data on the three-dimensional motion of the hip, for use in the three-dimensional hindlimb model, the fixed hip position was used for both the two-dimensional and three-dimensional hindlimb models to maintain a level of consistency among them. Thus, results obtained with the hip motion included in the model will vary slightly from the results determined in this study.

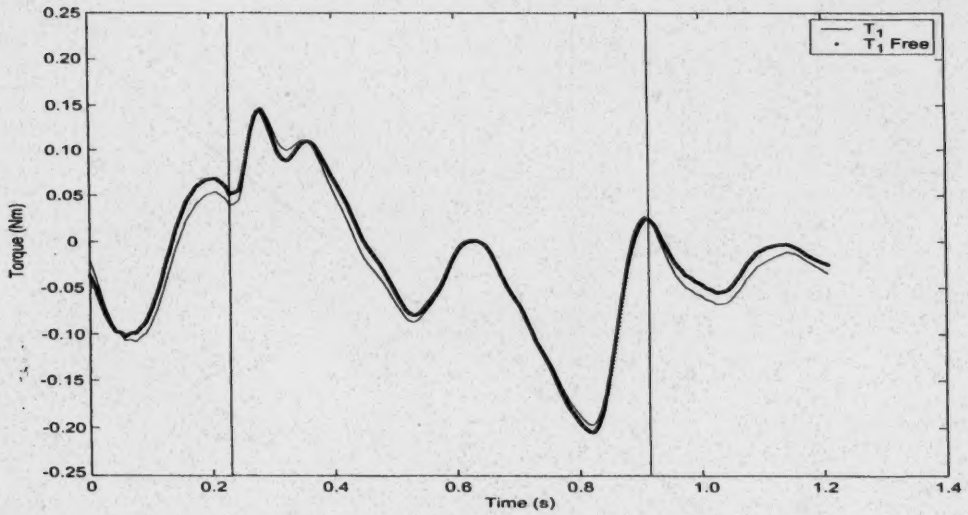

Figure 3.11: Hip joint torques estimated with the hip fixed and with the hip free to follow the actual hip motion.

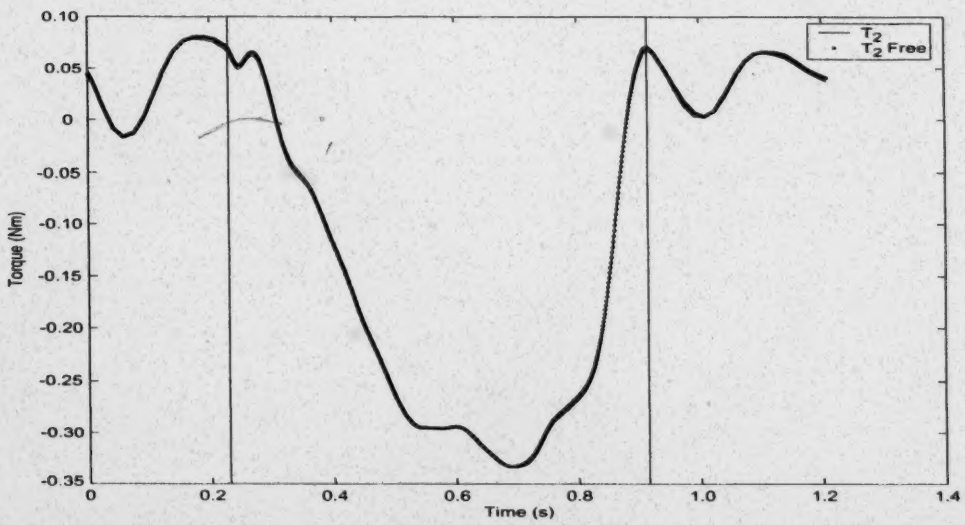

Figure 3.12: Knee joint torques estimated with the hip fixed and with the hip free to follow the actual hip motion.

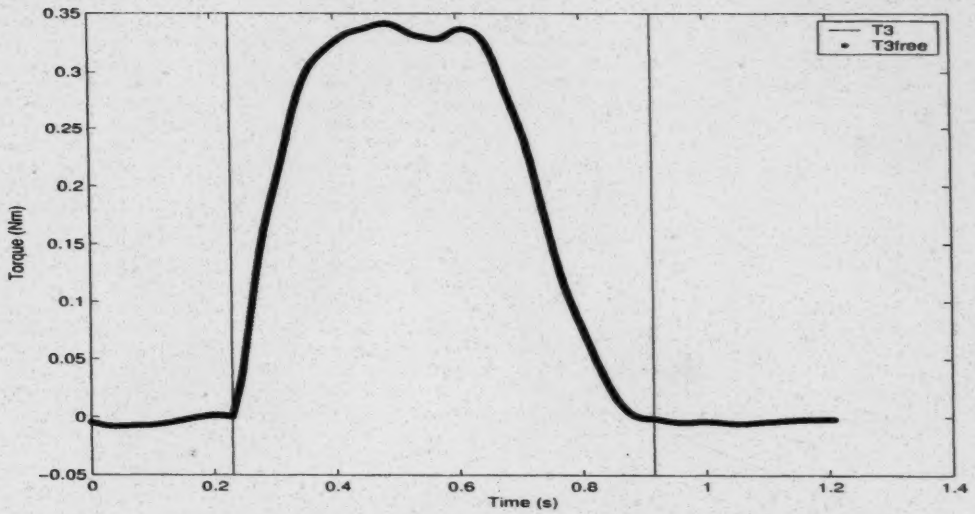

Figure 3.13: Ankle joint torques estimated with the hip fixed and with the hip free to follow the actual hip motion.

3.5 Joint Torque Sensitivity to Variations in Segment Parameters

The sensitivity of the joint torques to changes in each of I_a, I_b, I_c, M_a, M_b, M_c, L_1, L_2, and L_3, were investigated in order to determine the influence each segmental parameter has on the estimated joint torques. All nine of the previously mentioned limb segment parameters were individually varied in 10% increments, from -50% to $+50\%$ of the their nominal values. Using the mass of the thigh (M_a) as an example, the minimum and maximum values used for the variations would be 50% and 150% of the nominal value of M_a, as listed in Table 3.2. Using the same kinematic and GRF data, the resulting joint torques were calculated from the two-dimensional hindlimb model for each variation of the segmental parameters. Since all of the maximum deviations observed occurred for the $\pm 50\%$ variations in each of the segmental parameters, the discussion will focus on the $\pm 50\%$ variations. The maximum deviations observed in the hip, knee, and ankle torques, as percentages of the magnitude of the peak torque for each joint, are shown in Table 3.4 for each one of the segmental parameters varied.

Table 3.3: Maximum deviations observed in the estimated joint torques during the swing phases, as a percentage of the peak joint torques during each swing phase, due to ±50% variations of the hindlimb segmental parameters.

Segmental Parameter Varied	Maximum Hip Torque Deviations (%)		Maximum Knee Torque Deviations (%)		Maximum Ankle Torque Deviations (%)	
	Swing 1	Swing 2	Swing 1	Swing 2	Swing 1	Swing 2
I_a	2.0	2.5	§	§	§	§
I_b	4.5	6.6	6.2	6.2	§	§
I_c	0.4	0.6	0.6	0.6	5.8	6.9
M_a	16.8	33.7	§	§	§	§
M_b	16.8	18.7	25.5	31.3	§	§
M_c	19.6	15.2	21.4	17.3	48.0	52.2
L_1	17.1	31.0	§	§	§	§
L_2	39.2	45.8	41.3	40.0	§	§
L_3	10.3	13.2	9.0	7.4	66.4	60.2

Swing 1 = 1^{st} Swing Phase
Swing 2 = 2^{nd} Swing Phase
§ = No Change

Table 3.4: Maximum deviations observed in the estimated joint torques during the stance phase, as a percentage of the peak joint torques during the stance phase, due to ±50% variations of the hindlimb segmental parameters.

Segmental Parameter Varied	Maximum Hip Torque Deviations (%)	Maximum Knee Torque Deviations (%)	Maximum Ankle Torque Deviations (%)
I_a	1.0	§	§
I_b	1.4	0.8	§
I_c	0.2	0.1	0.1
M_a	10.7	§	§
M_b	7.7	6.9	§
M_c	8.2	4.1	0.9
L_1	10.3	§	§
L_2	20.2	9.2	§
L_3	3.6	1.2	0.9

§ = No Change

Before beginning it should be noted that only the joint torques of the joints located above the hindlimb segment which had its segmental properties varied, were affected by the variation. This occurs due to the interrelation between the hip, knee, and ankle torques in the equations of motion. The equation of motion used to calculate the hip torque depends on the knee torque, which in turn depends upon the ankle torque. Any changes in the segmental parameters of the tarsals (I_c, M_c, or L_3) will affect the equation of motion used to calculate the ankle torque, causing a change in the ankle torque, and thus the knee and hip torques as well. A change in one of the segmental parameters of the shank (I_b, M_b, or L_2) portion of the hindlimb model will affect the knee torque and the hip torque, however the ankle torque will remain unchanged as the equation of motion used to solve for the ankle torque is not affected by any variation in the properties of the shank.

3.5.1 Effect of Centroidal Moment of Inertia Variations

The first segmental parameters investigated were the CMI's of each hindlimb segment. As shown in Table 3.4, the largest deviation observed in the three joint torques was a 2.5% deviation in the hip torque during the initial swing phase caused by a ±50% variation in the centroidal moment of inertia of the shank (I_b). Figure 3.14 shows the estimated hip torques for the ±50% variations in I_b in addition to the original hip torque based on the uniform slender rod assumption. For comparison purposes each of the three original joint torques estimated from the two-dimensional hindlimb model, which were based upon the uniform slender rod assumption, will be referred to as the control torques. The largest deviations which occur due to the ±50% variations in I_b take place during the swing phases but are difficult to observe in Figure 3.14.

While the deviations in the joint torques caused by variations in I_b were quite small, variations in I_a and I_c had even less of an effect. The variations in I_a caused peak deviations of 1.1% or less in the hip joint torque throughout all three phases of the step cycle. Variations in I_c caused peak deviations of 0.2% or less in each of the three gait phases. The extremely small deviations in the joint torques caused by the variations in I_c can be attributed to the small value of I_c, as it is two orders of magnitude smaller than both I_a and I_b.

A linear relationship exists between the deviations observed in the joint torques and the variations of each of the segmental inertia properties. For example, if the amount that I_b was varied by was reduced by a factor of 5, from 50% to 10%, all of the deviations that occur in the joint torques due to

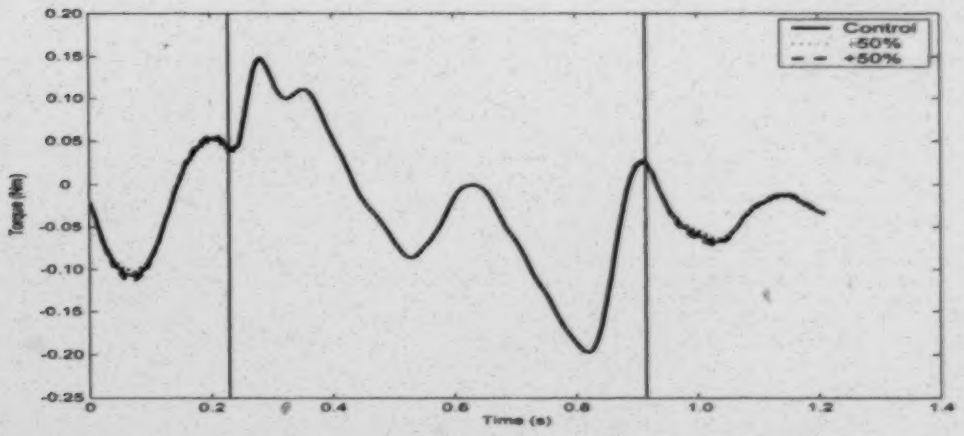

Figure 3.14: Hip joint torques estimated with ±50% variations in I_b.

the variation in I_b would also be reduced by a factor of 5. Therefore the peak deviation of 2.5%, which was observed when the nominal value of I_b was varied by 50%, would decrease to 0.5% if the amount the nominal value of I_b was varied by was decreased to was 10% instead of 50%. The linear relationship between the deviations in the joint torques and the variations in the segmental inertia parameters can be inferred from Equations (3.1), (3.2), and (3.3). Since all of the CMI's (I_a, I_b, and I_c) are first order variables, the deviations in the joint torques are a direct result of the variation in that single parameter.

In addition to the linear relationship between the deviations in the joint torques and the variations in the segmental inertia properties, there is symmetry in the deviations about the control torque caused by both the positive and negative variations in the inertia properties. A positive or negative variation of a fixed magnitude in the value of one of I_a, I_b, or I_c will result in deviations of identical magnitudes, but with opposite signs, about the control torque. Due to this symmetry about the control joint torques, the magnitudes of the peak deviations observed are identical for both positive and negative variations of the same magnitude, in the CMI values.

3.5.2 Effect of Segmental Mass Variations

Figures 3.15 - 3.17 illustrate the deviations which occur in the hip joint torque for the ±50% variations in M_a, M_b, and M_c, respectively. Over the first swing phase the variations in M_a, M_b, and M_c all cause similar deviations in the hip

torque. However, for the second swing phase variations M_a cause the largest deviations in the hip torque. During the stance phase the deviations which were observed are also quite similar in magnitude.

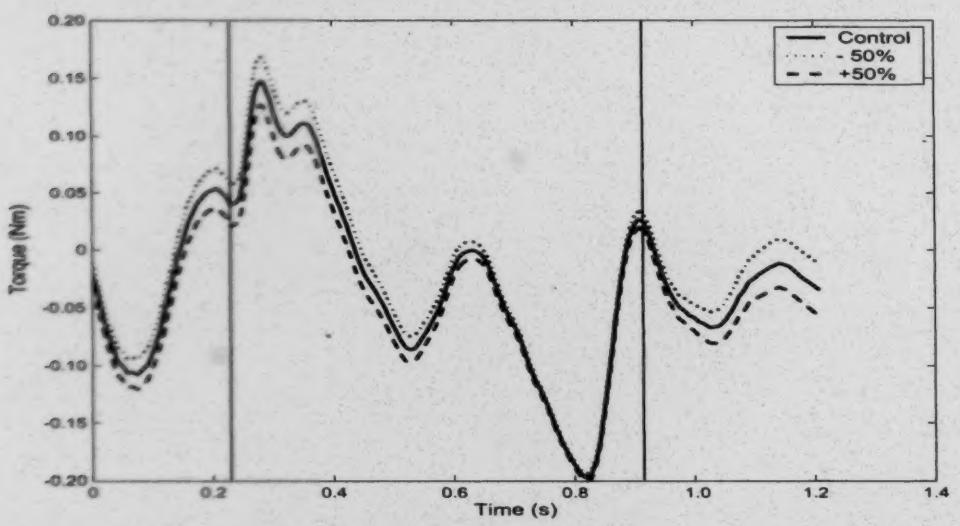

Figure 3.15: Hip joint torques estimated with ±50% variations in M_a.

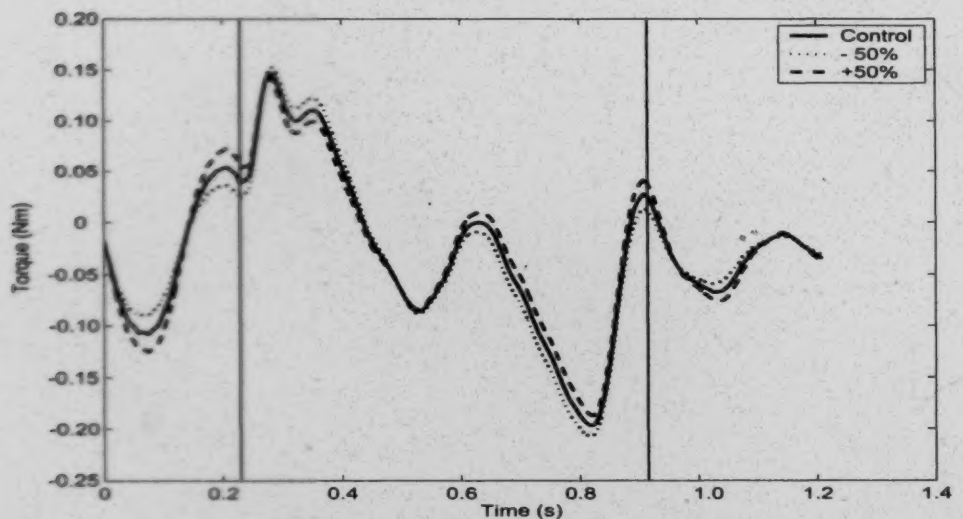

Figure 3.16: Hip joint torques estimated with ±50% variations in M_b.

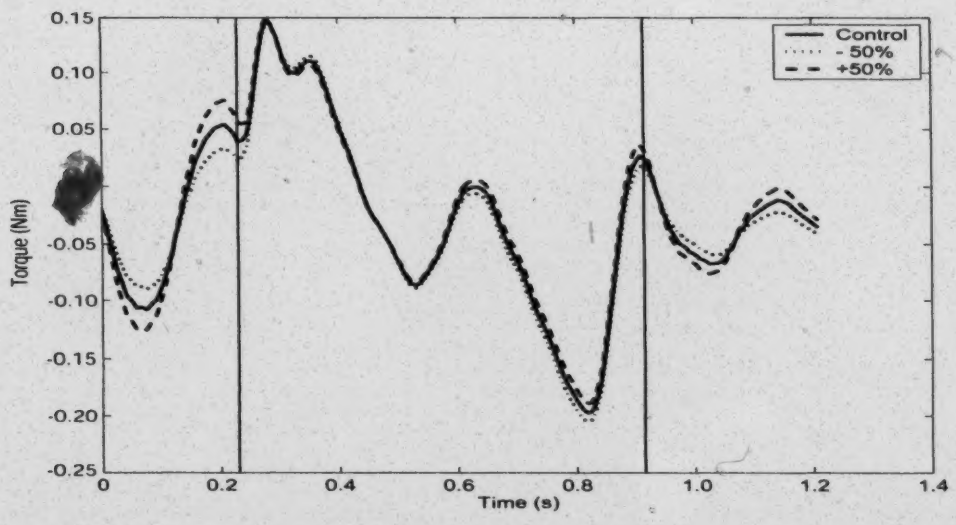

Figure 3.17: Hip joint torques estimated with ±50% variations in M_c.

Figures 3.18 and 3.19 illustrate the deviations which occur in the knee joint torque for the ±50% variations in M_b and M_c. The deviations in both the swing and stance phases, caused by the variations in M_b and M_c, are quite similar in shape and location.

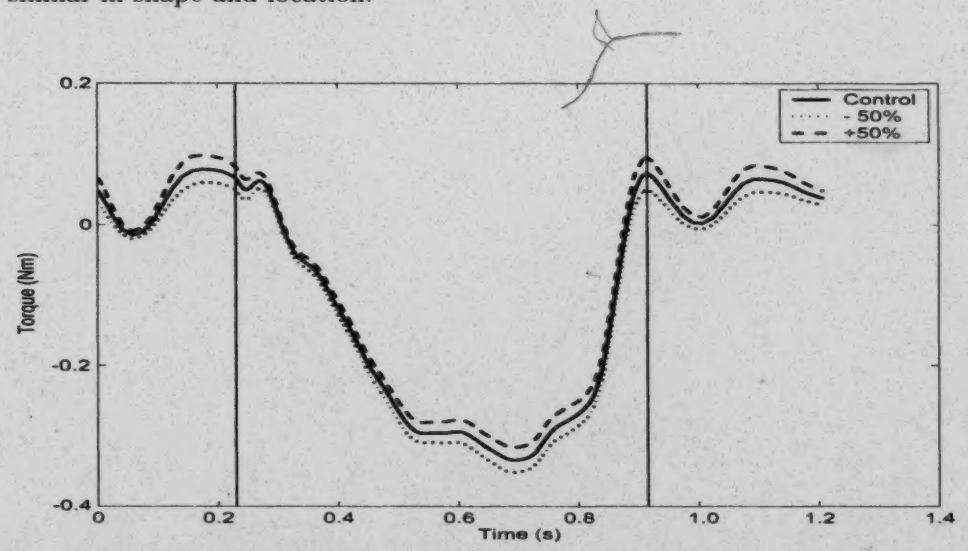

Figure 3.18: Knee joint torques estimated with ±50% variations in M_b.

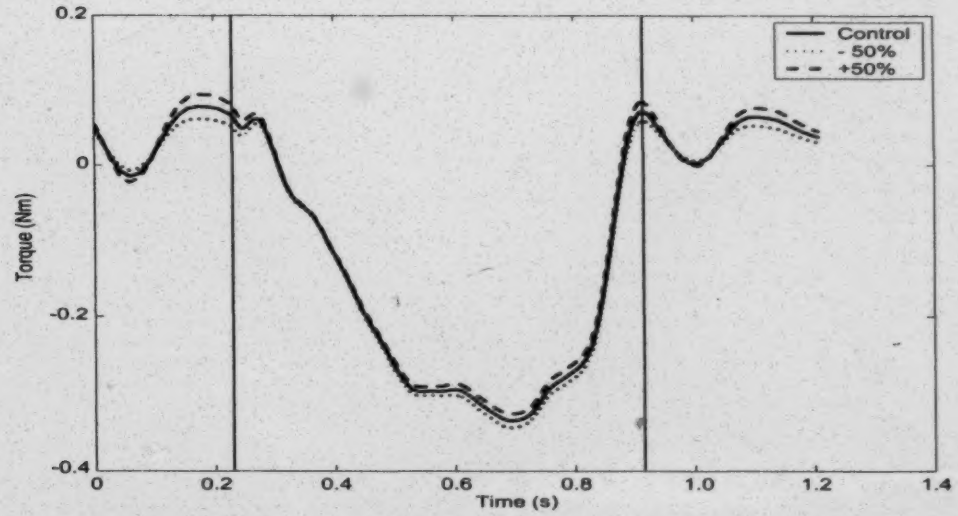

Figure 3.19: Knee joint torques estimated with ±50% variations in M_c.

Figure 3.20 illustrates the deviations which occur in the ankle joint torque for the ±50% variation in M_c. The variations in M_c have a significant effect on the ankle joint torques during the swing phases, however during the stance phase variations in M_c are negligible.

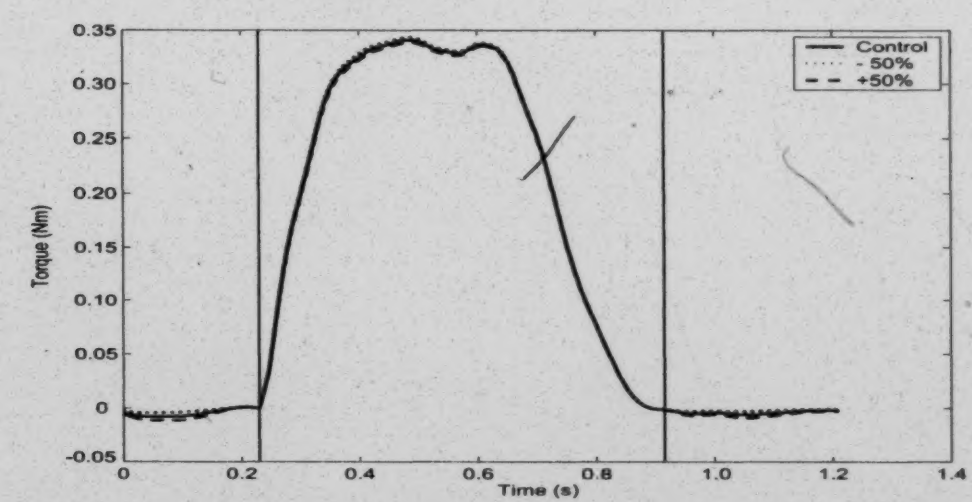

Figure 3.20: Ankle joint torques estimated with ±50% variations in M_c.

Similar to the CMI's there is also a linear relationship between the variations in the masses and the deviations which occur in each of the joint torques, as well as symmetry in the deviations about the control torque. Again these relationships can also be inferred from the Equations 3.1, 3.2, and 3.3, for the same reasons given previously for the CMI terms. Interestingly the variations in relatively small M_c caused deviations in the knee and ankle joint torques, in both the swing and stance phases, that were very close in magnitude to the deviations caused by M_a and M_b.

3.5.3 Effect of Variations in Center of Mass Locations

The sensitivity of the estimated joint torques to the positions of the center of mass of each limb segment were investigated. For the center of mass locations, a positive variation implies that one of L_1, L_2, or L_3 has increased, moving the center of mass down the limb segment, farther away from the body. Alternately a negative variation implies that one of L_1, L_2, or L_3 has decreased, moving the center of mass upwards along the limb, towards the body.

Figures 3.21 to 3.26 show the deviations which occur in the hip, knee, and ankle torques for $\pm 50\%$ variations in each of L_1, L_2, and L_3. During the stance phase the $+50\%$ variation L_2, the location of the center of mass for the shank segment, caused the largest deviations in the estimated joint torques. The $+50\%$ variation in L_2 caused a deviation in the hip joint torque that was twice as large as the deviation caused by the $+50\%$ variation in L_1, where the mass of the thigh was ≈ 4 times larger than the mass of the shank segment. The variations in L_3 had a modest effect on all three joint torques when compared the deviations caused by L_1 and L_2 during the stance phase. This may be attributed to the smaller length and much smaller mass of the tarsal segment of the hindlimb when compared to the thigh and shank segments.

During the swing phases L_2 also caused the largest deviations in the estimated joint torques, while the variation in L_3 had a much more significant effect on all three estimated joint torques during the swing phases.

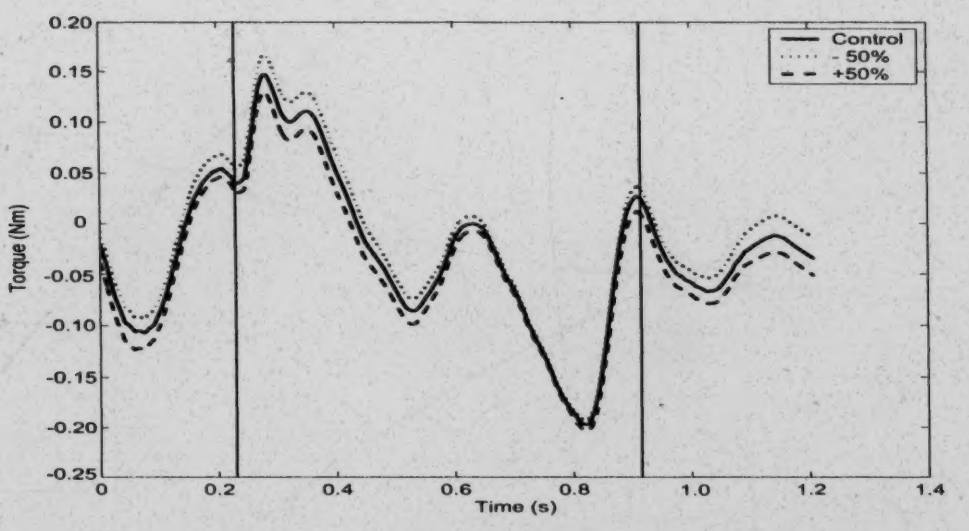

Figure 3.21: Hip joint torques estimated with $\pm 50\%$ variations in L_1.

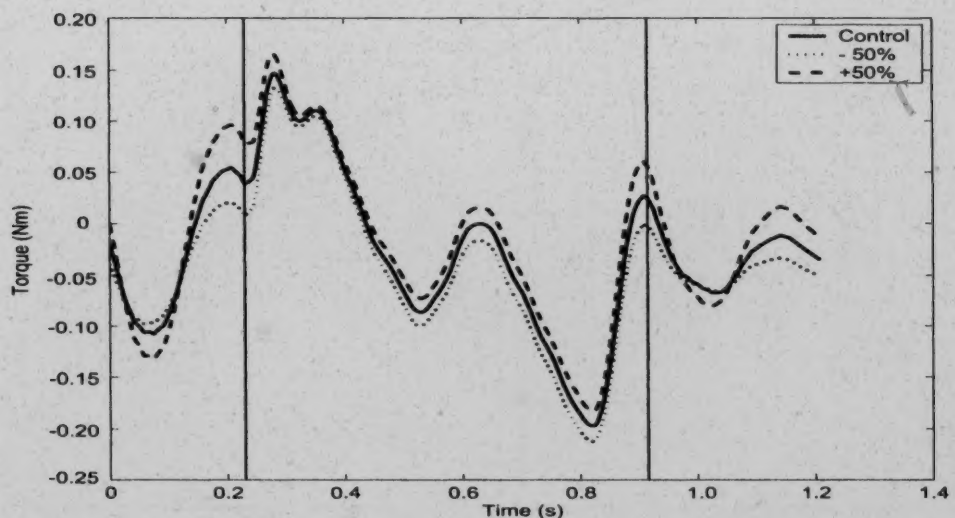

Figure 3.22: Hip joint torques estimated with $\pm 50\%$ variations in L_2.

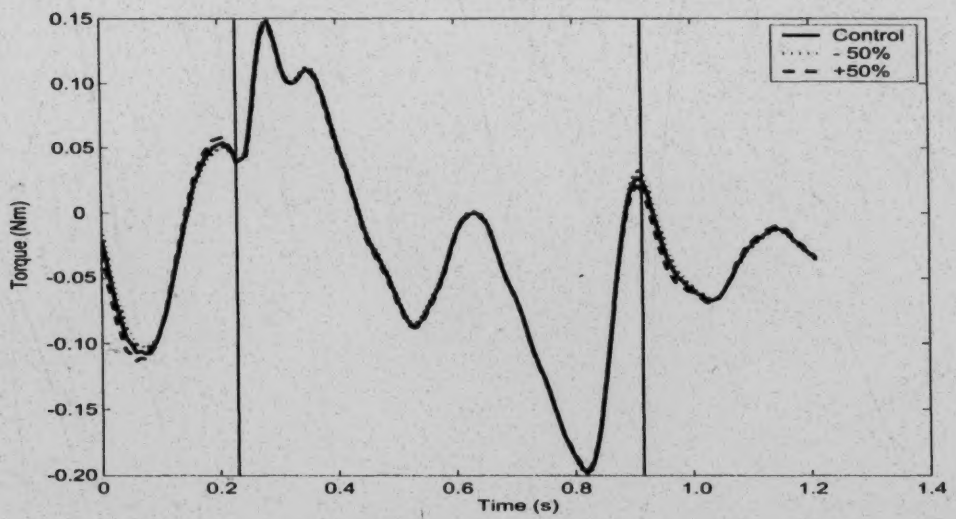

Figure 3.23: Hip joint torques estimated with ±50% variations in L_3.

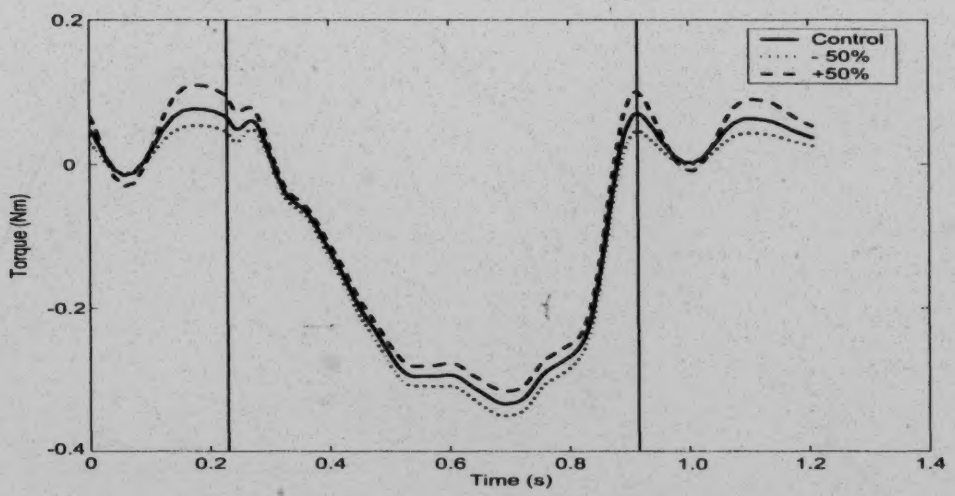

Figure 3.24: Knee joint torques estimated with ±50% variations in L_2.

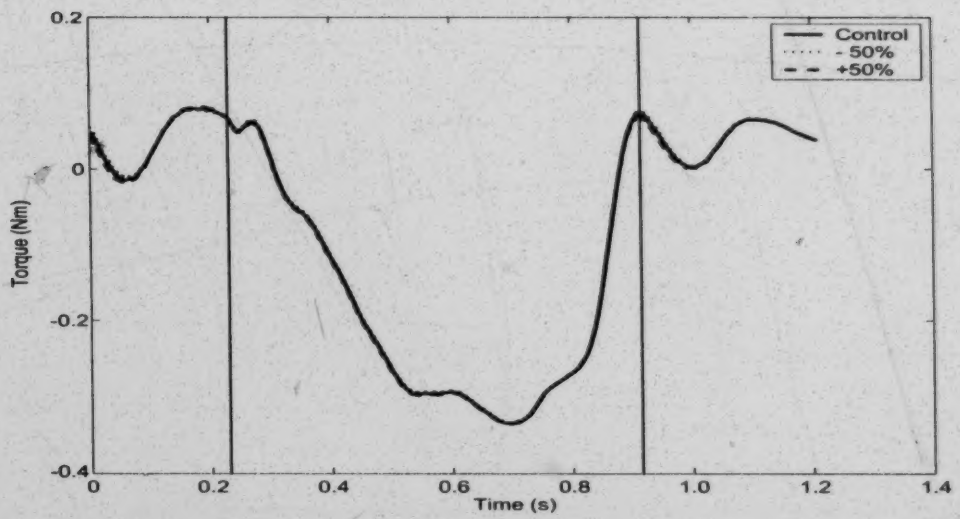

Figure 3.25: Knee joint torques estimated with $\pm 50\%$ variations in L_3.

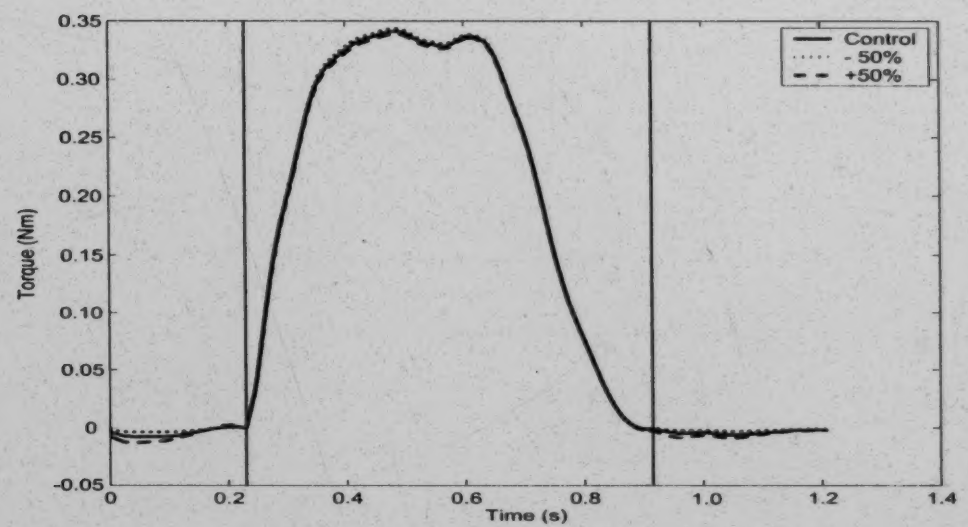

Figure 3.26: Ankle joint torques estimated with $\pm 50\%$ variations in L_3.

Unlike variations in the masses and inertias, variations in the locations of the center of mass for each limb segment did not have a linear relation, or any symmetry about the control torque, with respect to the deviations that they caused in the joint torques. This may be observed in Figure 3.22 during the swing phases. The +50% variation in L_2 causes deviations that are quite a bit larger than the −50% variation in L_2 near t = 0.075 s. The non-linearity of the relationship between the variables L_1, L_2, and L_3 can be inferred from the Equation 3.1, as each one of L_1, L_2, and L_3 are all second order variables. In general the negative variations in the center of mass location of each hindlimb segment, which moved the center of mass locations closer towards the hip joint, resulted in much smaller deviations in the joint torques than those caused by the positive variations.

3.5.4 Sensitivity Summary

Of the segmental limb parameters that were investigated the center of mass location of the shank segment, L_2, proved to have the most influential effect on the estimated hip and knee joint torques.

The masses of the hindlimb segments were the next most influential segmental parameters with respect to their effects on the estimated hip and knee joint torques.

The joint torques estimated by the two-dimensional hindlimb model proved to be fairly insensitive ($< 6.9\%$ change during swing, $< 0.2\%$ change during stance) to the $\pm 50\%$ variations in the CMI values.

Earlier in Section 3.1 the hindlimb segments of the two-dimensional hindlimb model were chosen to be modeled as uniform slender rods. As shown in Table 3.1 the CMI's and center of mass locations of each hindlimb segment as calculated based upon the uniform slender rod assumption, differed from the center of mass locations and the CMI's which were predicted by Hoy and Zernicke (1985). In order to see how the estimated joint torques would be affected, the center of mass locations and CMI's of the two-dimensional hindlimb model were replaced by the center of mass locations and CMI's predicted by Hoy and Zernicke (1985). The hip, knee, and ankle joint torques estimated with the slender rod assumption and with the values predicted by Hoy and Zernicke (1985) are shown in Figures 3.27, 3.28, and 3.29 respectively.

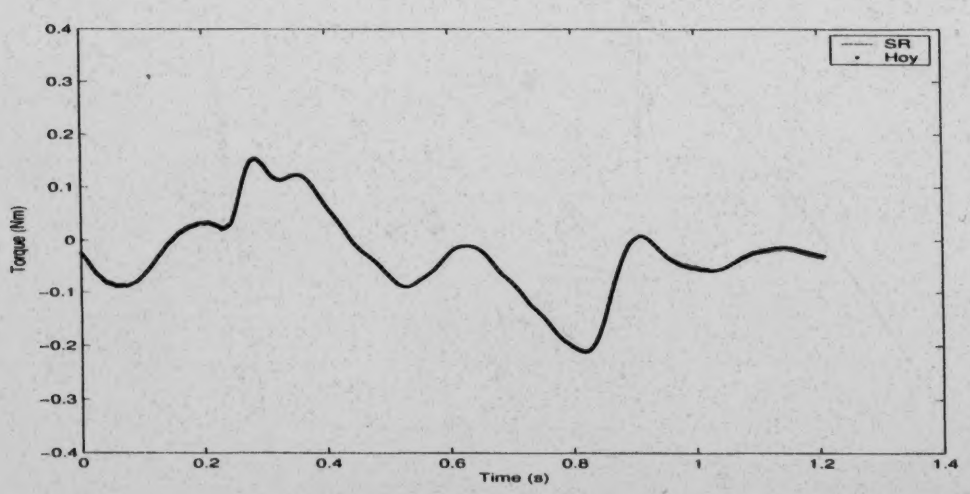

Figure 3.27: Hip joint torques estimated by the two-dimensional hindlimb model using the CMI's and center of mass locations based on the slender rod assumption [SR], and the CMI and center of mass location values predicted by Hoy and Zernicke (1985) [Hoy].

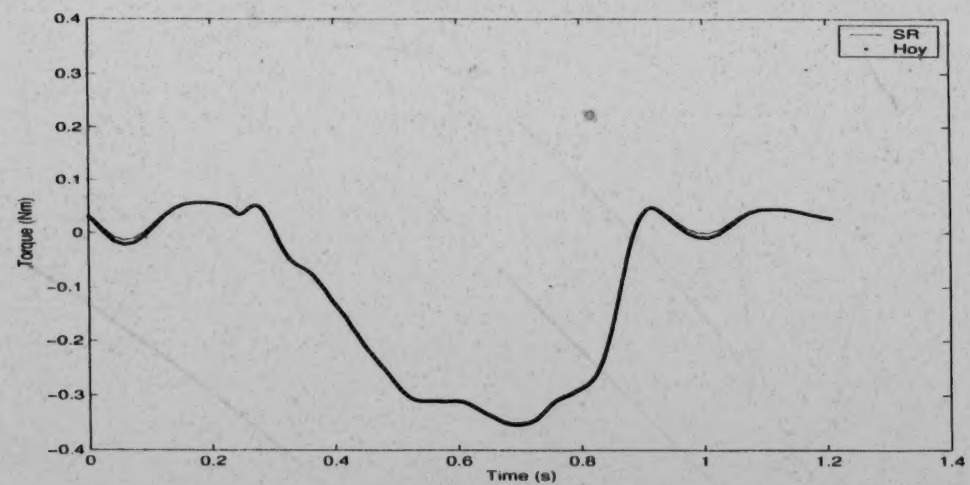

Figure 3.28: Knee joint torques estimated by the two-dimensional hindlimb model using the CMI's and center of mass locations based on the slender rod assumption [SR], and the CMI and center of mass location values predicted by Hoy and Zernicke (1985) [Hoy].

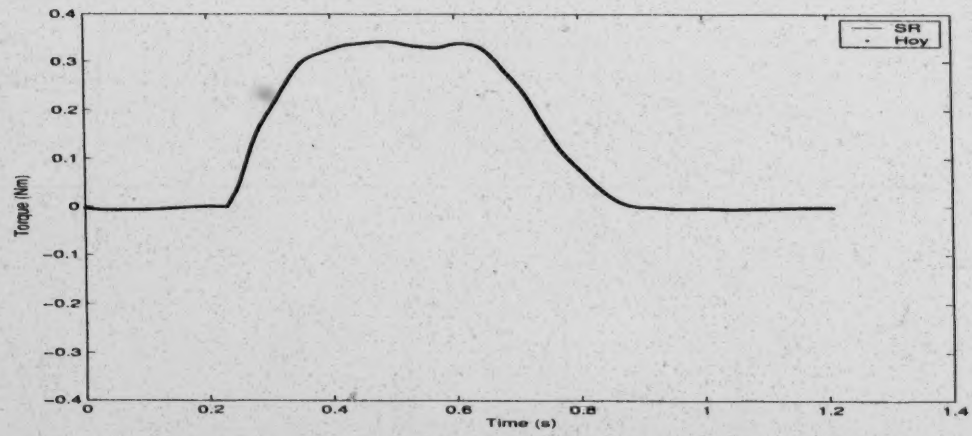

Figure 3.29: Ankle joint torques estimated by the two-dimensional hindlimb model using the CMI's and center of mass locations based on the slender rod assumption [SR], and the CMI and center of mass location values predicted by Hoy and Zernicke (1985) [Hoy].

As shown in Figures 3.27 to 3.29 the joint torques estimated using the uniform slender rod values versus the joint torques using the values predicted by Hoy and Zernicke (1985) are virtually indistinguishable from one another. Therefore the joint torques estimated using the values predicted by Hoy and Zernicke (1985) were subtracted from the joint torques estimated uniform slender rod values, the results of which are shown in Figure 3.30. The maximum observed differences of 5.7×10^{-3} Nm, 8.6×10^{-3} Nm, and 3.5×10^{-4} Nm correspond to 2.9%, 2.4%, and 0.1% differences in the peak hip, knee, and ankle joint torques respectively.

The similarity between the joint torques estimated with the CMI and center of mass locations based on the uniform slender rod assumptions, and the joint torques estimated with the CMI and center of mass locations predicted by Hoy and Zernicke (1985), were somewhat surprising since the variations in the center of mass locations caused very large deviations in the estimated joint torques. However the center of mass locations were only varied by 5.7%, 7.7%, and 1.4% for the thigh, shank, and tarsal segments, respectively. These variations in the center of mass locations were far smaller than the $\pm 50\%$ variations which were investigated in Section 3.5.3. Also the center of mass locations were all moved closer to the proximal joints, which as noted in Section 3.5.3, caused smaller deviations in the estimated joint torques.

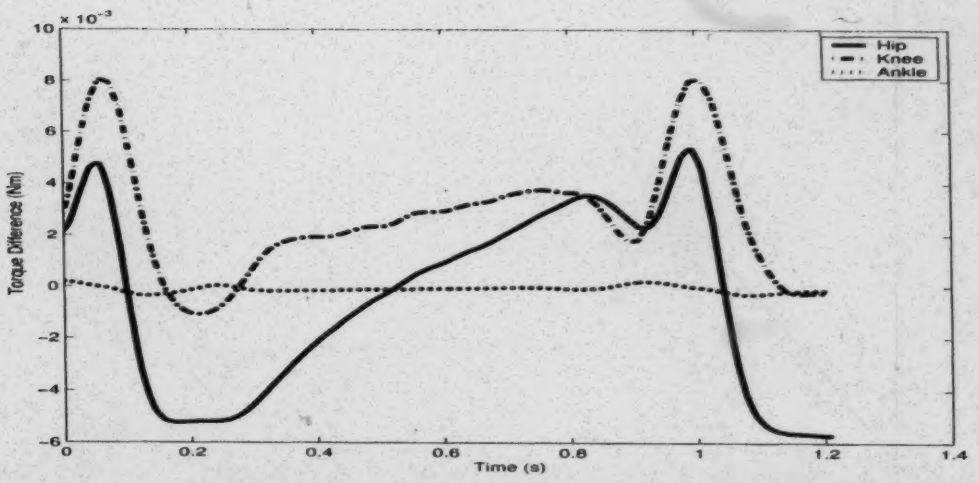

Figure 3.30: Differences between the joint torques estimated by the two-dimensional hindlimb model using the CMI's and center of mass locations based on the slender rod assumption, and the CMI and center of mass location values predicted by Hoy and Zernicke (1985).

Since the differences between the joint torques estimated with the CMI and center of mass locations based on the uniform slender rod assumptions, and the joint torques estimated with the CMI and center of mass locations predicted by Hoy and Zernicke (1985), are so small the choice of using the uniform slender rods to model the hindlimb segments is then validated. Therefore the two-dimensional hindlimb model provides an accurate representation for the estimation of the two-dimensional joint torques.

3.6 Rigid Body Paw Model

A rigid body paw was added to the two-dimensional hindlimb model to investigate how it would affect the estimated joint torques. The rigid body paw, like the rest of the two-dimensional hindlimb model, was modeled as a uniform slender rod and was attached to the two-dimensional hindlimb model at the MTP joint using a frictionless revolute joint. A free body diagram of the paw is shown in Figure 3.31. The joint torque and kinematic data for the paw adhere the same sign conventions used for the rest of the two-dimensional hindlimb model.

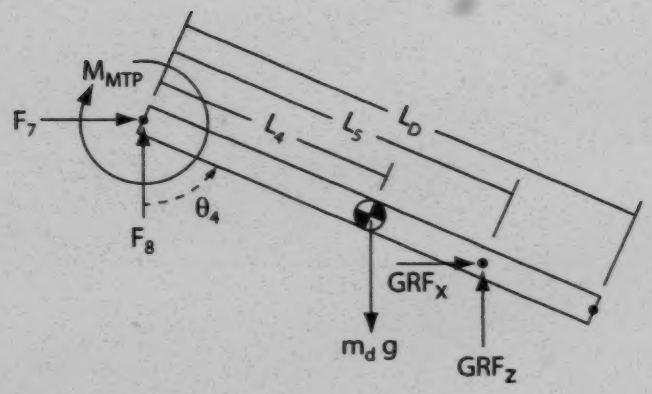

Figure 3.31: Rigid body paw model. M_{MTP} represents the MTP joint torque shown acting in the positive direction. F_7 and F_8 are the reaction forces which occur at the MTP joint.

The length of the rigid body paw, L_d, was estimated from the kinematic data as twice the mean length between the reflective marker placed on the MTP joint and the reflective marker placed on the midpoint of the paw. The mass of the paw, M_d, was found using the empirical equations presented by Hoy and Zernicke (1985). The centroidal moment of inertia, I_d, was then calculated based upon the mass and the slender rod geometry of the rigid body paw model. The segmental parameter values for the paw are shown in Table 3.5.

Table 3.5: Segment parameters for the rigid body paw.

Segment Parameter	Description	Value	Units
L_d	Length of paw	2.8	cm
L_4	Location of center of mass	$\frac{L_d}{2}$	cm
L_5	Center of pressure	$0, \frac{L_d}{4}, \frac{L_d}{2}, \frac{3L_d}{4}, L_d$	cm
I_d	CMI of paw	0.009×10^{-4}	kg·m^2
M_d	Mass of paw	13.6	g

Since center of pressure data was not available for this study five separate locations for the application of the GRF's on the rigid body paw were investigated. The joint torques estimated for each different location of GRF application could then be compared to one another to observe the what effects that the center of pressure location had on the estimated joint torques. The variable L_5, shown in Figure 3.31, describes the locations on the paw to which the GRF's were applied. Each of the locations were equidistantly spaced from one another over the entire length of the paw, where the distance between the locations was equal to $\frac{1}{4}$ the length of the paw. Thus when $L_5 = 0$ the GRF's were applied directly to the MTP joint, while for $L_5 = L_d$ the GRF's were applied to the end of the rigid body paw.

The kinematic data for the paw was calculated from the reflective marker placed on the MTP joint and the reflective marker placed on the midpoint of the paw. The same methods used to calculate the kinematic data for thigh, shank, and tarsal segments of the two-dimensional hindlimb model were used to calculate the kinematic data for the paw, as discussed in Chapter 2. The estimated joint angles (Θ_4), angular velocities ($\dot{\Theta}_4$), and angular accelerations ($\ddot{\Theta}_4$) for the paw are shown in Figure 3.32, Figure 3.33, and Figure 3.34, respectively. While the data shown in Figures 3.32 to 3.34 may not appear to be quite as smooth as the two-dimensional kinematic data shown in Chapter 2, Section 2.2.2, it was calculated from the same positional data set and subject to filtering with the same Butterworth filter.

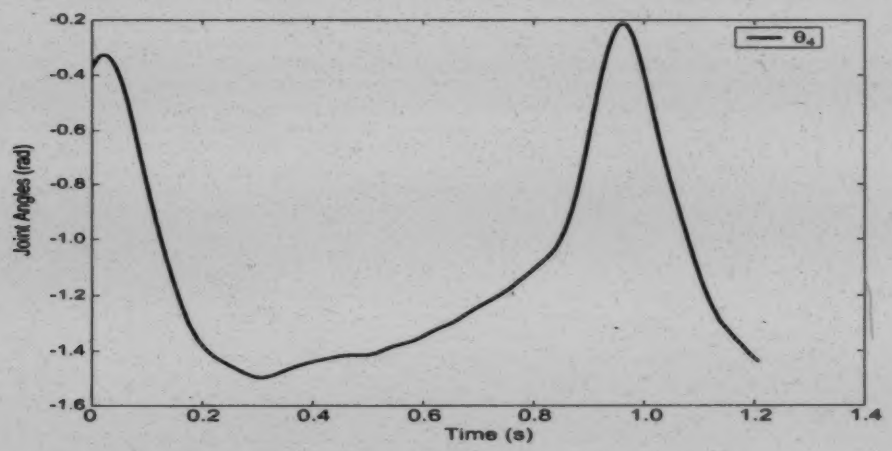

Figure 3.32: Joint angles for the rigid body paw.

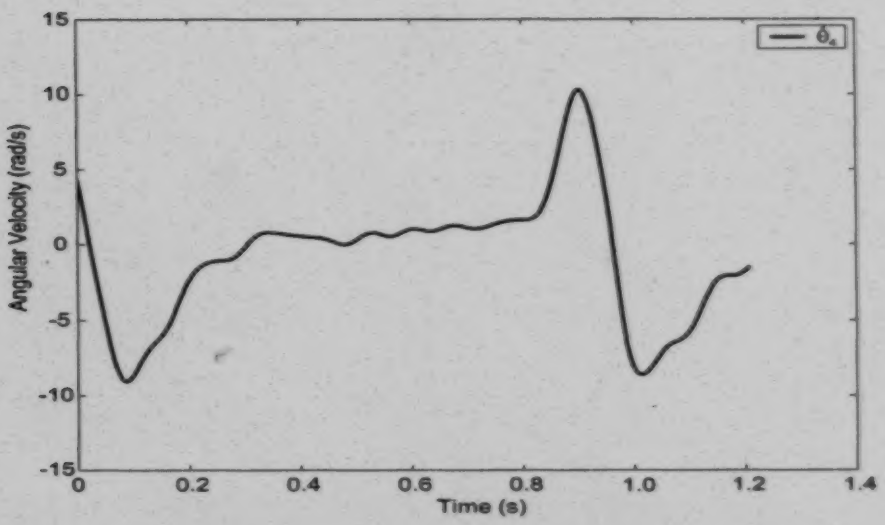

Figure 3.33: Angular velocities for the rigid body paw.

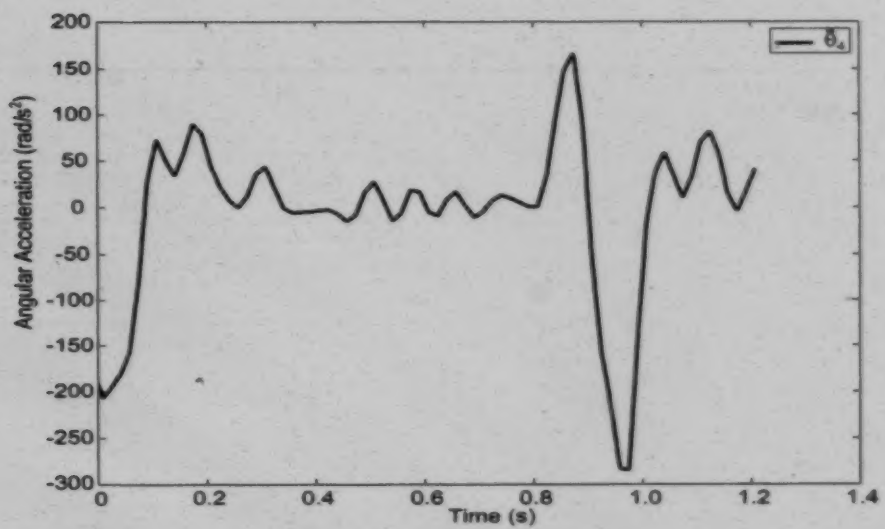

Figure 3.34: Angular velocities for the rigid body paw.

3.6.1 Equations of Motion with Rigid Body Paw

Autolev was again used to solve for Kane's dynamical equations of motion for the four segment, two-dimensional hindlimb model, and are shown in Equations (3.4) to (3.7). With the additon of the paw to the two-dimensional hindlimb model an additional joint torque about the MTP joint was created, hence there are four equations of motion. Kane's equations were implemented into a MATLAB® program created to solve the equations for the hip, knee, ankle, and MTP joint torques when given the kinematic and ground reaction force data as the inputs.

$$\begin{aligned} T_{hip} &= T_{knee} + L_a(GRF_x\cos\Theta_1 - GRF_z\sin\Theta_1) \\ &\quad + L_a(L_2M_b + L_bM_c + L_bM_d)\sin(\Theta_1-\Theta_2)\dot{\Theta}_2^2 \\ &\quad + L_a(L_3M_c + L_cM_d)\sin(\Theta_1-\Theta_3)\dot{\Theta}_3^2 + L_4L_aM_d\sin(\Theta_1-\Theta_4)\dot{\Theta}_4^2 \\ &\quad + g\big(L_1M_a + L_a(M_b+M_c+M_d)\big)\sin\Theta_1 \\ &\quad + \big(I_a + M_aL_1^2 + (M_b+M_c+M_d)L_a^2\big)\ddot{\Theta}_1 \\ &\quad + L_a\big(L_2M_b + L_b(M_c+M_d)\big)\cos(\Theta_1-\Theta_2)\ddot{\Theta}_2 \\ &\quad + L_a(L_3M_c + L_cM_d)\cos(\Theta_1-\Theta_3)\ddot{\Theta}_3 + L_4L_aM_d\cos(\Theta_1-\Theta_4)\ddot{\Theta}_4 \end{aligned} \tag{3.4}$$

$$\begin{aligned} T_{knee} &= T_{ankle} + L_b(GRF_x\cos\Theta_2 - GRF_z\sin\Theta_2) \\ &\quad - L_a(L_2M_b + L_bM_c + L_bM_d)\sin(\Theta_1-\Theta_2)\dot{\Theta}_1^2 \\ &\quad + L_b(L_3M_c + L_cM_d)\sin(\Theta_2-\Theta_3)\dot{\Theta}_3^2 + L_4L_bM_d\sin(\Theta_2-\Theta_4)\dot{\Theta}_4^2 \\ &\quad + g\big(L_2M_b + L_b(M_c+M_d)\big)\sin\Theta_2 \\ &\quad + L_a(L_2M_b + L_bM_c + L_bM_d)\cos(\Theta_1-\Theta_2)\ddot{\Theta}_1 \\ &\quad + \big(I_b + M_bL_2^2 + (M_c+M_d)L_b^2\big)\ddot{\Theta}_2 \\ &\quad + L_b(L_3M_c + L_cM_d)\cos(\Theta_2-\Theta_3)\ddot{\Theta}_3 + L_4L_bM_d\cos(\Theta_2-\Theta_4)\ddot{\Theta}_4 \end{aligned} \tag{3.5}$$

$$
\begin{aligned}
T_{ankle} \;=\; & T_{mtp} + L_c(GRF_x \cos\Theta_3 - GRF_z \sin\Theta_3) \\
& -L_a(L_3M_c + L_cM_d)\sin(\Theta_1-\Theta_3)\dot{\Theta}_1^2 \\
& -L_b(L_3M_c + L_cM_d)\sin(\Theta_2-\Theta_3)\dot{\Theta}_2^2 + L_4L_cM_d\sin(\Theta_3-\Theta_4)\dot{\Theta}_4^2 \\
& +g(L_3M_c + L_cM_d)\sin\Theta_3 + L_a(L_3M_c + L_cM_d)\cos(\Theta_1-\Theta_3)\ddot{\Theta}_1 \\
& +L_b(L_3M_c + L_cM_d)\cos(\Theta_2-\Theta_3)\ddot{\Theta}_2 + (I_c + M_cL_3^2 + M_dL_c^2)\ddot{\Theta}_3 \\
& +L_4L_cM_d\cos(\Theta_3-\Theta_4)\ddot{\Theta}_4
\end{aligned}
\tag{3.6}
$$

$$
\begin{aligned}
T_{mtp} \;=\; & L_5(GRF_x \cos\Theta_4 - GRF_z \sin\Theta_4) + gL_4M_d\sin\Theta_4 \\
& -L_4L_aM_d\sin(\Theta_1-\Theta_4)\dot{\Theta}_1^2 - L_4L_bM_d\sin(\Theta_2-\Theta_4)\dot{\Theta}_2^2 \\
& -L_4L_cM_d\sin(\Theta_3-\Theta_4)\dot{\Theta}_3^2 + L_4L_aM_d\cos(\Theta_1-\Theta_4)\ddot{\Theta}_1 \\
& +L_4L_bM_d\cos(\Theta_2-\Theta_4)\ddot{\Theta}_2 + L_4L_cM_d\cos(\Theta_3-\Theta_4)\ddot{\Theta}_3 \\
& +(I_d + M_dL_4^2)\ddot{\Theta}_4
\end{aligned}
\tag{3.7}
$$

3.6.2 Estimated Joint Torques

The estimated MTP joint torques are shown in Figure 3.35 for each value of L_5 investigated. Only during the stance phase ($t = 0.23$ s to $t = 0.92$ s) were any differences observed in the estimated MTP joint torque, due to the GRF's acting on the rigid body paw. For the case in which $L_5 = 0$ the estimated MTP joint torques were very close to zero as the only forces acting on the paw were the gravitational and inertial forces. As the magnitude of L_5 was increased, and the location to which the GRF's were applied was moved further along the paw towards the digits, the magnitude of the estimated MTP joint torques also increased. A linear relationship was observed between the increases in the location of the center of pressure and the increases observed in the magnitude of the MTP joint torques. At each discrete time step the magnitude of the increase in the estimated MTP joint torque was identical for each subsequent increase in L_5. To illustrate this result the observed peak magnitude of the MTP joint torque when $L_5 = \frac{L_d}{4}$ was found to be 0.080 Nm at $t = 0.633$ s. When L_5 was increased to $L_5 = \frac{L_d}{2}$ the observed peak magnitude in the MTP joint torque increased by another 0.080 Nm to 0.160 Nm at $t = 0.633$ s. Each time L_5 was increased by 25% of the total length of the paw, the magnitude

of the estimated MTP joint torque at $t = 0.633$ s increased by 0.080 Nm.

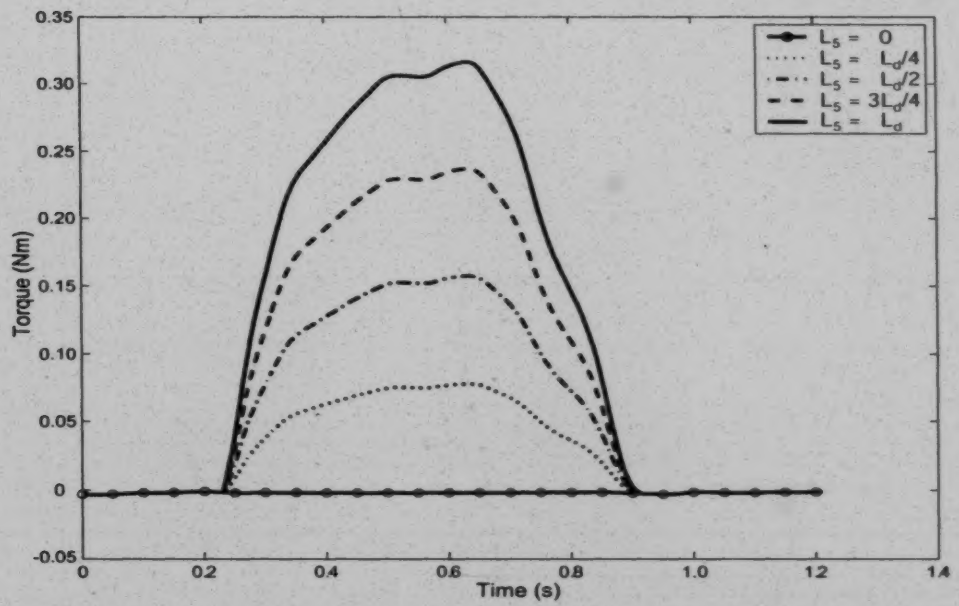

Figure 3.35: Estimated MTP joint torques calculated calculated for different locations of center of pressure application.

The estimated joint torques for the hip, knee, and ankle joints are shown in Figures 3.36 to 3.38. Each of these joint torques were affected by the changes in L_5 since the joint torques are dependant on one another. The joint torques dependance on each other can be observed from the equations of motion where the hip joint torque is affected by the knee joint torque, which is affected by the ankle joint torque, which in turn is affected by the MTP joint torque. The linear relationship between L_5 and the changes in magnitude observed in the MTP joint torque was also observed in the hip, knee, and ankle joint torques. For the case in which $L_5 = \frac{L_d}{4}$ which caused the MTP joint torque to increase by 0.080 Nm at $t = 0.633$ s, each of the other three joint torques saw a change in magnitude of 0.080 Nm at $t = 0.633$ s as well. An increase in magnitude of 0.080 Nm was observed in the hip and ankle torques, while a decrease in magnitude of 0.080 Nm was observed in the knee torque.

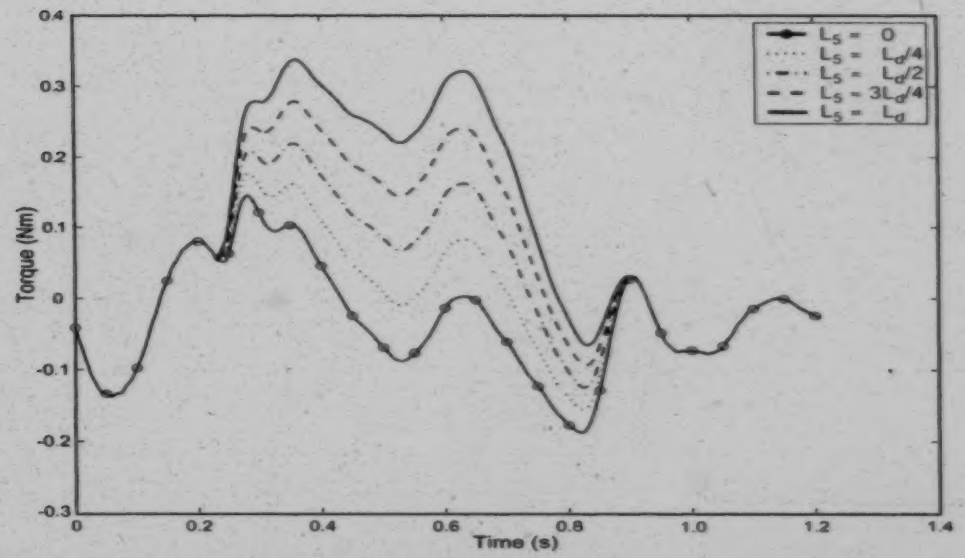

Figure 3.36: Estimated hip joint torques calculated for different locations of center of pressure application.

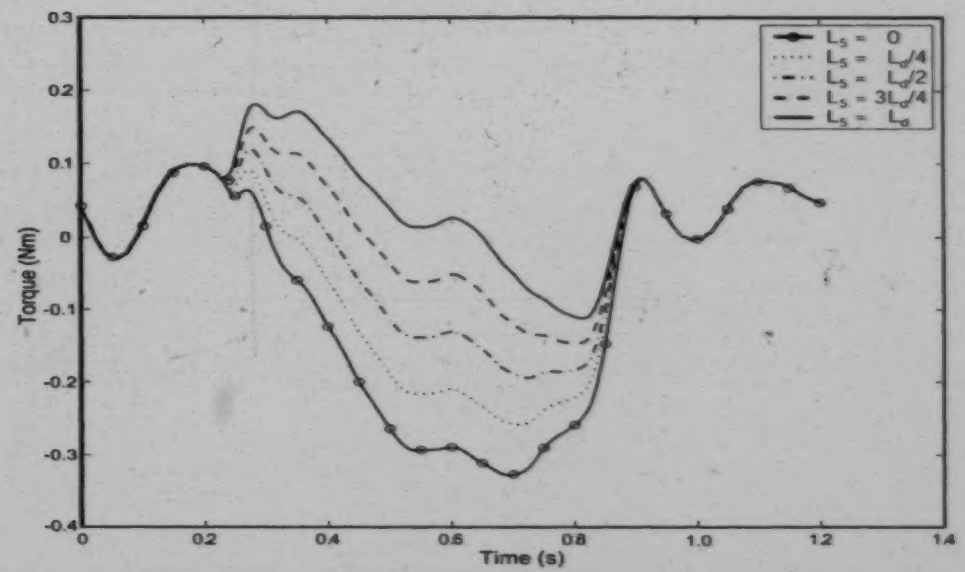

Figure 3.37: Estimated knee joint torques calculated for different locations of center of pressure application.

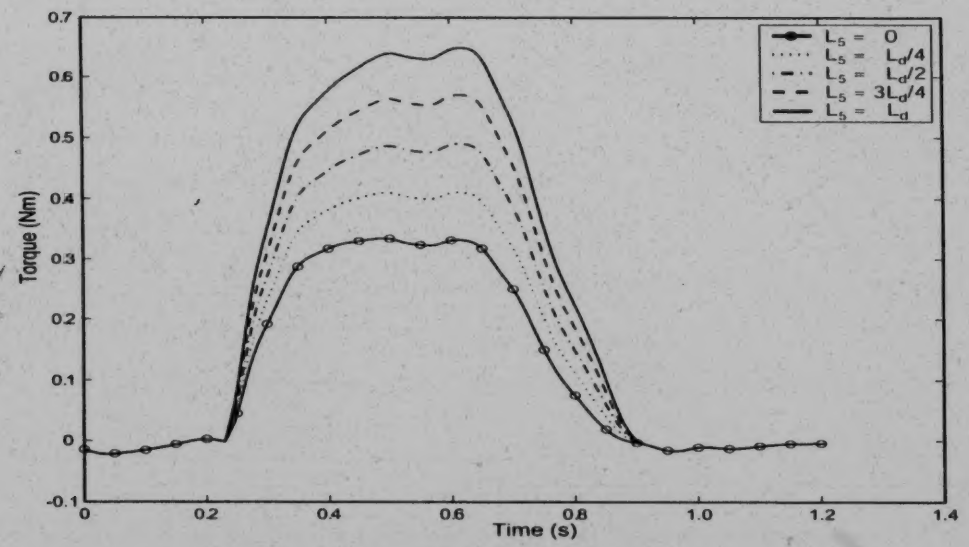

Figure 3.38: Estimated ankle joint torques calculated for different locations of center of pressure application.

As shown in Figures 3.36 to 3.38, the location to which the GRF's are applied to the paw has a significant impact on the joint torques estimated by the hindlimb model during the stance phase. When the GRF's were applied to the middle of the rigid paw ($L_5 = \frac{L_d}{2}$), it was found that the hip, knee, and ankle joint torques estimated by the hindlimb model each increased by 0.16 Nm (t = 0.633 s) over the joint torques estimated when the GRF's were applied to the MTP joint. When the GRF's were applied to the end of the rigid paw it was found that the hip, knee, and ankle joint torques increased by 0.32 Nm (t = 0.633 s) respectively, over the joint torques estimated by the two-dimensional model without a paw.

3.6.3 Rigid Body Paw Summary

The location along the paw to which the GRF's are applied is a highly important consideration for the estimation of the joint torques. Variations in the location on the paw to which the GRF's are applied have a far more significant effect on the estimated joint torques than any of the ±50% variations in the segmental masses, centroidal moments of inertia, and center of mass locations of the hindlimb model.

Figure 3 in Fowler et al. (1993) shows that for walking on a level surface the center of pressure initially acts at the middle of the paw and moves towards the digits over the duration of the stance phase. Assuming that this result is also representative of the cat's from which the kinematic and GRF data was collected for this study, bounds can then be created for the amount of variation in the estimated hip, knee, and ankle torques which could be expected over the duration of the stance phase, if a rigid paw was included in the two-dimensional hindlimb model. Thus if center of pressure data was available for this study and a rigid body paw was included in the two-dimensional hindlimb model as outlined above, the magnitudes of the estimated hip and ankle joint torques would be increased by at least 0.16 Nm (GRF's applied to the middle of the paw), and at most by 0.32 Nm (GRF's applied to the end of the paw), of their respective values. The magnitude of the estimated knee joint torque would be decreased by at least 0.16 Nm and at most 0.32 Nm of it's respective values.

Chapter 4

Three-Dimensional Inverse Dynamics Model

When studying animal locomotion researchers often restrict their analysis of the motion of the animal's limbs to the sagittal plane [Fowler et al. (1993); Goslow et al. (1973); Herr and McMahon (2000); Hoy and Zernicke (1986); Manter (1938); Neveu et al. (2001); Shen and Poppele (1995); Trank and Smith (1996)]. In this study, the sagittal plane coincides with the X-Z plane of the global reference frame. An assumption is made that any movement which occurs outside of the sagittal plane during locomotion is small enough that it would have a negligible effect on the analysis.

To investigate the validity of the two-dimensional motion assumption, an additional degree of freedom was added to the hip joint of the two-dimensional hindlimb model. The extra degree of freedom allowed for adduction and abduction of the hip so that the model could then incorporate motion outside of the sagittal plane, which will be referred to as the out of plane motion. The joint torques could then be calculated by both the two-dimensional and three-dimensional models to determine if any significant differences exist between them.

4.1 Three-Dimensional Hindlimb Model

Out of plane motion for the two-dimensional hindlimb model was created by allowing rotation at the hip joint about the X-axis of the global reference frame. The amount of hindlimb rotation about the Z-axis is much smaller than the abduction and adduction movement about the X-axis at the hip. Therefore this study will focus only on the abduction and adduction movement about the X-axis at the hip joint.

The mass of the animal for which the three-dimensional kinematic and GRF data was collected was not provided, so a total cat mass of 4 kg was assumed, as it was for the cat from which the two-dimensional kinematic data was collected. The segmental parameters for the three-dimensional hindlimb model are shown in Table 4.1. The moments of inertia shown in Table 4.1 represent both principal moments of inertia, I_x and I_y, about the center of mass for each hindlimb segment. Since each hindlimb segment is modeled as a uniform slender rod $I_x = I_y$, while $I_z = 0$.

Table 4.1: Table of three-dimensional hindlimb model segmental variables.

Variable	Description	Value	Units
I_a	CMI of limb segment A	141.8×10^{-6}	kg·m^2
I_b	CMI of limb segment B	66.8×10^{-6}	kg·m^2
I_c	CMI of limb segment C	7.1×10^{-6}	kg·m^2
M_a	Mass of limb segment A	195	g
M_b	Mass of limb segment B	58	g
M_c	Mass of limb segment C	22	g
L_a	Length of limb segment A	9.21	cm
L_b	Length of limb segment B	9.12	cm
L_c	Length of limb segment C	5.64	cm
L_1	Center of mass location	$L_a/2$	cm
L_2	Center of mass location	$L_b/2$	cm
L_3	Center of mass location	$L_c/2$	cm

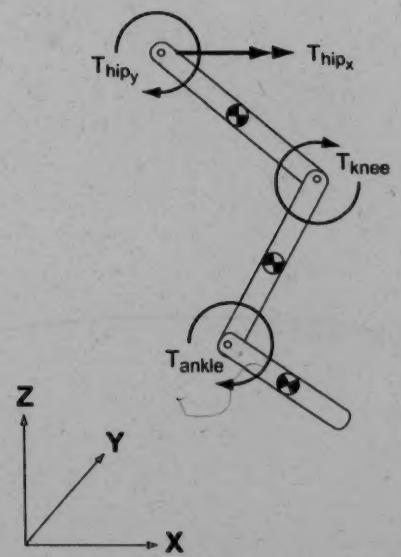

Figure 4.1: The four joint torques for the three-dimensional model. All four joint torques depicted are positive when acting in the directions shown. T_{hip_Y}, T_{knee}, and T_{ankle} are defined similarly to the two-dimensional hindlimb model, as shown in Figure 3.6.

With an additional degree of freedom added to the model, an additional torque was required to govern the abduction and adduction motion of the hip. Figure 4.1 shows all four of the joint torques for the three-dimensional hindlimb model. T_{hip_Y} and T_{hip_X} represent the hip joint torques occurring in the sagittal plane (about the Y-axis) and the adduction and abduction torque (occurring about the X-axis) respectively. Note that T_{hip_Y} is equivalent to T_{hip} of the two-dimensional hindlimb model.

4.2 Three-Dimensional Kane's Equations

Autolev was again used to formulate Kane's dynamical equations of motion for the three-dimensional hindlimb model. The Autolev code used to generate Kane's equations for the three-dimensional hindlimb model can be found in Appendix B. Once the equations of motion were formulated using Autolev they were then implemented into a MATLAB® program along with the three-dimensional kinematic and GRF data. The equations of motion could then be

solved in order to find the joint torques. The equations of motion are

$$
\begin{aligned}
T_{hip_X} \;=\; & -(L_a \sin\Theta_1 + L_b \sin\Theta_2 + L_c \sin\Theta_3)(GRF_y \cos\Theta_a + GRF_z \sin\Theta_a) \\
& + g \sin\Theta_a \left[(L_1 M_a + L_a M_b + L_a M_c)\cos\Theta_1 + (L_2 M_b + L_b M_c)\cos\Theta_2 \right. \\
& \left. + L_3 M_c \cos\Theta_3\right] - 2\sin\Theta_3 \left[I_c \cos\Theta_3 + L_3 M_c \left(L_a \cos\Theta_1 + L_b \cos\Theta_2 \right.\right. \\
& \left.\left. + L_3 \cos\Theta_3\right)\right]\dot{\Theta}_3\dot{\Theta}_a - 2\sin\Theta_2 \left[L_a(L_2 M_b + L_b M_c)\cos\Theta_1 \right. \\
& \left. + (I_b + M_b L_2^2 + M_c L_b^2)\cos\Theta_2 + L_3 L_b M_c \cos\Theta_3\right]\dot{\Theta}_2\dot{\Theta}_a \\
& - 2\sin\Theta_1 \left[\left(I_a + M_a L_1^2 + (M_b + M_c)L_a^2\right)\cos\Theta_1 + L_a(L_2 M_b + L_b M_c)\cos\Theta_2 \right. \\
& \left. + L_3 L_a M_c \cos\Theta_3\right]\dot{\Theta}_1\dot{\Theta}_a + \left[(I_a + M_a L_1^2 + M_b L_a^2)\cos^2\Theta_1 \right. \\
& + (I_b + M_b L_2^2)\cos^2\Theta_2 + (I_c + M_c L_3^2)\cos^2\Theta_3 + 2L_2 L_a M_b \cos\Theta_1 \cos\Theta_2 \\
& \left. + 2L_3 M_c \cos\Theta_3 (L_a \cos\Theta_1 + L_b \cos\Theta_2) + M_c (L_a \cos\Theta_1 + L_b \cos\Theta_2)^2\right]\ddot{\Theta}_a
\end{aligned}
\tag{4.1}
$$

$$
\begin{aligned}
T_{hip_Y} \;=\; & \left[T_{knee} + L_a \sin\Theta_1 (GRF_x \arctan\Theta_1 + GRF_y \sin\Theta_a - GRF_z \cos\Theta_a) \right. \\
& + g \sin\Theta_1 \cos\Theta_a \left(L_1 M_a + L_a (M_b + M_c)\right) + L_a L_3 M_c \sin(\Theta_1 - \Theta_3)\dot{\Theta}_3^2 \\
& + L_a (L_2 M_b + L_b M_c)\sin(\Theta_1 - \Theta_2)\dot{\Theta}_2^2 + \left[\sin\Theta_1 \left[L_a L_b M_c \cos\Theta_2 \right.\right. \\
& \left.\left. + (I_a + M_a L_1^2 + M_b L_a^2 + M_c L_a^2)\cos\Theta_1\right] + L_2 L_a M_b \cos^2\Theta_2 \left[\sin(\Theta_1 - \Theta_2) \right.\right. \\
& \left.\left. + \tan\Theta_2 \cos(\Theta_1 - \Theta_2)\right] + L_3 L_a M_c \cos\Theta_3 \left[\cos\Theta_3 \sin(\Theta_1 - \Theta_3) \right.\right. \\
& \left.\left. + \sin\Theta_3 \cos(\Theta_1 - \Theta_3)\right]\right]\dot{\Theta}_a^2 + L_a (L_2 M_b + L_b M_c)\cos(\Theta_1 - \Theta_2)\ddot{\Theta}_2 \\
& \left. + \left(I_a + M_a L_1^2 + (M_b + M_c)L_a^2\right)\ddot{\Theta}_1 + L_a L_3 M_c \cos(\Theta_1 - \Theta_3)\ddot{\Theta}_3\right]\frac{1}{\cos\Theta_a}
\end{aligned}
\tag{4.2}
$$

$$
\begin{aligned}
T_{knee} \;=\; & T_{ankle} + L_b \sin\Theta_2 (GRF_x \arctan\Theta_2 + GRF_y \sin\Theta_a - GRF_z \cos\Theta_a) \\
& - L_a (L_2 M_b + L_b M_c) \sin(\Theta_1 - \Theta_2) \dot{\Theta}_1^2 + L_b L_3 M_c \sin(\Theta_2 - \Theta_3) \dot{\Theta}_3^2 \\
& + \Big[\big[(I_b + M_b L_2^2 + M_c L_b^2) \cos\Theta_2 + L_a (L_2 M_b + L_b M_c) \cos\Theta_1 \big] \sin\Theta_2 \\
& + L_b L_3 M_c \big[\cos^2\Theta_3 \sin(\Theta_2 - \Theta_3) + \sin\Theta_3 \cos\Theta_3 \cos(\Theta_2 - \Theta_3) \big] \Big] \dot{\Theta}_a^2 \\
& + L_a (L_2 M_b + L_b M_c) \cos(\Theta_1 - \Theta_2) \ddot{\Theta}_1 + (I_b + M_b L_2^2 + M_c L_b^2) \ddot{\Theta}_2 \\
& + L_b L_3 M_c \cos(\Theta_2 - \Theta_3) \ddot{\Theta}_3 + g \sin\Theta_2 \cos\Theta_a (L_2 M_b + L_b M_c)
\end{aligned}
\tag{4.3}
$$

$$
\begin{aligned}
T_{ankle} \;=\; & L_c \sin\Theta_3 (GRF_x \arctan\Theta_3 + GRF_y \sin\Theta_a - GRF_z \cos\Theta_a) \\
& - L_a L_3 M_c \sin(\Theta_1 - \Theta_3) \dot{\Theta}_1^2 - L_b L_3 M_c \sin(\Theta_2 - \Theta_3) \dot{\Theta}_2^2 \\
& + \sin\Theta_3 \big[I_c \cos\Theta_3 + L_3 M_c (L_a \cos\Theta_1 + L_b \cos\Theta_2 + L_3 \cos\Theta_3) \big] \dot{\Theta}_a^2 \\
& + g L_3 M_c \sin\Theta_3 \cos\Theta_a + L_a L_3 M_c \cos(\Theta_1 - \Theta_3) \ddot{\Theta}_1 \\
& + L_b L_3 M_c \cos(\Theta_2 - \Theta_3) \ddot{\Theta}_2 + (I_c + M_c L_3^2) \ddot{\Theta}_3
\end{aligned}
\tag{4.4}
$$

Recall that the adduction and abduction motion is represented by Θ_a, as defined in Chapter 2, Section 2.2.2.

4.3 Three-Dimensional Joint Torques

The estimated joint torques calculated using the three-dimensional hindlimb model are shown in Figure 4.2. Vertical lines have been used in the figure to indicate the transitions between the swing and stance phases. The first transition occurs at 0.11 s as the hindlimb exits the first swing phase and enters the stance phase when the paw comes into contact with the ground. The stance phase then continues until 0.39 s at which point the paw loses contact with the surface, and the limb enters into a second swing phase. Figure 4.3 has been included to aid in the discussion of the joint torques by providing a visual representation of some of the positions of the hindlimb during the swing phases and the stance phase.

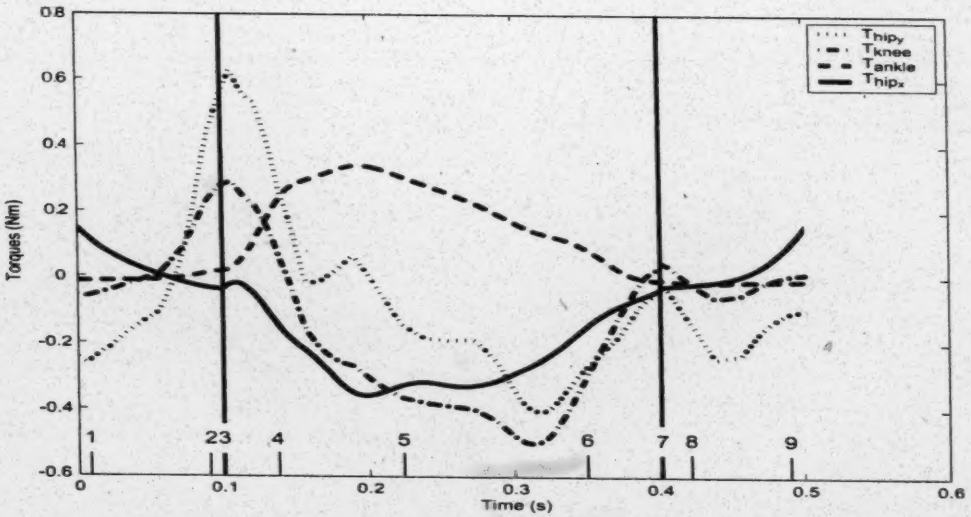

Figure 4.2: Joint torques estimated by the three-dimensional inverse dynamics hindlimb model. The vertical lines indicate the transitions between the swing and stance phases. The small vertical bars, numbered $1 - 9$, represent the times corresponding to each limb position shown in Figure 4.3.

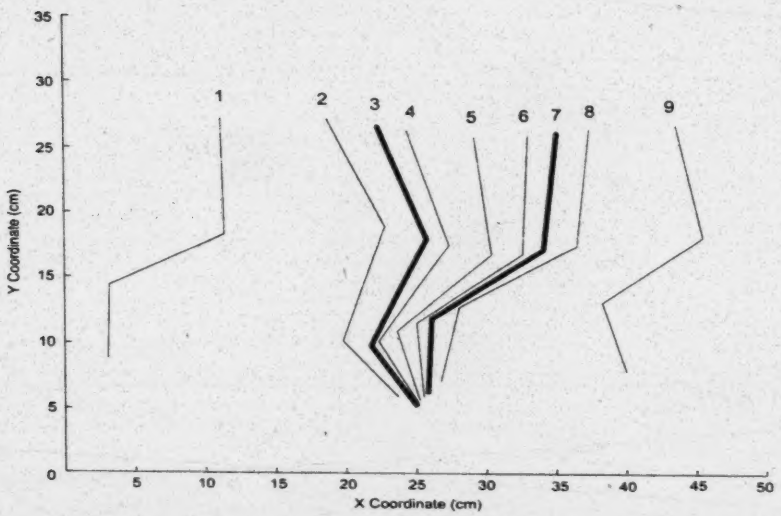

Figure 4.3: Selected hindlimb positions corresponding to Figure 4.2. Positions 3 and 7 have been darkened as they show the beginning and end of the stance phase.

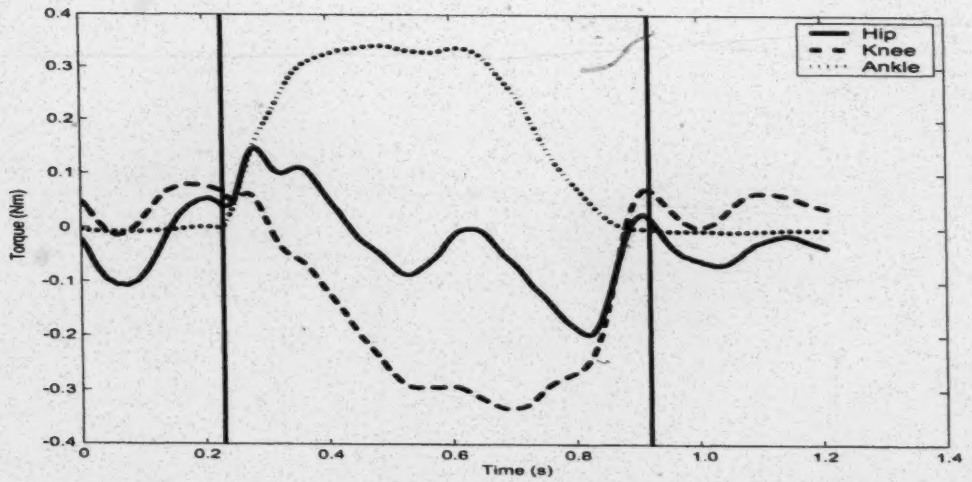

Figure 4.4: Joint torques estimated by the two-dimensional inverse dynamics hindlimb model. The vertical lines ($t = 0.23$s and $t = 0.92$ s) represent the transitions between the swing and stance phases.

Since two different cats were used for the collection of the two-dimensional kinematic and GRF data, and the three-dimensional kinematic and GRF data, the joint torques estimated using the two separate data sets are not the same. The joint torques estimated from the two-dimensional kinematic and GRF data sets, previously shown in Figure3.7, have also been included here in Figure 4.4 to aid in the discussion. The most noticeable difference between the joint torques estimated from the two-dimensional and three-dimensional kinematic and GRF data sets is the large spike in the magnitude of the hip torque, and to a slightly lesser degree the knee torque, during the transition between the swing phase to the stance phase shown in Figure 4.2. The spike in the joint torques can be attributed to the large angular accelerations of the thigh and shank portions of the hindlimb during the first swing phase (see Figure 2.14). The static joint torques and dynamic joint torques for this data set have been included in Figure 4.5 and Figure 4.6 respectively. As shown in Figure 4.6 the dynamic joint torques are responsible for the spike in the estimated joint torques near the swing phase to stance phase transition. This further highlights why the dynamic torques should not be excluded from the joint torque estimation during the stance phase, as mentioned earlier in Section 3.4. Aside from the spikes in the hip and knee torques, the joint torques estimated from the two-dimensional and three-dimensional kinematic and GRF data sets display many of the same characteristics.

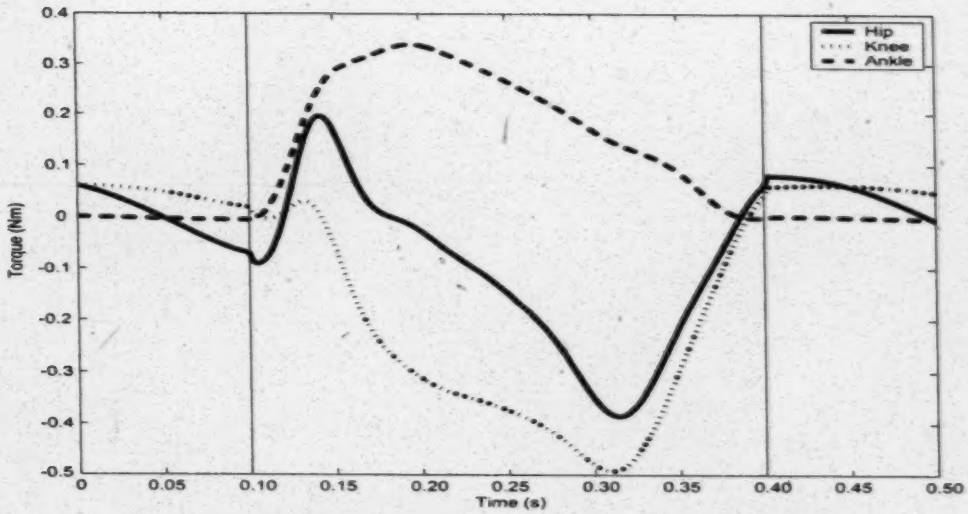

Figure 4.5: Static contributions to the estimated joint torques.

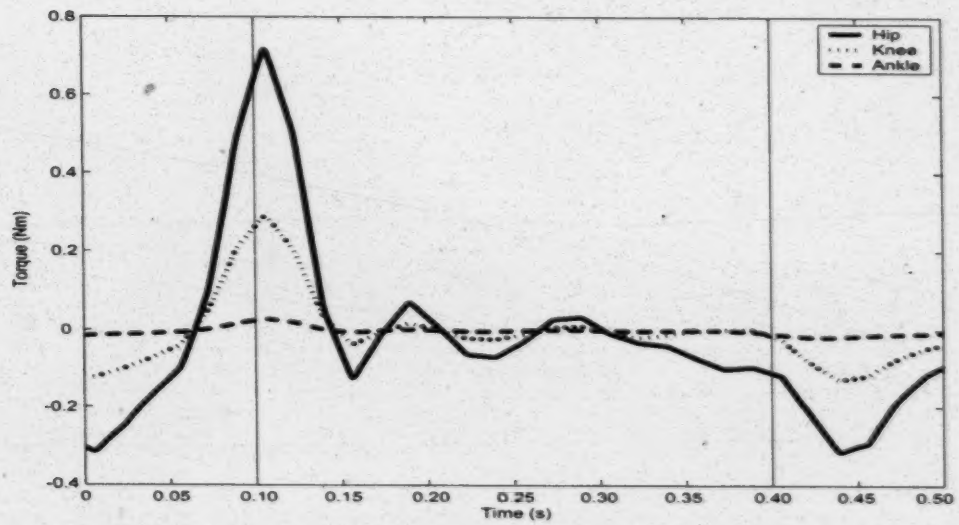

Figure 4.6: Dynamic contributions to the estimated joint torques.

The new joint torque T_{hip_X}, shown in Figure 4.2, initially starts as an adduction torque swinging the leg towards the body during the first swing phase (position 1). Over the last portion of the first swing phase T_{hip_X} becomes negative, as it switches to an abduction torque to slow the hindlimb, so that the hindlimb will be positioned near perpendicular with the surface for the onset of the stance phase (position 2). During the swing phases the primary contribution to the magnitude of T_{hip_X} comes from $\ddot{\theta}_a$, the angular acceleration due to the adduction and abduction motion of the hindlimb. During the stance phase the GRF's become the major contributors to T_{hip_X}. During the stance phase (positions 3 - 7) the hip swings out slightly over the paw in the negative Y direction, therefore the abduction torque supplied by T_{hip_X} prevents the hips from collapsing laterally. Over the last portion of the stance phase T_{hip_X} gradually increases back towards zero, however remaining an abduction torque over the first portion of the second swing phase in order to swing the hindlimb out away from the body once more. The peak magnitude of $T_{hip_X} = 0.36$ Nm, is very close to the peak magnitude of $T_{ankle} = 0.34$ Nm, and also close to the peak magnitude of $T_{knee} = 0.50$ Nm during the stance phase.

4.4 Two-Dimensional and Three-Dimensional Joint Torque Comparison

The three-dimensional kinematic data set in which the abduction and adduction motion (Θ_a) was approximated, and the three-dimensional GRF data was used to calculate the joint torques from both the two-dimensional and three-dimensional hindlimb models. For the estimation of the two-dimensional joint torques, the hip abduction and adduction motion and the ground reaction forces acting in the Y-axis of the global reference frame were simply ignored.

The joint torques estimated by both the two-dimensional and the three-dimensional hindlimb models are shown in Figures 4.7, 4.8, and 4.9. The differences observed between the hip, knee, and ankle torques, as estimated by the two-dimensional and three-dimensional hindlimb models respectively, were very small. Each one of the joint torques estimated by the three-dimensional model were subtracted from their counterparts estimated by the two-dimensional hindlimb model. The results of which are shown in Figure 4.10. The magnitude of the differences between joint torques estimated by the two-dimensional and three-dimensional hindlimb models are less than 4.0×10^{-3} Nm.

This result validates the assumption that a planar inverse dynamics model

of the hindlimb will provide an accurate estimation of the joint torques T_{hipx} (equivalent to T_{hip}), T_{knee}, and T_{ankle}, as they have been defined in this study.

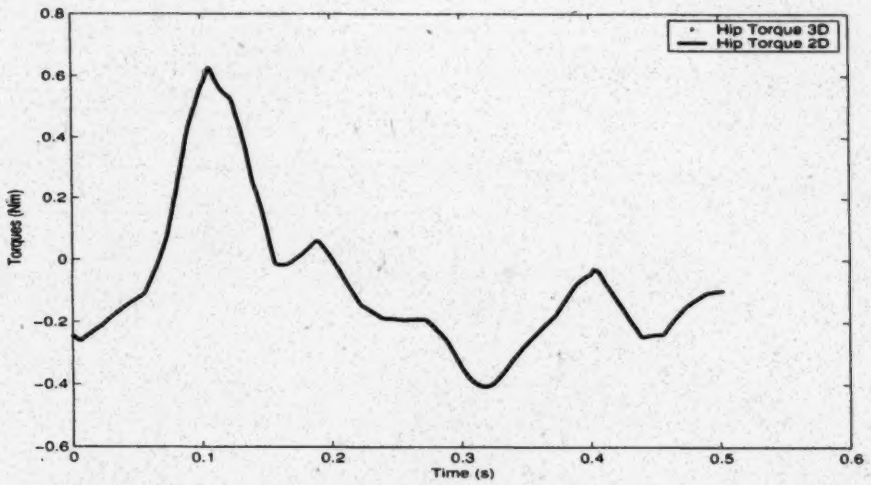

Figure 4.7: Hip joint torques estimated by both the two-dimensional and three-dimensional hindlimb models.

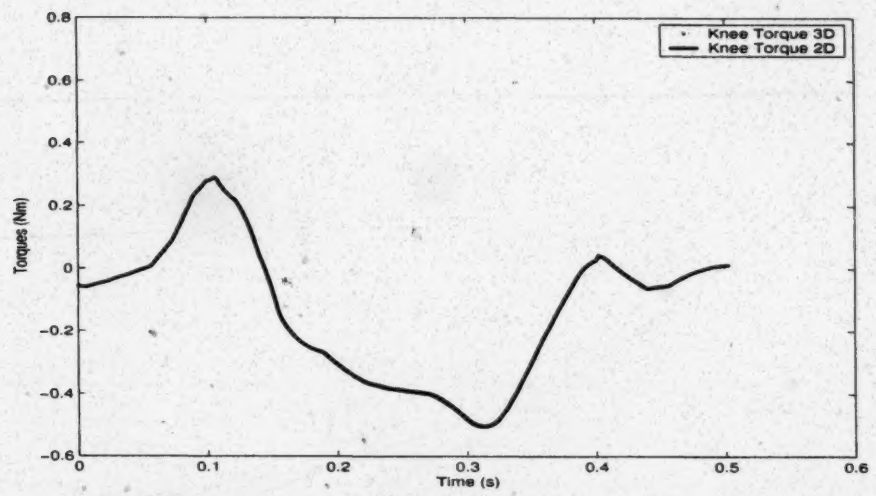

Figure 4.8: Knee joint torques estimated by both the two-dimensional and three-dimensional hindlimb models.

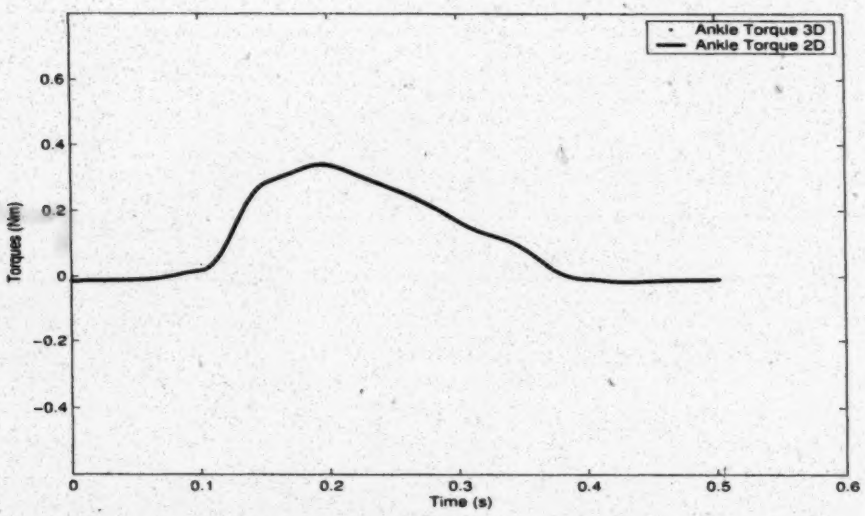

Figure 4.9: Ankle joint torques estimated by both the two-dimensional and three-dimensional hindlimb models.

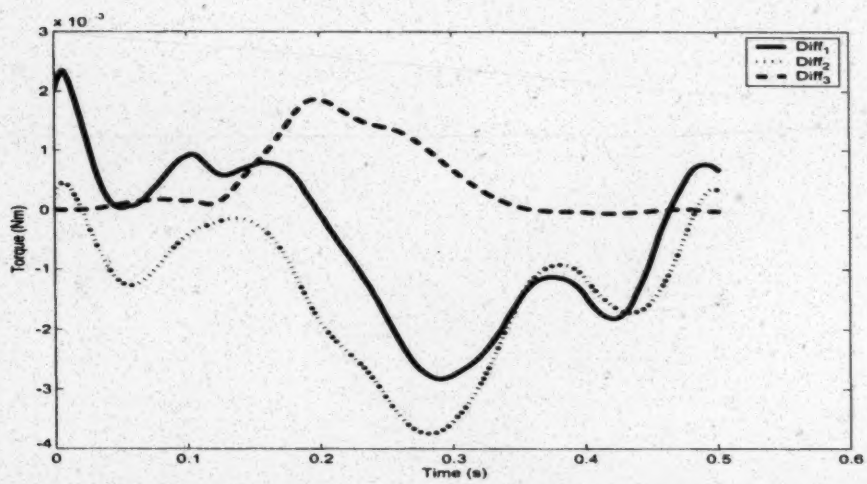

Figure 4.10: Differences between the two-dimensional and three-dimensional hindlimb torques. $Diff_1$, $Diff_2$, and $Diff_3$ represent the differences between the two-dimensional and three-dimensional hip, knee, and ankle joint torques respectively.

Chapter 5

Two-Dimensional Forward Dynamics

In Chapter 3 a two-dimensional inverse dynamics hindlimb model was developed to provide an estimate of the joint torques which occur within the hindlimb of a cat for walking on a level surface. In this chapter a two-dimensional forward dynamics model will be developed. In forward dynamics the forces and moments which act upon the system are used to calculate the resultant motion. The joint torques estimated from the inverse dynamics for the two-dimensional hindlimb model, along with the measured two-dimensional GRF's, will be used for the forward dynamics simulations.

5.1 Two-Dimensional Forward Dynamics Model

The two-dimensional hindlimb model is used for both the inverse dynamics and the forward dynamics simulations. The difference between the two is in the way that the equations of motion are solved. For inverse dynamics, the known kinematics are used to estimate the forces and moments occurring in each joint of the two-dimensional hindlimb model. The forward dynamics simulations, on the other hand, determine the motion of a system for a given set of applied forces and moments. As a test, a forward dynamics simulation can be performed using the joint torques obtained from an inverse dynamics simulation as inputs. In principle this should result in a motion which is identical to the original kinematics. This can be used to verify the results of both forward and inverse dynamics procedures.

For the forward dynamics simulations the equations of motion were arranged into matrices such that all of the acceleration terms (all second order terms) were located on the right hand side of the equations, while the remaining terms were located on the left hand side of the equations, as shown in Equation 5.1.

$$\begin{bmatrix} & & \\ & A & \\ & & \end{bmatrix} \begin{bmatrix} \ddot{\Theta}_1 \\ \ddot{\Theta}_2 \\ \ddot{\Theta}_3 \end{bmatrix} = \begin{bmatrix} \\ B \\ \\ \end{bmatrix} \tag{5.1}$$

The A matrix represents the (3x3) angular acceleration coefficient matrix, which contains all of the terms associated with the angular accelerations. The B matrix on the right hand side of the equation, of size (3x1), contains all of the remaining terms from each of the three equations of motion. All terms in both the A and B matrices are known for each time step taken during the integration of the equations of motion. The equations of motion are solved for the angular accelerations during the integration using

$$\begin{bmatrix} \ddot{\Theta}_1 \\ \ddot{\Theta}_2 \\ \ddot{\Theta}_3 \end{bmatrix} = \begin{bmatrix} & & \\ & A^{-1} & \\ & & \end{bmatrix} \begin{bmatrix} \\ B \\ \\ \end{bmatrix} \tag{5.2}$$

Integration of the equations of motion for the forward dynamics simulations was performed using ODE45 (an integration routine that is built into MATLAB®) which is an adaptive step size integrator based on the explicit Runge-Kutta (45) formula, the Dormand-Prince pair [Shampine and Reichelt (1997)]. ODE45 is a one-step solver as it needs only the solution at the time step (t_{n-1}) immediately preceding the point (t_n) which is to be computed. Thus, before the integration process begins the initial angular positions and velocities of each of the hindlimb segments, in addition to the GRF's and the joint torques acting on the two-dimensional hindlimb model at $t = 0$ need to be specified.

For the forward dynamics simulations the two-dimensional hindlimb was modeled with the hip joint fixed at a single location, as it was for the inverse dynamics. The GRF's and joint torques were applied to the forward dynamics model based solely upon the progress of the forward dynamics simulation with respect to time, not position. Unlike the joint torques, which were continuously applied to the two-dimensional hindlimb model for the entire duration of the forward dynamics simulation, the GRF's were only applied between 0.23 s and 0.92 s. These two times correspond to the onset and end of the stance

phase respectively, as calculated from the two-dimensional GRF data.

During the integration ODE45 often chooses time steps that do not coincide with the fixed step-size of 10^{-3} s for the discrete joint torque and GRF data sets. For example, if ODE45 chose to perform an integration step at 0.3106 s no joint torque or GRF data would be available for that specific integration step. In this case joint torque and GRF data would be available on either side (0.310 s and 0.311 s) of the required integration step of 0.3106 s. To provide the proper joint torque and GRF data at the time steps required by the integrator, both the joint torques and GRF's were interpolated using a cubic spline function when required.

5.2 Failure of the Forward Dynamics Simulations

The initial forward dynamics simulations for the two-dimensional hindlimb model failed quite spectacularly. Figures 5.1(a), 5.1(b), and 5.1(c) show the original kinematic data used to calculate the two-dimensional joint torques, as well as the kinematic data predicted by the forward dynamics simulation. As shown in Figures 5.1(a) - 5.1(c) the kinematics predicted by the forward dynamics simulation begin to deviate away from the original joint angles almost immediately. The deviation of the predicted joint angles becomes quite drastic at 0.4 s when the tarsal segment of the hindlimb begins to spin in the counterclockwise direction (see Figure 5.1(c)). Shortly after both the thigh and shank segments begin to spin as well.

After trying numerous combinations of different step-sizes and error tolerances the forward dynamics simulations still failed. MATLAB®'*s* ODE23, which uses the explicit Runge-Kutta (23) of Bogacki and Shampine [Shampine and Reichelt (1997)] was tried to see if an alternative integrator might work, but it also failed in the same manner. After the failure of ODE45 and ODE23, which are both non-stiff integrators, it was thought that there may be some stiffness in the equations of motion. ODE15s, which is an integrator for stiff systems of equations based upon the numerical differentiation formulas (Shampine and Reichelt, 1997), was then tried but it also failed in a similar fashion.

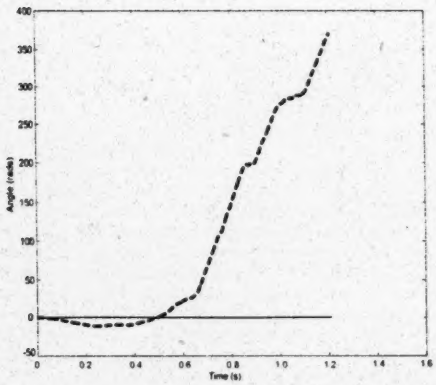

(a) Hip Angle

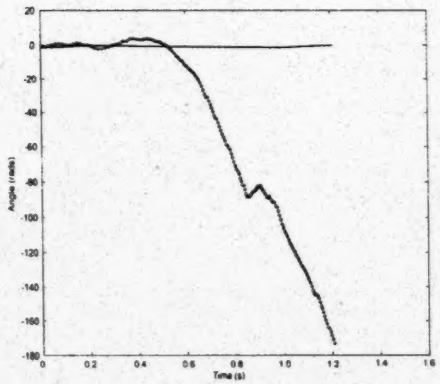

(b) Knee Angle

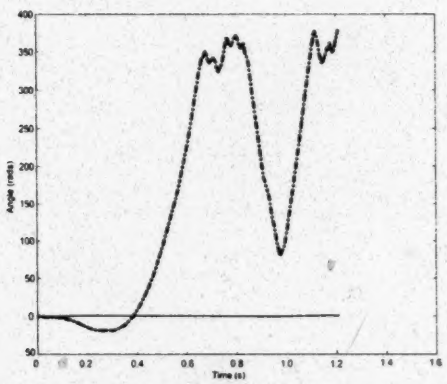

(c) Ankle Angle

Figure 5.1: Original kinematic data is shown with solid lines while the predicted kinematic data from the forward dynamics simulation is shown with dashed lines.

With the failure of the forward dynamics simulations for the two-dimensional hindlimb model a decision was made to investigate a simplified forward dynamics model in order to ascertain what was causing the simulations to fail.

5.2.1 Forward Dynamics Simulations for a Simple Pendulum

A single link pendulum was created by removing the shank and tarsal segments from the two-dimensional hindlimb model, as shown in Figure 5.2. The single

link pendulum then consisted of a uniform slender rod hanging from a fixed frictionless pin joint which was previously the hip joint of the two-dimensional hindlimb model.

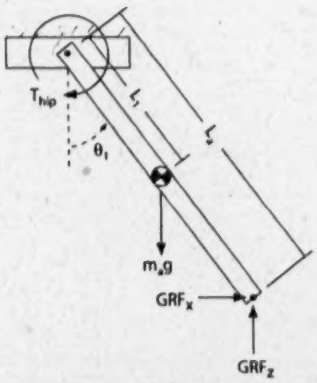

Figure 5.2: Single link pendulum created by removing the shank and tarsal segments from the two-dimensional hindlimb model. GRF_x, GRF_z, and T_{hip} are defined as positive in the directions shown, while Θ_1 is shown in the negative direction.

The segmental parameters of the single link pendulum remained unchanged from those of the thigh segment of the two-dimensional hindlimb model. All of the sign conventions for the joint angles, angular velocities, angular accelerations, and torques previously defined for the thigh segment of the two-dimensional hindlimb model also apply to the single link pendulum. The GRF's are also defined in the same was as for the two-dimensional hindlimb model, except that they were applied directly to the free end of the single link pendulum. The equation of motion for the single link pendulum is

$$T_{hip} = L_a\left(GRF_x \cos\Theta_1 - GRF_z \sin\Theta_1\right) + gL_1M_a \sin\Theta_1 + \ddot{\Theta}_1\left(I_a + M_aL_1^2\right). \quad (5.3)$$

The joint torque for the single link pendulum was calculated based upon the kinematic data for the hip joint and the two-dimensional GRF's. ODE45 was used as the integrator for the forward dynamics simulation. It was possible to correctly predict the kinematics for the first portion of the simulation, however at approximately 0.6 s the predicted kinematics diverged away from the true solution as shown in Figure 5.3.

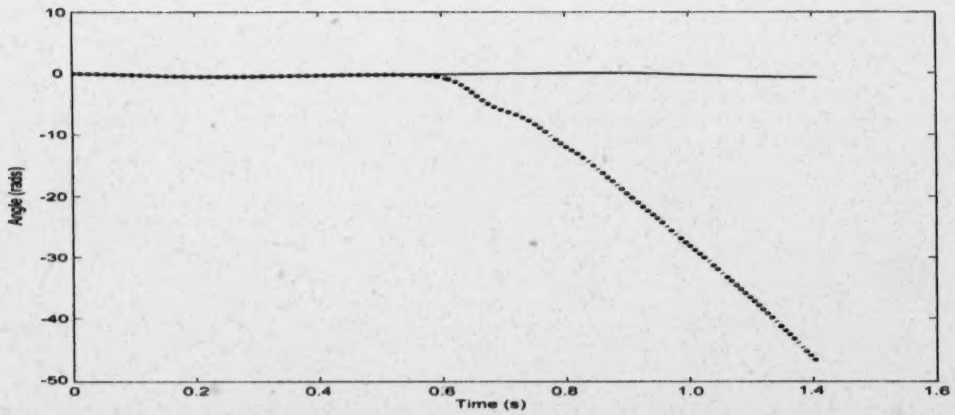

Figure 5.3: Original kinematic data (solid line) and the kinematic data predicted by the forward dynamics simulation (dotted line) for the single link pendulum.

Investigation into the failure of the forward dynamics simulation for the single link pendulum revealed that just prior 0.6 s, the predicted position of the pendulum began to drift away slightly ($< 2.29 \times 10^{-2}$ degrees) from its expected position. The joint torque being applied to the pendulum was no longer correct with respect to reproducing the original kinematics, since it was calculated with the original kinematics. Due to the mechanical nature of the two-dimensional pendulum model, as there was no control system present in the model, there was no way to modify the joint torques being applied to the pendulum to correct for the small deviations in the predicted position. Thus, as the forward dynamics simulation progressed the joint torques being applied to the pendulum amplified the deviations in the predicted position of the pendulum.

To further investigate the initial drift in the pendulum's position the forward dynamics simulation was simplified one step further by focussing only on a static case. For the static case investigations the joint torque was used to hold the pendulum at a fixed position while a single static force was applied to the free end of the pendulum in either the X or Z direction, as shown in Figures 5.4(a) and 5.4(b). The positions used for the static case investigation were 0 to 2π rads in $\frac{\pi}{6}$ increments. At each position a range of different static forced were applied from $GRF_{x,z} = -20$ N to $+20$ N in 5 N increments.

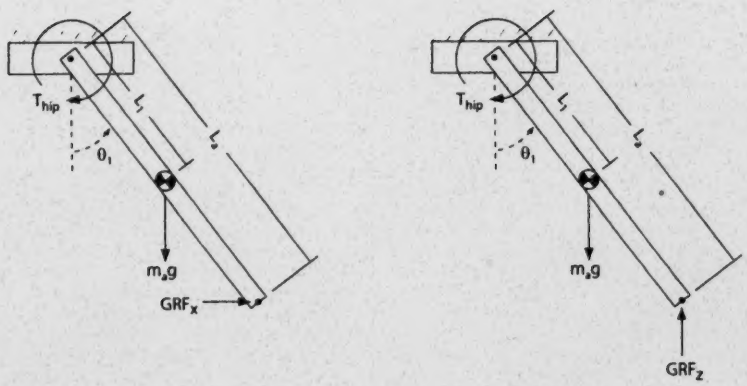

(a) (b)

Figure 5.4: Figures (a) and (b) show the forces applied to the free end of the pendulum for the static case investigation.

It was found that the stability of the forward dynamics simulations for the static cases, depended on whether or not a compressive or tensile force was applied to the pendulum. If a tensile force was applied to the pendulum, such as a negative GRFz at $\theta_1 = 0$, the forward dynamics simulation provided a static solution as expected. Here any drift in the calculated position of the pendulum, caused by round off error during the integration, was offset by the tensile force which acted to stabilize the simulation. However when a compressive force was applied to the pendulum, such as a positive GRFz at $\theta_1 = 0$, the forward dynamic simulation diverged. In this case the compressive force acts to destabilize the pendulum, causing any drift in the calculated position of the pendulum to be amplified. The time required for the forward dynamics simulation to become unstable was decreased by increasing the magnitude of the compressive force applied to the pendulum.

For the non-static forward dynamics simulation the GRF's create compressive forces which acts on the free end of the single link pendulum, over the duration of the stance phase. The compressive forces created by the GRF's destabilize the forward dynamics simulation causing the simulations to fail. Similarly for the two-dimensional hindlimb model the GRF's also apply compressive forces over the duration of the stance phase. However, compared to

the single link pendulum model, the two-dimensional hindlimb model is more sensitive to the destabilizing effect of the compressive forces. Any variation in the predicted kinematics from the expected kinematics, will cause the joint torques being applied during the forward dynamics simulation to be incorrect. Therefore without some sort of control mechanism in place to account for the drift in the position of the pendulum, or each of the hindlimb segments for the two-dimensional hindlimb model, the forward dynamics will not provide a successful simulation.

5.3 Torsional Springs and Dampers

In an effort to overcome the destabilizing effect of the GRF's on the forward dynamics simulations the addition of linear torsional spring-damper pairs, analogous to the linear spring-damper pair shown in Figure 5.5, was investigated. The limbs of animals (including humans) have been shown to display spring like behavior. Alexander (1985) proposed that animal's limbs employ spring like qualities as a means of minimizing energy expenditure during running gaits. Human legs have also been modeled as springs during running where the stance limb is modelled as single linear spring with a point mass that is equivalent to the body mass [Ferris et al. (1998)]. More complex limb models utilizing both one dimensional springs and dampers [Nigg and Liu (1999)] as well as torsional springs [Farley et al. (1998)] and torsional spring-damper pairs [Rapoport et al. (2003)] have also been used to investigate the effects of limb stiffness characteristics in humans. The muscles and tendons of the limbs do not behave as simple springs since they exhibit viscoelastic properties as they can store, dissipate, and return energy [Zajac (2002)]. Thus, it is appropriate to include viscoelastic properties in the hindlimb model.

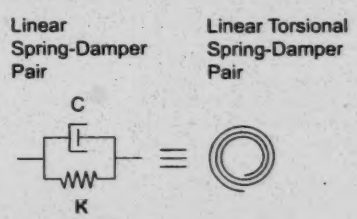

Figure 5.5: Torsional spring-damper pair representation. The torsional spring and torsional damper are in parallel with one another, similar to the linear spring damper pair.

Adding a linear torsional spring-damper pair to the forward dynamics models is a simple way of accounting for the small amount of error which propagates during the forward dynamics simulations. A linear torsional spring-damper pair was added to the pendulum model as shown in Figure 5.6. The torsional spring was defined such that it would not apply any torque when $\Theta_1 = 0$. A positive (or negative) angular displacement and angular velocity then results in a negative (or positive) torque being supplied by both the torsional spring and torsional damper. The addition of the linear torsional spring-damper pair to the single link pendulum model corrected for any drift in the predicted position of the pendulum by automatically supplying a corrective torque. With the addition of the torsional spring-damper pair to the pendulum model the joint torques estimated by the inverse dynamics model were altered. For the sake of clarity the torques created by the torsional springs and dampers will be referred to as passive joint torques. The joint torques estimated without the torsional springs and dampers will be referred to as the anatomic joint torques and the combination of both the passive and anatomic joint torques will then be referred to as the total joint torques.

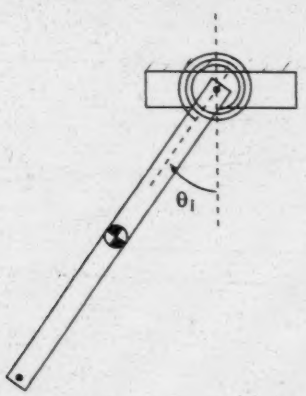

Figure 5.6: Single link pendulum with the addition of the torsional spring-damper pair.

The stiffness coefficient (K) and damping coefficient (C) for the torsional spring-damper pair were found by running the forward dynamics simulation repeatedly. A kinematic accuracy requirement of $\pm 1°$ (± 0.0175 rads) was used to evaluate whether or not the forward dynamics simulations were successful. If at any point, one of the joint angles predicted by the forward dynamics simulation differed by more than $\pm 1°$ from the original joint angle data (see Chapter 2, Figure 2.5), the simulation was deemed a failure. Each time the

simulation was run either K or C was varied so that a combination of the smallest K and C values could be found, while still allowing the kinematic data predicted by the forward dynamics simulation to meet the kinematic accuracy requirement. By finding the combination of the smallest values for K and C, the passive joint torque which they create would be minimized, thereby decreasing the effect of the passive torque on the total joint torque. The values which were found for the pendulum were $K = 0.09 \frac{\text{Nm}}{\text{rad}}$, $C = 0.032 \frac{\text{Nm·s}}{\text{rad}}$. The anatomic joint torque and the total joint torque profiles for the pendulum are shown in Figure 5.7.

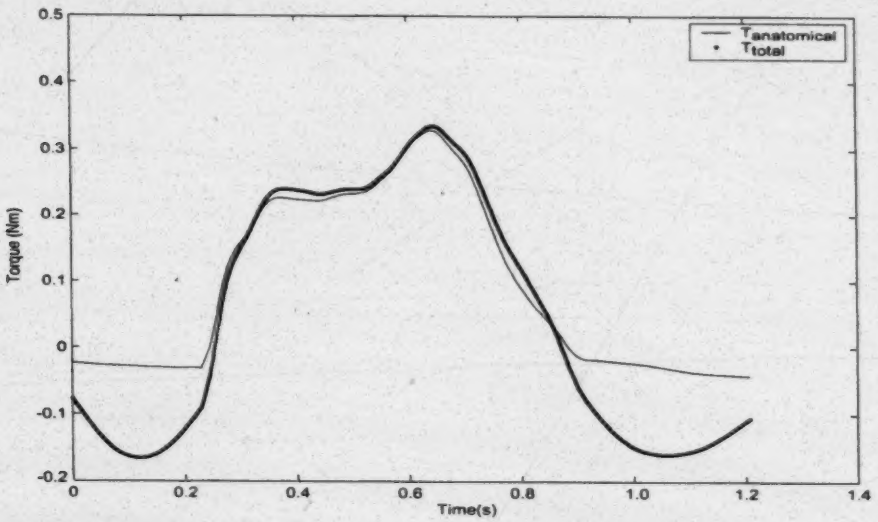

Figure 5.7: Anatomic and total joint torques for the pendulum model.

The passive torques supplied by the torsional spring-damper pair as calculated from the inverse dynamics, and the passive torques used during the forward dynamics simulation for the pendulum, are shown in Figure 5.8. To illustrate the corrective torque supplied by the torsional spring-damper pair during the forward dynamics simulation, a portion of Figure 5.8 has been blown up and is shown in Figure 5.9. The small difference between the two torques shown in Figure 5.9, beginning just prior to 0.6 s, represents the corrective torque required to stabilize the forward dynamic simulation.

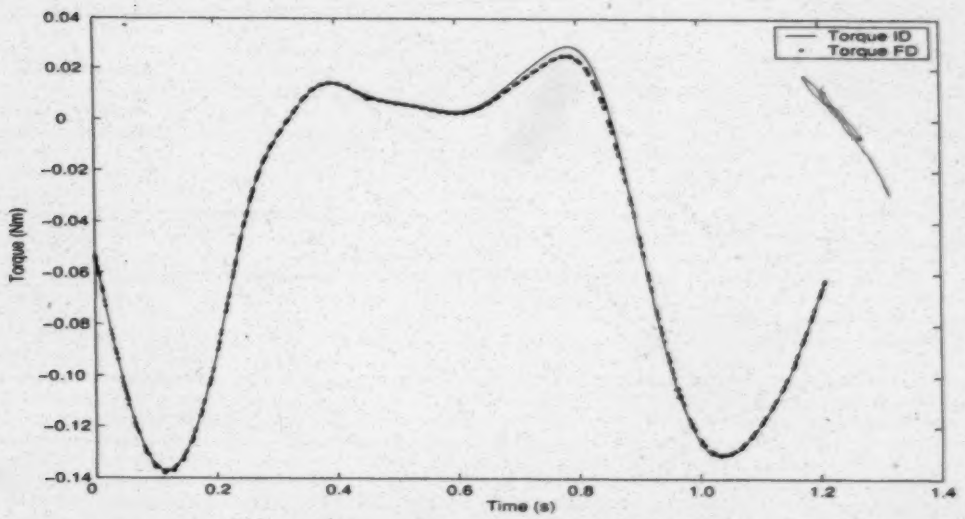

Figure 5.8: Passive torques supplied during the inverse dynamics (Torque ID) and during the forward dynamics simulation (Torque FD). $K = 0.09 \frac{\text{Nm}}{\text{rad}}$, $C = 0.032 \frac{\text{Nm·s}}{\text{rad}}$.

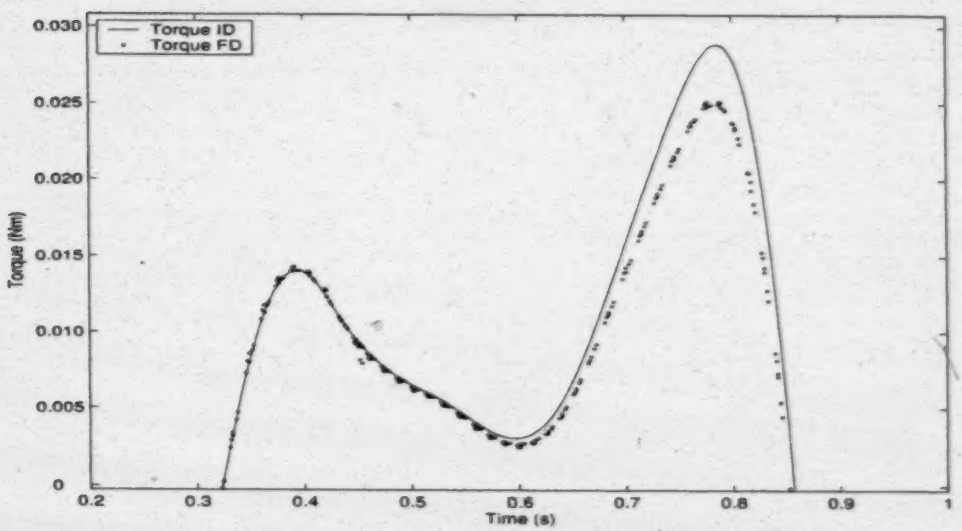

Figure 5.9: Magnification of Figure 5.8 to highlight the corrective torque supplied by the spring-damper pair during the forward dynamics simulation.

5.3.1 Implementation of Torsional Springs and Dampers

Similar to the single link pendulum, linear torsional spring-damper pairs were added to each one of the three joints of the two-dimensional hindlimb model as shown in Figure 5.10. While the spring-damper pair added to the hip joint is implemented into the two-dimensional hindlimb model in exactly the same way as for the pendulum model, the spring-damper pairs added to the knee and ankle joints were defined differently. For the knee and ankle joints, the torques supplied by the spring-damper pairs depend on the relative angles (Φ_1 and Φ_2) and the relative angular velocities ($\dot{\Phi}_1$ and $\dot{\Phi}_2$) between the thigh and shank, and the shank and tarsals. Φ_1 and Φ_2 are also shown in Figure 5.10.

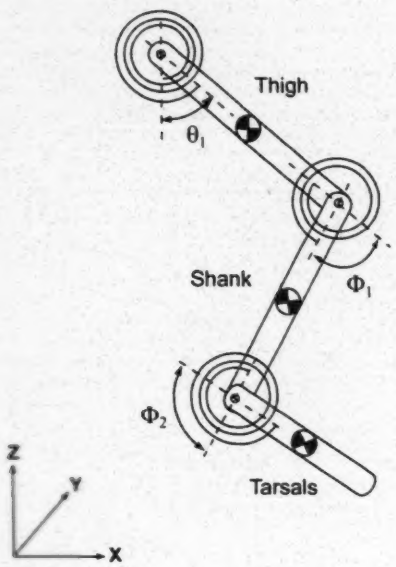

Figure 5.10: Two-dimensional hindlimb model with the addition of the linear torsional spring-damper pairs, represented by the spirals.

Φ_1, Φ_2, $\dot{\Phi}_1$, and $\dot{\Phi}_2$ are related to the kinematic data as shown in Equations (5.4) to (5.7).

$$\Phi_1 = \Theta_2 - \Theta_1 \tag{5.4}$$

$$\Phi_2 = \Theta_3 - \Theta_2 \tag{5.5}$$

$$\dot{\Phi}_1 = \dot{\Theta}_2 - \dot{\Theta}_1 \tag{5.6}$$

$$\dot{\Phi}_2 = \dot{\Theta}_3 - \dot{\Theta}_2 \tag{5.7}$$

The addition of the torsional spring-damper pairs to the two-dimensional hindlimb model added a spring stiffness term and a damping term (highlighted with an underbrace) to each of the equations of motion for the two-dimensional hindlimb model, as shown in Equations (5.8) to (5.10). The total joint torques are represented by T_{hip}, T_{knee}, and T_{ankle} in Equations (5.8) to (5.10). The passive joint torques are represented by the stiffness and damping terms that have been under-braced on the right hand side of Equations (5.8) to (5.10). The anatomic joint torques are then represented by all of the remaining terms on the right hand side of Equations (5.8) to (5.10). All of the torsional springs implemented into the two-dimensional hindlimb model had identical stiffnesses, K, and shared the same damping coefficient, C.

$$\begin{aligned} T_{hip} \;=\; & T_{knee} + L_a\left(GRF_x\cos\Theta_1 - GRF_z\sin\Theta_1\right) + g\left(L_1M_a + L_aM_b + L_aM_c\right)\sin\Theta_1 \\ & + L_a\left(L_2M_b + L_bM_c\right)\sin(\Theta_1-\Theta_2)\dot{\Theta}_2^2 + L_3L_aM_c\sin(\Theta_1-\Theta_3)\dot{\Theta}_3^2 \\ & + \left(I_a + M_aL_1^2 + M_bL_a^2 + M_cL_a^2\right)\ddot{\Theta}_1 + L_a\left(L_2M_b + L_bM_c\right)\cos(\Theta_1-\Theta_2)\ddot{\Theta}_2 \\ & + L_3L_aM_c\cos(\Theta_1-\Theta_3)\ddot{\Theta}_3 \underbrace{+K\Theta_1 + C\dot{\Theta}_1} \end{aligned} \tag{5.8}$$

$$\begin{aligned} T_{knee} \;=\; & T_{ankle} + L_b\left(GRF_x\cos\Theta_2 - GRF_z\sin\Theta_2\right) + g\left(L_2M_b + L_bM_c\right)\sin\Theta_2 \\ & - L_a\left(L_2M_b + L_bM_c\right)\sin(\Theta_1-\Theta_2)\dot{\Theta}_1^2 + L_3L_bM_c\sin(\Theta_2-\Theta_3)\dot{\Theta}_3^2 \\ & + L_a\left(L_2M_b + L_bM_c\right)\cos(\Theta_1-\Theta_2)\ddot{\Theta}_1 + \left(I_b + M_bL_2^2 + M_cL_b^2\right)\ddot{\Theta}_2 \\ & + L_3L_bM_c\cos(\Theta_2-\Theta_3)\ddot{\Theta}_3 \underbrace{+K\Phi_1 + C\dot{\Phi}_1} \end{aligned} \tag{5.9}$$

$$
\begin{aligned}
T_{ankle} \;=\; & L_c\left(GRF_x\cos\Theta_3 - GRF_z\sin\Theta_3\right) - L_3L_aM_c\sin(\Theta_1-\Theta_3)\dot{\Theta}_1^2 \\
& -L_3L_bM_c\sin(\Theta_2-\Theta_3)\dot{\Theta}_2^2 + gL_3M_c\sin\Theta_3 + \left(I_c+M_cL_3^2\right)\ddot{\Theta}_3 \\
& +L_3L_bM_c\cos(\Theta_2-\Theta_3)\ddot{\Theta}_2 + L_3L_aM_c\cos(\Theta_1-\Theta_3)\ddot{\Theta}_1 \underbrace{+K\Phi_2 + C\dot{\Phi}_2}
\end{aligned}
\tag{5.10}
$$

The implementation of the linear torsional spring-damper pairs into the two-dimensional hindlimb model was somewhat artificial in the sense that they did not account for any anatomical properties of the hindlimb, but were instead used as a means of stabilizing the forward dynamics simulation. However as mentioned at the beginning of this section the limbs, and the muscles and tendons which actuate them, display spring and damper like behavior. Therefore viscoelastic properties should also be included in the hindlimb model.

There has been very little research regarding the torsional stiffness and torsional damping properties of feline hindlimb joints. Yasuda et al. (1986) measured the passive torsional stiffness and damping coefficients for a feline knee about the X-axis direction for valgus loading of the knee. Valgus loading occurs when a force is applied laterally to the limb, which would occur if a force was applied in the Y-axis direction to the hindlimb. The torsional stiffness and damping coefficients could be approximated by modeling the stiffness and damping properties for hindlimb muscles and tendons, but this would involve the development of models for each of the muscles and tendons of the limb, and their distribution on the hindlimb model. The work involved in such an endeavor would go beyond the scope of the current study.

The range of K and C values that would allow the forward dynamics simulation to meet the kinematic accuracy requirement is quite large. However large values for K ($> 1\frac{\text{Nm}}{\text{rad}}$) and C ($> 1\frac{\text{Nm·s}}{\text{rad}}$) create passive joint torques which are far larger than the anatomic joint torques. When observing the total joint torques, the anatomic joint torques are then buried underneath the much larger passive joint torques. Therefore the combination of K and C values which introduced the smallest passive joint torques, was chosen. Thus the effect of adding the torsional spring-damper pairs was minimized with respect to the total joint torques. The kinematic accuracy requirement of $\pm 1°$ or ± 0.0175 rads used for the pendulum model was again used to evaluate whether or not the forward dynamics simulations for the hindlimb model were successful. The stiffness and damping coefficients for the torsional springs and

dampers of the two-dimensional hindlimb model were found in a similar fashion as the stiffness and damping coefficients for the single link pendulum.

The combination of $K = 0.04\frac{\text{Nm}}{\text{rad}}$ and $C = 0.042\frac{\text{Nm·s}}{\text{rad}}$ introduced the smallest passive torques, while allowing the forward dynamics simulation to meet the kinematic accuracy requirement, for the chosen segmental parameters of the hindlimb model. The passive joint torques introduced by the spring-damper pair at the hip, knee, and ankle joints are shown in Figure 5.11. The torsional dampers are the dominant contributors to the passive joint torques shown in Figure 5.11, which is caused by the much larger angular velocities of the hindlimb segments, when compared to the angular displacements.

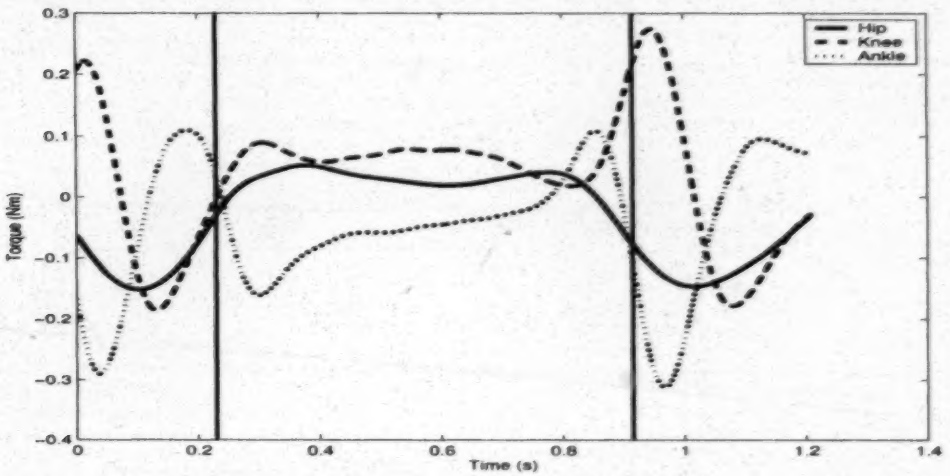

Figure 5.11: Passive Joint Torques created by the spring-damper pairs ($K = 0.04\ \frac{\text{Nm}}{\text{rad}}$, $C = 0.042\frac{\text{Nm·s}}{\text{rad}}$). The vertical lines ($t = 0.23$ s and $t = 0.92$ s) represent the transitions between the swing and stance phases.

5.3.2 Joint Torques with Torsional Spring-Damper Pairs

The total joint torques estimated with the torsional spring-damper pairs are shown in Figure 5.12. For comparison purposes the anatomic joint torques are shown in Figure 5.13. As shown in Figure 5.12 the addition of the spring-damper pairs affects the total joint torques the most during the swing phases. Here the much smaller anatomic joint torques become hidden beneath the larger passive torques created by the spring-damper pairs. During the stance

phase the total joint torques are affected the most near the transitions between the swing and stance phases. The magnitudes of all three total joint torques are also slightly decreased during the stance phase, when compared to the anatomic joint torques shown in Figure 5.13.

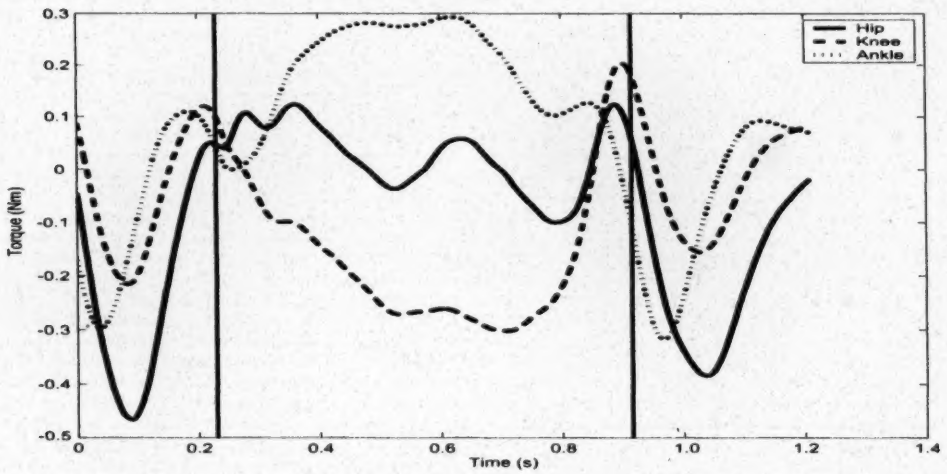

Figure 5.12: Total Joint Torques ($K = 0.04\ \frac{\text{Nm}}{\text{rad}}$, $C = 0.042\ \frac{\text{Nm·s}}{\text{rad}}$).

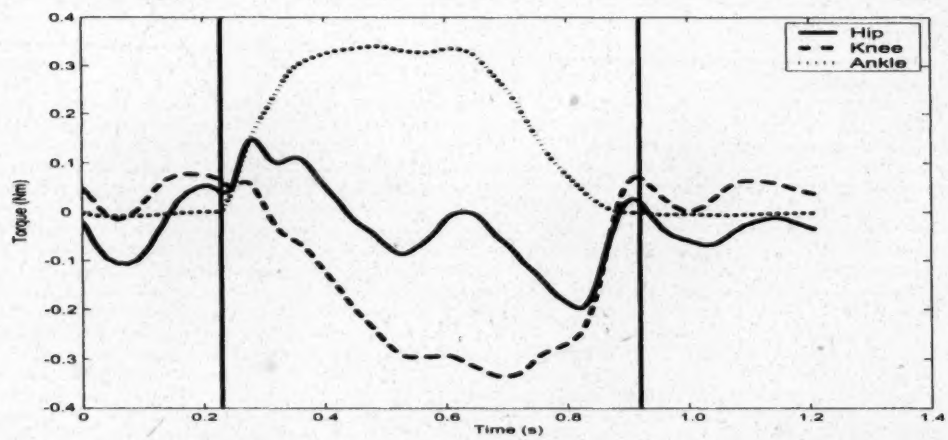

Figure 5.13: Anatomic joint torques. The vertical lines represent the transitions between the swing and stance phases ($t = 0.23$ s and $t = 0.92$ s).

5.4 Concluding Remarks

The initial failure of the forward dynamics simulation for the two-dimensional hindlimb model demonstrated the need for some type of control to be integrated in to the model to account for the sensitivity of the forward dynamics simulation to slight variances in the predicted positions of the hindlimb segments, and the destabilizing effect of the GRF's. The addition of the linear torsional spring-damper pairs were shown to stabilize the forward dynamics simulations. Although the torsional spring-damper pairs may be somewhat artificial at this stage of development, their inclusion provides a means of modeling the viscoelastic properties of the soft-tissues in the hindlimb, which will need to be addressed in future work if quantitative information is required.

Chapter 6

Conclusions and Future Work

6.1 Conclusions

The study of feline hindlimb modeling has allowed for a number of conclusions to be drawn about the modeling process:

Care should be taken when obtaining the segmental lengths of the hindlimb. This will ensure that the triangulation technique can be used to calculate the position of the knee joint for the kinematic data. It will also allow for the most accurate estimation of the segmental parameters for the hindlimb model calculated from Hoy and Zernicke (1985).

The use of uniform slender rods to model the geometry of the thigh, shank, and tarsal segments was demonstrated to be an acceptable approximation for the hindlimb studied, provided that the masses of the individual segments were predicted using the empirical equations developed by Hoy and Zernicke (1985).

The contributions to the estimated joint torques made by the dynamic joint torques should not be ignored since they can have a significant effect on the estimated joint torques near the transitions between the swing phases and stance phases.

Variations in the center of mass locations and the masses of the hindlimb model can also have a significant effect on the estimated joint torques. Of the segmental parameters investigated the center of mass location of the shank, L_2, had the greatest influence on the estimated hip and knee joint torques. Most of the differences in the estimated joint torques were caused during the

swing phases, due to the faster motion of the limb during swing phase than the stance phase.

The addition of a rigid body paw to the two-dimensional hindlimb model had a very significant effect on the estimated joint torques during the stance phase. Much greater, in fact, than any of the investigated variations in the segmental hindlimb parameters. From the rigid paw investigation it can be extrapolated that the addition of a paw model to the two-dimensional hindlimb model will result in an increase in the magnitudes of the estimated hip and ankle torques, and a decrease in the magnitude of the estimated knee torque.

During a typical walking gait the cat hindlimb does not move in a simple planar fashion. However this study has shown that a planar model will provide an accurate estimate of the joint torques occurring within the limb. Should three-dimensional joint torques be estimated at each joint, this finding would no longer hold true. The addition of GRFy, which pushes laterally on the paw creating a valgus load on the limb during the stance phase, will cause a significant increase in the joint torques acting about the X-axis (adduction / abduction) at each joint.

A successful forward dynamics simulation, run using the estimated joint torques and the measured GRF's as inputs, was not achieved without some means of accounting for the instability caused by the GRF's. The forward dynamics model required the addition of linear torsional spring-damper pairs at each joint to stabilize the forward dynamics simulations. The linear torsional spring-damper pairs also provide a means of incorporating the viscoelastic properties of the soft tissues (muscles and tendons) in the hindlimb, in the absence of soft tissue models in the two-dimensional hindlimb.

6.2 Future Work

Recommendations for future research into the modeling of the feline hindlimb include are broken into two categories: inverse dynamics and forward dynamics.

Inverse Dynamics

To the author's knowledge no studies have performed a three-dimensional inverse dynamics investigation into the feline hindlimb. Muscles at the hip

and MTP joints stabilize the hindlimb during gait about the adduction and abduction axis. The estimated joint torques may provide an additional insight into the cat's locomotor control system.

If the forces and moments which occur within the paw itself are to be estimated, the kinematic data for the phalanges or a method of modeling the motion of the phalanges will be required. Collection of kinematic data for the phalanges will require a refinement in the video based kinematic data collection process, or require the development of an alternative method for measuring the kinematic data of the phalanges. Additionally the transfer of the GRF's from the soft tissues on the underside of the paw, to the phalanges, will be needed.

Forward Dynamics

For forward dynamics investigations the flexibility and compliance of the paw will need to be addressed. The movement of the MTP joint and the subsequent movement of the area of contact over the surface of the paw are two factors that should be addressed by a paw model. The compliance of the paw due to the deformation of the soft tissues in the paw during contact, should also be considered. Alexander (1990) stated that some sort of padding is needed to avoid excessive impact forces when the hindlimb makes contact with a surface.

The creation of a ground contact model could be investigated. A ground contact model removes the two-dimensional hindlimb model's reliance on the application of the measured GRF's during the forward dynamics simulations. This is an important step towards creating a forward dynamics model which can propel itself, thereby creating locomotion. The ground contact model should be developed with the inverse dynamics model, since the motion of the inverse dynamics model is fixed (due to the kinematic data), such that it will provide GRF's that match the measured GRF's.

References

R.M. Alexander. *Elastic mechanisms in animal movement.* McGraw-Hill, 1985.

R.M. Alexander. Three uses for springs in legged locomotion. *International Journal of Robotics Research*, 9(2):53–61, 1990.

M. Bobbert, M. Yeadon, and B. Nigg. Mechanical analysis of the landing phase in heel-toe running. *Journal of Biomechanics*, 25(3):223–234, 1992.

O. Bruneau and FB. Ouezdou. Distributed ground/walking robot interaction. *Robotica*, 17:313–323, 1999.

J.A. Buford and J.L. Smith. Adaptive control for backward quadrupedal walking. II. hindlimb muscle synergies. *Journal of Neurophysiology*, 64:756–756, 1990.

J.A. Buford, R.F. Zernicke, and J.L. Smith. Adaptive control for backward quadrupedal walking. I. posture and hindlimb kinematics. *Journal of Neurophysiology*, 64:745–755, 1990.

A. Cappozzo. Gait analysis methodology. *Human Movement Science*, 3:27–50, 1984.

P. Carlson-Kuhta, T. Trank, and Smith J. Forms of forward quadrupedal locomtion. II. a comparison of posture, hindlimb kinematics, and motor patterns for upslope and level walking. *Journal of Neurophysiology*, 79(4): 1687–1701, 1998.

J. Duysens, H.W.A.A. Van de Crommet, B.C.M. Smits-Engelsman, and F.C.T. Van der Halem. A walking robot called human: lessons to be learned from neural control of locomtion. *Journal of Biomechanics*, 35(4):447–453, 2002.

O. Ekeberg and K.G. Pearson. Computer simulation of stepping in the hind legs of the cat: an examination of mechanisms regulating the stance-to-swing transition. *Journal of Neurophysiology*, 94:4256–4268, 2005.

C. Farley, H. Houdijk, C. Van Strien, and M. Louie. Mechanism of leg stiffness adjustment for hopping on surfaces of different stiffnesses. *Journal of Applied Physiology*, 85(3):1044–1055, 1998.

D. Ferris, M. Louie, and C. Farley. Running in the real world: adjusting leg stifness for different surfaces. *Proceedings of the Royal Society of London Series B*, 265:989–994, 1998.

E.G. Fowler, R.J. Gregor, J.A. Hodgson, and R.R. Roy. Relationship between ankle muscle and joint kinetics during the stance phase of locomotion in the cat. *Journal of Biomechanics*, 26:465–483, 1993.

M. Gasson, B. Hutt, I. Goodhew, P. Kyberd, and K. Warwick. Invasive neural prosthesis for neural signal detection and nerve stimulation. *International Journal of Adaptive Control and Signal Processing*, 19(5):365–375, 2005.

G.E. Goslow, R.M. Reinking, and D.G. Stuart. The cat step cycle: hind limb joint angles and muscle lengths during unrestrained locomotion. *Journal of Morphology*, 141:1–42, 1973.

H.M. Herr and T.A. McMahon. A trotting horse model. *International Journal of Robotics Research*, 19(6):556–581, 2000.

M. Hoy and R. Zernicke. Modulation of limb dynamics in the swing phase of locomotion. *Journal of Biomechanics*, 18(1):49–60, 1985.

M. Hoy and R. Zernicke. The role of intersegmental dynamics during rapid limb oscillations. *Journal of Biomechanics*, 19:866–877, 1986.

H. Huber and M. Dutoit. Dynamic foot-pressure measurement in the assessment of operatively treated clubfeet. *Journal of Bone and Joint Surgery*, 86A(6):1203–1210, 2004.

T.R. Kane and D.A. Levinson. *Dynamics: Theory and Applications*. Cambridge University Press, 1988.

J.P. Kuhtz-Buschbeck, R. Poppele, M. Illert, and C. Weinhardt. X-ray study of the cat hindlimb during treadmill locomotion. *European Journal of Neuroscience*, 6:1187–1198, 1994.

K. Mabuchi and H. Fujie. Use of robotics technology to measure friction in animal joints. *Clinical Biomechanics*, 11(2):121–125, 1996.

J.T. Manter. The dynamics of quadrupedal walking. *Journal of Experimental Biology*, 15:522–540, 1938.

B.J. McFayden, S. Lavoie, and T. Drew. Kinetic and energetic patterns for hindlimb obstacle avoidance during cat locomotion. *Experimental Brain research*, 125:502–510, 1999.

S. Miller, J. Van Der Burg, and F.G.A. Van Der Meche. Coordination of movements of the hindlimb and forelimbs in different forms of locomotion in normal and decerebrate cats. *Brain Research*, 91(2):217–237, 1975.

P. Neveu, J. Villanova, and J.P. Gasc. Modelisation of an unspecified quadruped walking mammal. *Comparative Biochemistry and Physiology Part A*, 131:135–144, 2001.

B. Nigg and W. Liu. The effect of muscle stiffness and damping on simulated impact force peaks during running. *Journal of Biomechanics*, 32:849–856, 1999.

K.L. Perell, R.J. Gregor, J.A. Buford, and J.L. Smith. Adaptive control for backward quadrupedal walking. IV. hindlimb kinetics during stance and swing. *Journal of Neurophysiology*, 70(6):2226–2240, 1993.

S. Rapoport, J. Mizrahi, E. Kimmel, O. Verbitsky, and E. Isakov. Constant and variable stiffness and damping of the leg joints in human hopping. *Journal of Biomechanical Engineering*, 125:507–514, 2003.

J.P. Schmiedeler and K.J. Waldron. The mechanics of quadrupedal galloping and the future of legged vehicles. *International Journal of Robotics Research*, 18(12):1224–1234, 1999.

L.F. Shampine and M.W. Reichelt. The matlab ode suite. *SIAM Journal on Scientific Computing*, 18(1):1–22, 1997.

C.E. Shannon. Communication in the presence of noise. *Proceedings of the Institute of Radio Engineers*, 37:10–21, 1949.

L. Shen and R. Poppele. Kinematic analysis of cat hindlimb stepping. *Journal of Neurophysiology*, 74(6):2266–2280, 1995.

D.H. Sutherland. The evolution of clinical gait analysis part I: kinesiological emg. *Gait and Posture*, 14(1):61–70, 2001.

T.V. Trank and J.L. Smith. Adaptive control for backward quadrupedal walking VI. metatarsophalangeal joint dynamics and motor patterns of digit muscles. *Journal of Neurophysiology*, 75(2):678–694, 1996.

A.J. Van Den Bogert, H.C. Schamhardt, and A. Crowe. Simulation of quadrupedal locomotion using a rigid body model. *Journal of Biomechanics*, 22(1):33–41, 1989.

D.A. Winter. *Biomechanics of Human Movement.* John Wiley and Sons, 1979.

G. Wu and J. Hitt. Ground contact characteristics of tai chi gait. *Gait and Posture*, 22(1):32–39, 2004.

K. Yasuda, T. Sasaki, and M. Kato. An experimental study on in vivo dynamic mechanical properties of the knees of cats in valgus loading. *Journal of Biomechanics*, 19(6):413–424, 1986.

F.E. Zajac. Understanding muscle coordination of the human leg with dynamical simulations. *Journal of Biomechanics*, 35:1011–1018, 2002.

Appendix A

Motion Capture System Calibration

A quick test of the motion capture system used by Dr. Pearson for the collection of the positional data was performed to investigate if there was any error made in the measurements of the kinematic data.

Four reflective markers were placed upon a calibration board in a rectangular configuration as shown in Figure A.1. The calibration board was then placed in the middle of the walkway. A calibration of the motion capture system was performed by recording a single frame of the stationary calibration board. For the calibration, the operator running the motion capture system manually chooses the location of each of the corners of the calibration board captured in the single frame using the Peak Motus program. The physical dimensions of the calibration board are then entered into the Peak Motus program. Since the motion capture system uses digitized video, pixels are used to measure distances. The calibration lets the Peak Motus software know what distance value to assign each pixel so that the program can correctly calculate the positions of the reflective markers.

The stationary calibration board was then recorded for 0.5 s at 60 Hz. The film was digitized and the position of the four reflective markers were then calculated relative to the bottom left hand corner of the calibration board by the Peak Motus program, creating a positional data set. The locations of the center of each of the four reflective markers were then manually measured using a ruler with a resolution of 0.5 mm, also with respect to the bottom left hand corner of the calibration board for comparison purposes.

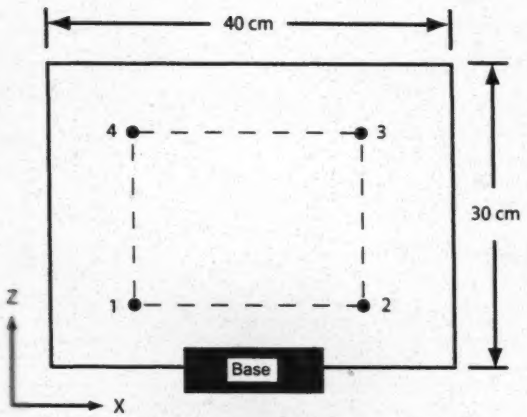

Figure A.1: Calibration board used for the calibration of the motion capture system. Reflective markers were placed at points 1 through 4, in a rectangular configuration.

Upon analysis of the positional data set for the four reflective markers, a small amount of fluctuation was observed in the calculated values of each of the X and Z coordinates of the four reflective markers. The X coordinate data calculated by the motion capture system for Point 1 is shown in Figure A.2. A maximum fluctuation of 0.3 mm's can be observed in Figure A.2. The fluctuation in the calculated value of the X coordinate may be attributed to the tracking of the reflective markers, where the tracking process refers to the identification of the location of each of the reflective markers in each frame of the digitized video. The majority of the tracking process is automated by the Peak Motus software, where the software chooses the location of the reflective markers in each frame of the digitized video based on the contrast between the intensity of the light given off by the reflective markers relative to their background. Any variations in the intensity of the light given off by the reflective markers, from frame to frame of the digitized video, may affect the calculation of the location of the center of the reflective marker. Of the four markers, the maximum observed fluctuation in the X and Z coordinates was 1.0 mm in the Z coordinate of the reflective marker located at point four.

Each of the X and Z coordinate data sets calculated by the motion capture system were averaged to find a mean X coordinate and Z coordinate for each

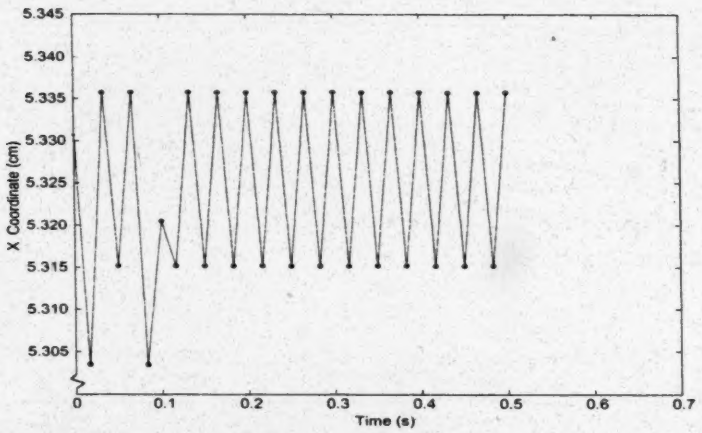

Figure A.2: Plot of the calculated X-Coordinate position of the reflective marker at Point 1 from the motion capture system.

of the four reflective markers. The measured locations of reference points 1 through 4 were then compared to the mean X and Z coordinates. The maximum error found in the motion capture system's calculation of the coordinates of the four reflective markers was 2.1 mm's.

Factors Affecting Measurements

For the purpose of this study an error of 2.1 mm's in the location measurements of the reflective markers provide an adequate estimation of the markers locations, since as mentioned in Chapter 2 Section 2.1.1 skin slippage is a far greater source of error in the measurements. There are, however, a few other factors which may affect the accuracy of the measurement of the reflective markers.

The two-dimensional kinematic data provided by Dr. Pearson was collected with a single camera. Therefore any motion of the hindlimb which occurs outside of the two-dimensional plane of the camera (which is the X-Z plane of the global reference frame) will not be accounted for. However for the case of a cat walking along an enclosed walkway, the errors which may occur due to the use of the single camera are fairly small. As mentioned in Chapter 2, Section 2.2.1 the largest out of plane motion occurs when the hip joint abducts during the swing phase. The largest observed abduction angle from the hip adduction and abduction data provided by Dr. Misiaszek was 10 degrees.

Assuming a total limb length of 25 cm's, the maximum error caused by the maximum observed hip abduction of 10 degrees would be 3.8 mm's in the Z direction for the paw marker, see Figure A.3. Any error due to the use of the single camera is still far less than the error attributed to the skin slippage, which may be as large as 4 cm's.

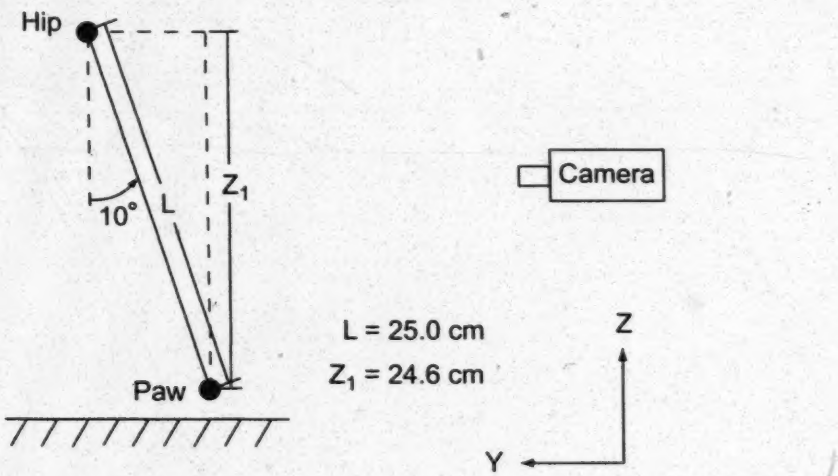

Figure A.3: Error in the measurement of the limb caused by two-dimensional data collection. L is the total length of the limb, while Z_1 would be the distance between the hip and paw markers as measured by the motion capture system.

The placement of the camera with respect to the distance that it is located from the walkway, and therefore the cat, will also affect the accuracy of the measurements. If the camera is not placed the same distance from the walkway for each trial, the accuracy of the system may vary for each gait trial since the pixels will then have a different distance value assigned to them for each trial.

Appendix B

Autolev Code

This appendix contains the code used by Autolev to generate Kane's equations of motion for the two-dimensional hindlimb model, and the three-dimensional hindlimb model. The code is saved as a text editor file which is then accessed and run by Autolev. The Autolev code for the three-dimensional hindlimb model also generates a set of equations with which the reaction forces which act upon the hip can be solved.

B.1 Two-Dimensional Hindlimb Model Code

```
%*********************************************************************
%     File:    2D_ID_3Link ( Setup for Autloev 3.4)
%     Problem: Analysis of 3 link leg with 3 torques and 2 GRF's
%*********************************************************************
%---------------------------------------------------------------------
%       Newtonian, bodies, frames, particles, points
%---------------------------------------------------------------------
degrees      off   % angles expressed in radians
Newtonian    N     % Newtonian reference frame
Bodies       A,B,C
Points       E,F,H,I
%---------------------------------------------------------------------
%       Variables, constants, specified, mass, inertia
%---------------------------------------------------------------------
VARIABLES   Q{3}''     % Angles + derivatives
VARIABLES   U{3}'      % Generalized Speeds and their derivatives
```

```
VARIABLES   GRFx,GRFy % Ground reaction Forces
VARIABLES   T1,T2,T3  % Torques
Constants   L1,L2,L3  % Distance centers of mass for links A,B,C
Constants   LA,LB,LC  % Lengths of Body A,B,C
Constants   G         % gravity
MASS        A = MA, B = MB, C = MC % Masses of bodies A,B,C,D
%  Model the limbs as slender rods
Inertia      A, IGA, IGA, 0 % inertia properties for body A
Inertia      B, IGB, IGB, 0 % inertia properties for body B
Inertia      C, IGC, IGC, 0 % inertia properties for body C
%-------------------------------------------------------------------
%       Geometry relating unit vectors
%-------------------------------------------------------------------
dircos(N,A,SPACE213,Q1,0,0)
dircos(N,B,space213,Q2,0,0)
dircos(N,C,space213,Q3,0,0)
%-------------------------------------------------------------------
%       Position vectors
%-------------------------------------------------------------------
P_E_Ao> = -L1*A3>  % Position vector from E to c.o.m. body A
P_E_F>  = -LA*A3>  % Position vector from E to end of body A
P_F_Bo> = -L2*B3>  % Position vector from F to c.o.m. body B
P_F_H>  = -LB*B3>  % Position vector from F to end of body B
P_H_Co> = -L3*C3>  % Position vector from H to c.o.m. body C
P_H_I>  = -LC*C3>  % Position vector from H to end of body C
P_E_I> = P_E_F> + P_F_H> + P_H_I>
express(P_E_I>,N) % Express position vector in N reference frame
%-------------------------------------------------------------------
%       Generalized Speeds
%-------------------------------------------------------------------
Q1' = U1
Q2' = U2
Q3' = U3
Q1'' = DT(Q1')
Q2'' = DT(Q2') %
Q3'' = DT(Q3')
%-------------------------------------------------------------------
%       Angular velocities
%-------------------------------------------------------------------
angvel(N,A)
```

```
angvel(N,B)
angvel(N,C)
%----------------------------------------------------------------
%       Angular accelerations
%----------------------------------------------------------------
ALF_A_N> = DT(W_A_N>,N)
ALF_B_N> = DT(W_B_N>,N) %
ALF_C_N> = DT(W_C_N>,N)
%----------------------------------------------------------------
%       Velocities
%----------------------------------------------------------------
V_E_N> = 0> % Velocity of point E in reference frame N
V2PTS(N,A,E,Ao)
V2PTS(N,A,E,F)
V2PTS(N,B,F,Bo)
V2PTS(N,B,F,H)
V2PTS(N,C,H,Co)
V2PTS(N,C,H,I)
%----------------------------------------------------------------
%       Accelerations
%----------------------------------------------------------------
A_E_N> = 0> % Acceleration of point E in reference frame N
A2PTS(N,A,E,Ao)
A2PTS(N,A,E,F)
A2PTS(N,B,F,Bo)
A2PTS(N,B,F,H)
A2PTS(N,C,H,Co)
A2PTS(N,C,H,I)
%----------------------------------------------------------------
%       Forces and Torques
%----------------------------------------------------------------
GRAVITY( -G*N3> )
Force_I> = GRFx*N1> + GRFy*N3>
TORQUE(B/C,T3*B2>)
TORQUE(A/B,T2*A2>)
TORQUE(N/A,T1*N2>)
%----------------------------------------------------------------
%       Kanes Equations of Motion
%----------------------------------------------------------------
Zero = expand(FR() + FRSTAR())
```

```
zero = arrange(zero,2,u1,u2,u3)
zero = arrange(zero,1,U1',u2',u3')
KANE()
%----------------------------------------------------------------
%       Output constants for Matlab code
%----------------------------------------------------------------
UNITS GRFx = N, GRFy = N UNITS T = s, Q1 = rads, Q2 = rads,
Q3 = rads CHECK = NICHECK()%
output T,Q1,Q2,Q3,U1,U2,U3,T1,T2,T3,check %
pause
save 2DID3L.all
```

B.2 Three-Dimensional Hindlimb Model Code

```
%*****************************************************************
%     File:    3D_ID ( Setup for Autloev 3.4)
%     Problem: Analysis of 3 link leg with 4 torques and 3 GRF's
%     Calculates Kanes Eqn's
%     Measures angles relative to the negative Z-axis
%*****************************************************************
%----------------------------------------------------------------
%       Newtonian, bodies, frames, particles, points
%----------------------------------------------------------------
degrees      off   % angles expressed in radians
Newtonian    N     % Newtonian reference frame
Bodies       A,B,C % Three segments of the Hindlimb
Points       D,E,F,O
%----------------------------------------------------------------
%       Variables, constants, specified, mass, inertia
%----------------------------------------------------------------
VARIABLES    Q{4}''    % Angles + deriv's
VARIABLES    U{7}'     % Generalized Speeds and their derivatives
VARIABLES    FGRF1,FGRF2,FGRF3,F1,F2,F3 % Forces
VARIABLES    T1,T2,T3,T4  % Torques
%
Constants    L1,L2,L3  % Distance centers of mass for links A,B,C
Constants    LA,LB,LC  % Lengths of Bodies A,B, and C
```

```
Constants    G          % gravity
%
MASS         A = MA, B = MB, C = MC % Masses of bodies A,B,C
%  Model the limbs as slender rods
Inertia      A, IGA, IGA, IGA % inertia properties for body A
Inertia      B, IGB, IGB, IGB % inertia properties for body B
Inertia      C, IGC, IGC, IGC % inertia properties for body C
%-------------------------------------------------------------
%       Geometry relating unit vectors
%-------------------------------------------------------------
dircos(N,A,SPACE213,-Q1,Q4,0)
dircos(N,B,space213,-Q2,Q4,0)
dircos(N,C,space213,-Q3,Q4,0)
%-------------------------------------------------------------
%       Position vectors
%-------------------------------------------------------------
P_O_Ao> = -L1*A3>  % Position vector from origin to c.o.m. body A
P_O_D>  = -LA*A3>  % Position vector from origin to end of body A
P_D_Bo> = -L2*B3>  % Position vector from D to c.o.m. body B
P_D_E>  = -LB*B3>  % Position vector from D to end of body B
P_E_Co> = -L3*C3>  % Position vector from D to c.o.m. body B
P_E_F>  = -LC*C3>  % Position vector from D to end of body B
P_O_F> = P_O_D> + P_D_E> + P_E_F> express(P_O_F>,n)
%-------------------------------------------------------------
%       Generalized Speeds
%-------------------------------------------------------------
Q1' = U1
Q2' = U2
Q3' = U3
Q4' = U4
Q1'' = DT(Q1')
Q2'' = DT(Q2')
Q3'' = DT(Q3')
Q4'' = DT(Q4')
%-------------------------------------------------------------
%       Angular velocities
%-------------------------------------------------------------
angvel(N,A)
angvel(N,B)
angvel(N,C)
```

```
%-----------------------------------------------------------------
%       Angular accelerations
%-----------------------------------------------------------------
ALF_A_N> = DT(W_A_N>,N)
ALF_B_N> = DT(W_B_N>,N)%
ALF_C_N> = DT(W_C_N>,N)
%-----------------------------------------------------------------
%       Velocities
%-----------------------------------------------------------------
V_O_N> = U5*N1> +U6*N2> + U7*N3
V2PTS(N,A,O,Ao)
V2PTS(N,A,O,D)
V2PTS(N,B,D,Bo)
V2PTS(N,B,D,E)
V2PTS(N,C,E,Co)
V2PTS(N,C,E,F)
%-----------------------------------------------------------------
%       Accelerations
%-----------------------------------------------------------------
A_O_N> = DT(V_O_N>, N)
A2PTS(N,A,O,Ao)
A2PTS(N,A,O,D)
A2PTS(N,B,D,Bo)
A2PTS(N,B,D,E)
A2PTS(N,C,E,Co)
A2PTS(N,C,E,F)


%-----------------------------------------------------------------
%       Motion Constraints
%-----------------------------------------------------------------
AUXILIARY[1] = Dot(V_O_N>, N1>)      % where Dot(V_O_N>,N1>) = 0
AUXILIARY[2] = Dot(V_O_N>, N2>)      % where Dot(V_O_N>,N2>) = 0
AUXILIARY[3] = Dot(V_O_N>, N3>)      % where Dot(V_O_N>,N3>) = 0
Constrain( AUXILIARY[U5,U6,u7] )     % Solves for U5,U6,U7
%-----------------------------------------------------------------
%       Forces and Torques
%-----------------------------------------------------------------
GRAVITY( -G*N3> ) % Gravity acts in negative Z dir.
Force_F> = FGRF1*N1> + FGRF2*N2> + FGRF3*N3>
```

```
Force_O> = F1*N1> + F2*N2> +F3*N3> % Forces acting on hip
TORQUE(B/C,T3*B2>) % torques on each joint
TORQUE(A/B,T2*A2>)
TORQUE(N/A,T1*N2> + T4*N1>)
%----------------------------------------------------------------
%       Kanes Equations of Motion
%----------------------------------------------------------------
Zero = expand(FR() + FRSTAR())
zero = arrange(zero,2,u1,u2,u3,u4)
zero = arrange(zero,1,U1',u2',u3',u4')
KANE(F1,F2,F3)
%----------------------------------------------------------------
%       Output constants for Matlab code
%----------------------------------------------------------------
UNITS FGRF1 = N, FGRF2 = N, FGRF3 = N, F1 = N, F2 = N, F3 = N
UNITS T = s, Q1 = rads, Q2 = rads, Q3 = rads, Q4 = rads CHECK =
NICHECK() output T,Q1,Q2,Q3,Q4,U1,U2,U3,U4,F1,F2,F3,check pause
save 3did.all
```